Study of deep-level defects in Cu(In, Ga)Se_2 thin film grown by three-stage process

Xiaobo Hu

Doctoral Program in Applied Physics

Submitted to the Graduate School of
Pure and Applied Sciences
in Partial Fulfillment of the Requirements
for the Degree of Doctor of Philosophy in
Engineering

at the
University of Tsukuba

Abstract

Photovoltaics (PV) technology is a promising method to convert solar energy into electric power which usually utilizes a kind of semiconductor device called solar cell. Among the many kinds of solar cells, thin-film solar cells have attracted more and more attention due to their high efficiencies and low material cost. Amongst, thin film solar cell based on polycrystalline $Cu(In_{1-x},Ga_x)Se_2$ (CIGS) material is the most efficient and the highest solar cell efficiency of 21.7% makes it the world record among all thin film technology. The highest efficiency reported was based on CIGS material with a bandgap energy around 1.15 eV (Ga content x=0.3). However, next-generation high-performance solar cells will require high-quality CIGS films with even larger Ga content since the ideal band gap energy for the highest efficiency is predicted to be 1.4 eV (x=0.7). Nevertheless, conversion efficiency of CIGS solar cell decreases with increasing Ga contents (x>0.3). Thus, the development of CIGS solar cells with wide bandgap (x>0.3) is indispensable. The investigation of the mechanisms that may decrease the efficiency of wide-bandgap CIGS solar cells is very important.

This thesis focused on the study of deep-level defects which located near the midgap energy level of the bandgap in Cu(In, Ga)Se_2 thin film solar cells since these defects may act as active recombination centers to limit the cell efficiency.

A defect level at 0.8 eV above the valence band maximum (VBM) was detected by transient photo-capacitance (TPC) spectroscopy, the position of which was almost unchanged with Ga/III ratio. Also, a relatively quantitative comparison of deep defect densities based on the results of TPC showed that the defect density seemed to increase with increasing Ga/III ratio. Then, this defect was proved to act as a trap center at low temperature (140 K) but act as a recombination center at at room temperature by a two-wavelength excitation photocapacitance method.

Quantitative information of the the 0.8 eV deep-level defect was then investigated by a Steady-state photocapacitance (SSPC) method with low intensity excitation light. The defect concentration in the order of 10^{13}-10^{14} cm^{-3} and the photoionization cross section in the order of 10^{-17}-10^{-16} cm^2 were obtained and both of them were found to increase with Ga content (x) in the range of 0.30-0.80. The increase of the defect concentration with Ga content may be an important factor to limit the efficiency of wide-bandgap CIGS solar cells.

The electronic structure of the 0.8 eV deep-level defect was investigated by the SSPC measurements with high intensity excitation light. A possible configuration coordinate model was proposed for the 0.8 eV defect to explain the results assuming two states: a stable state D and its metastable state D* with a large lattice relaxation. The metastable state may provide another carrier recombination path to limit the cell efficiency.

The effect of the deep-level defects on the devices was investigated by Time-resolved photoluminescence (TRPL). The results showed that deep-level defects other than shallow-level defects acted as the main recombination centers to cause the short minority carrier lifetime in Cu(In, Ga)Se_2 thin films. By comparing the results of TRPL and photocapacitance (including TPC and SSPC), it was deduced that the 0.80 eV deep-level defect may act as a significant recombination center that decreases the minority carrier lifetime in CIGS thin films when Ga content increases.

Possible origins of the 0.8 eV defect were considered to be related to the formation of $Cu_{2-x}Se$ secondary phase while comparing the respective quantity relationship with Ga/III ratio.

Since the 0.80 eV deep-level defect is one of the causes for the degradation of CIGS cell efficiency with high Ga content, it is necessary to decrease the density of defects to improve cell efficiency, especially for CIGS samples with high Ga content.

Tables of contents

Chapter 1 Introduction

1.1 Energy crisis and solar energy

Energy is the driving force for development, economic growth, automation, and modernization of the human world. The global energy demand is in apex due to fast growth of industrialization and population. The world primary energy consumption is shown in Fig. 1-1 [1-1]. In the past 15 years, conventional fossil fuels including coal, natural and oil have been always acting as the main sources of the energy supply, which accounted for over 80%. As the demand of energy is still increasing very fast year by year, however, the conventional fossil fuels like coal, oil, natural gas, etc., are fast depleting. Even ruling out of this point, the environment issues such as pollutions and the emission of CO_2 caused by fossil fuels can not be ignored. Thus, development of alternative energy sources particularly those are renewable and friendly to environment are inevitable to solve the energy crisis.

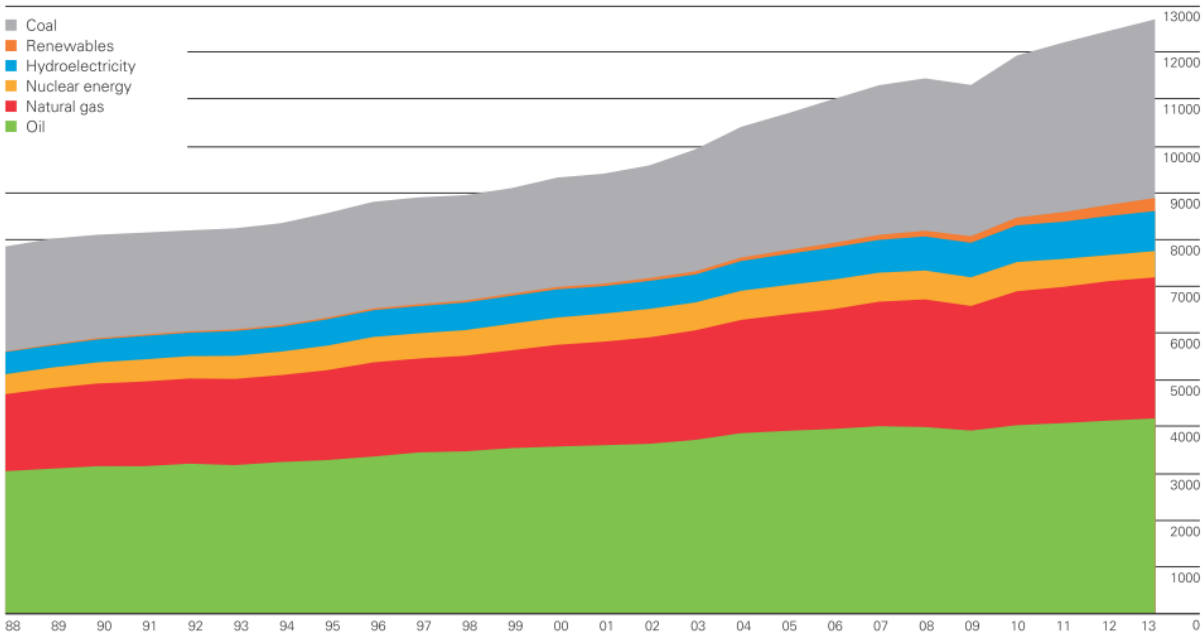

Fig. 1-1 World primary energy consumption from 1988 to 2013 by fuel (Mtoe), where Mtoe stands for million tonnes oil equivalent [1-1].

Solar energy is an attractive alternative source to the fossil fuels since it is inexhaustible and pollution free. The Earth receives an annual energy from the Sun which is about 20,000 times more than the present annual energy consumption of the world. Even if a fraction of this energy is effectively utilized, the energy problems can be mitigated to some extent. Methods of solar energy utilization can be broadly divided into two categories: (i) photothermal and (ii) photovoltaic. The photothermal systems convert solar radiation into thermal energy, which may be used directly or converted into electricity. The photovoltaic systems directly convert sunlight into electricity. Fig. 1-2 shows the predictions of the future energy supply trends in which the solar energy sources and especially the photovoltaic energy will gradually become a primary energy source [1-2].

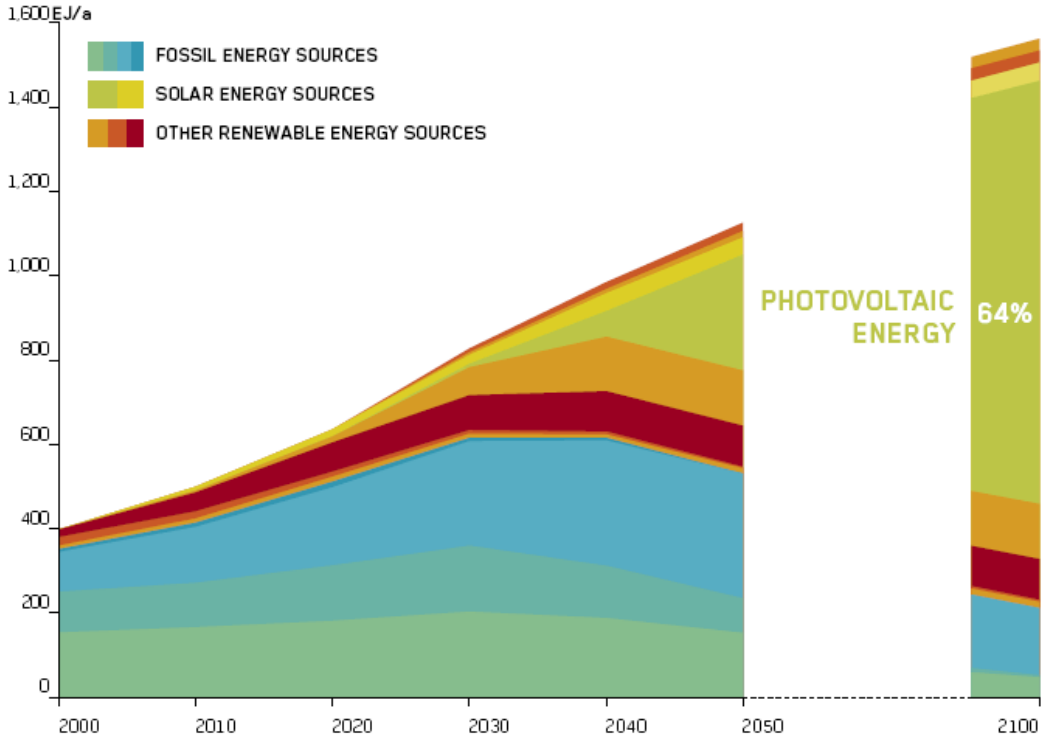

Fig. 1-2 Projected share of energy source until 2050/2100 [1-2].

Fig. 1-3 shows the cumulative growth in PV capacity from 1992 to 2011 within the grid-connected and off-grid applications for PV, this figure shows a significant and increasing proportion of worldwide PV capacity [1-3].

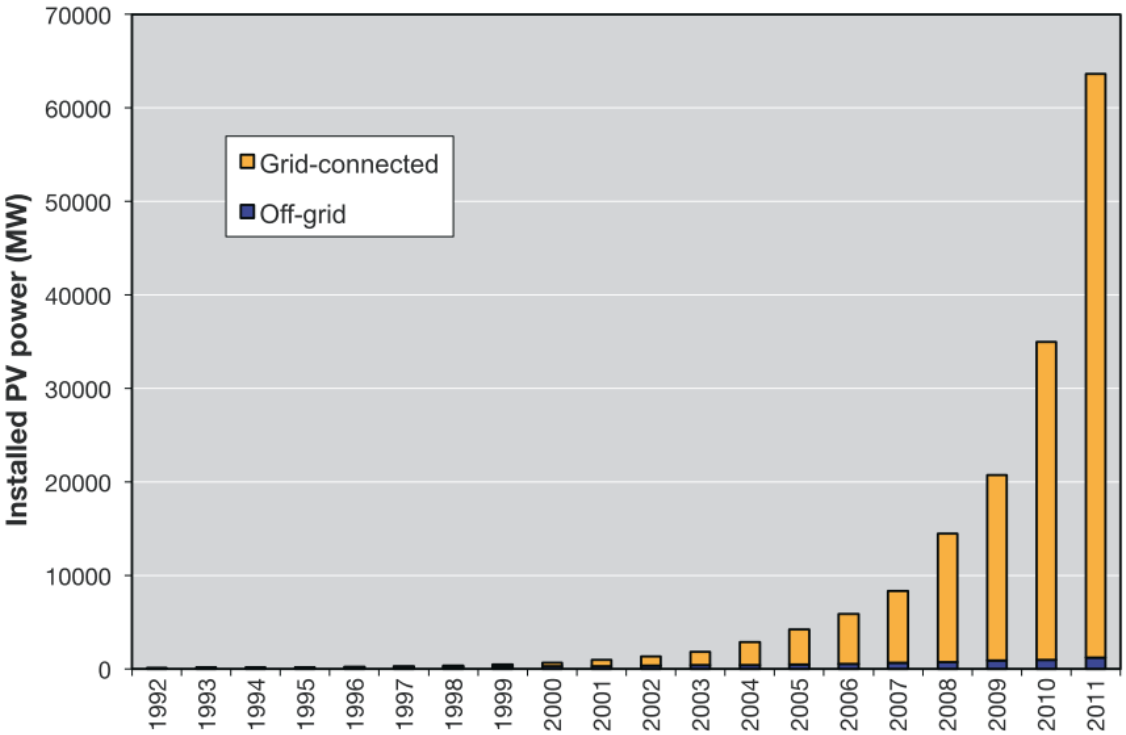

Fig. 1-3.The cumulative growth in PV capacity from 1992 to 2011 within the two primary applications (grid-connected and off-grid use) for PV [1-3].

1.2 Photovoltaic Technologies

Commercial PV modules may be divided into two broad categories: wafer based crystalline Si (c-Si) and thin film (TF) based solar cells, with c-Si and TF representing 85–90% and 10–15% of today's global annual market, respectively [1-4]. Additionally, there are a range of currently emerging technologies, including advanced TF concepts, concentrating PV, and organic and dye-sensitized solar cell. In the long-term, novel innovative concepts are envisaged. These are hoped to achieve significant performance increase and cost reduction by implementing nano-geometries, plasmonic effects, up- or down-conversion, etc. Fig. 1-4 compares these technologies by status and prospect in terms of solar to electricity conversion efficiency [1-5]. To provide a guideline of the chronological and topical evolution of R&D of PV, current and emerging concepts have been grouped by Green into "first", "second", and "third generation" technologies [1-6].

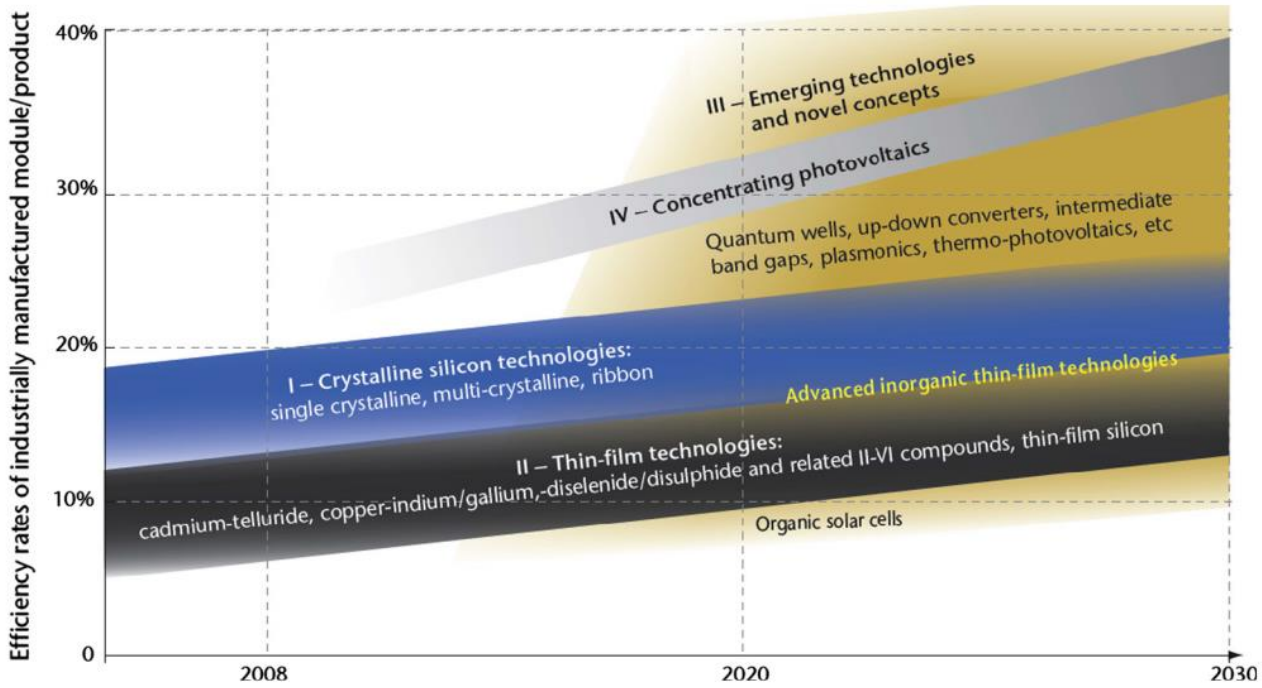

Fig. 1-5. Photovoltaic technology status and prospects in terms of efficiency range of commercial modules or products from 2007 to 2030. [1-7].

First generation PV

The first generation PV is usually pointed to the single-junction solar cells based on single-crystalline (sc-) and multi-crystalline (mc-) Si wafers that are typically serially interconnected to form PV modules. Si-based solar cell fabrication is based on mature and reliable high-throughput technologies, since it benefited greatly from its symbiosis with the IC industry providing materials and processing know-how. Continuous technology improvements pushed commercial top-performer modules based on sc-Si well above the 20% efficiency [1-5]. On the other hand, mc-Si based commercial modules achieve lower record efficiencies of up to 18%, but at lower costs. In the future, seed-assisted cast quasi-single crystalline (QSC) Si shows great potential to drive mc-Si out of the market, since QSC Si exhibits improved material properties---that is higher minority carrier lifetime and fewer grain boundaries and dislocations at high productivity [1-8]. Nowadays, the high efficiencies and low prices achieved make it more and more difficult for upcoming technologies to compete with Si mainstream.

Second generation PV

The second generation is usually represented by the thin-film (TF) technologies which are expected to exhibit lower production costs per surface area than c-Si PV, and benefit from the economy of scale obtained with large-area industrial tools developed by flat panel display technologies [1-9]. By an integrated process flow, thin film absorber materials of 1 μm to 3 μm thickness are deposited on low-cost substrates such as glass, directly leading to PV modules [1-10]. This cost-reduction potential compared to c-Si based technologies is utilized as long as efficiency and fabrication costs per unit area remain comparable. Between 2002 and 2008 annual TF production rose from 17 MW to nearly 1 GW, raising its market share to almost 15% [1-11]. During that time the poly-Si bottleneck led to massive venture capital investments into all kinds of TF technologies, mainly a-Si based ones. Today, one main issue for commercial TF solar cells/modules is to close the gap to the efficiencies of their laboratory counterparts. These range from 20% for CIGS over 17% for CdTe to 12% for a-Si/lc-Si, whereas medium standard module efficiencies range from 16% for CIGS over percent for CdTe to 10% for a-Si based tandems [1-5]. These differences are mainly due to unresolved issues relating to poor material reproducibility and deposition uniformity over large areas [1-12]. Nevertheless, in recent years some companies made important steps toward higher efficiency such as ZSW in the case of CIGS [1-13]. In order to compete with c-Si in terms of cost per watt addition, completely new concepts and fabrication techniques may be developed and added to second generation technologies. Thus such concepts are commonly summarized as third generation technologies.

Third generation PV

The third generation PV is envisaged to exhibit higher efficiency and/or apply lower cost substrates or deposition methods to exceed the limits of single-junction devices. This may lead to ultra-high efficiency devices exhibiting similar production cost as compared to first or second generation PV (Fig. 1-5) [1-6]. Third generation PV includes new conceptual approaches such as (i) multiple energy level absorption based on different inorganic (such as a-Si, III-V semiconductors, thin-film or nanostructures) and organic materials, (ii) intermediate-level cells as suggested for III-V, II-VI, and chalcopyrite systems, (iii) multiple carrier excitation in quantum dots, (iv) modulation of the spectrum by up/down conversion, (v) thermo-photovoltaics or thermophotonics, and (vi) hot carrier cells that collect photo-generated carriers before they have a chance to thermalize. But also PV relying on optical concentration, the deposition of established material systems on novel substrates, or the use of alternative fabrication techniques are frequently accounted to third or next generation PV.

1.3 Solar cell basics

A Solar cell is basically a semiconductor diode. The semiconductor material absorbs the incoming photons and converts them into electron-hole pairs. In the photo-generation process, the decisive parameter is the ban-dgap energy E_g of the semiconductor. In an ideal case, photons with an energy $h\nu<E_g$ will not contribute to photogeneration, whereas photons with an energy $h\nu \leq E_g$ will each contribute the energy E_g to the photo-generated electron-hole pair, with the excess energy ($h\nu$-E_g) being very rapidly lost by thermalization.

1.3.1 Operating principles

Fig. 1-6 shows the electron-hole pairs generated by the absorbed photons in different regions of the solar cell. The electron-hole pairs generated in the depletion region will be separated the built-in electric field (E) or the drift electric field. The generated electrons will drift to the neutral n-side and make the region negative; the holes will reach to the neutral p-side and makes this side positive. So a photo induced voltage develops between the terminals with p-side positive relative to n-side. If external load is connected to the terminals,

the excess electron in the n-side will flow through the load to the p-side and recombine there with hole and current occurs. The electron-hole pairs generated in the neutral regions are collected by diffusion processes. Photo-generated electrons in the neutral p-region and photo-generated holes in the neutral p-region are possibly collected to the depletion region where the possibilities are determined by the distances between the position where the electrons and holes generated and the edge of the depletion region. If the distance is smaller than the diffusion length of the electrons (L_e) in the p-region or holes (L_h) in the n-region, then the electrons and holes can diffuse to depletion region and drift by electric field and contribute to photovoltaic effect. The diffusion length is described by

$$L_{e,h} = \sqrt{2D_{e,h}\tau_{e,h}} \tag{1-1}$$

where D is the diffusion coefficient of electron in p-region or hole in n-region, τ is the lifetime of electron in p-region or hole in n-region.

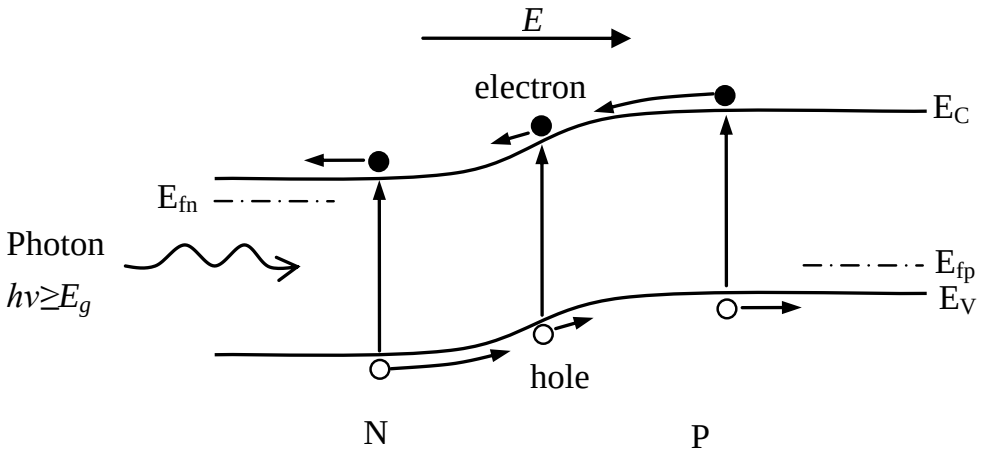

(a)

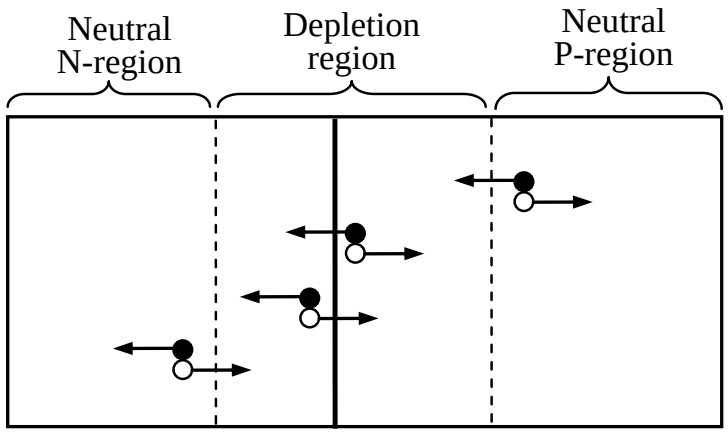

(b)

Fig. 1-6. (a) The energy band diagram of an pn junction solar cell under illumination, *E*: built-in electric field; E_{fn}, E_{fp}: qusi-fermi energy level in the n-side and p-side; E_C, E_V: conduction band minimum and valence band maximum; (b) the corresponding diagram of the pn junction which shows the photo-generated electron-hole pairs in different regions.

1.3.2 IV characteristics

Fig. 1-7 (a) shows equivalent circuit diagram of a solar cell where R_s denotes the series resistance and R_{sh} is the shunt resistance. Fig. 1-7 (b) shows the I–V characteristics under dark and illumination conditions. It is noted that the shaded area in the fourth quadrant of the photo I-V curve represents the power generated in the solar cell. The dark and photo I-V characteristics of a p-n junction solar cell are discussed next.

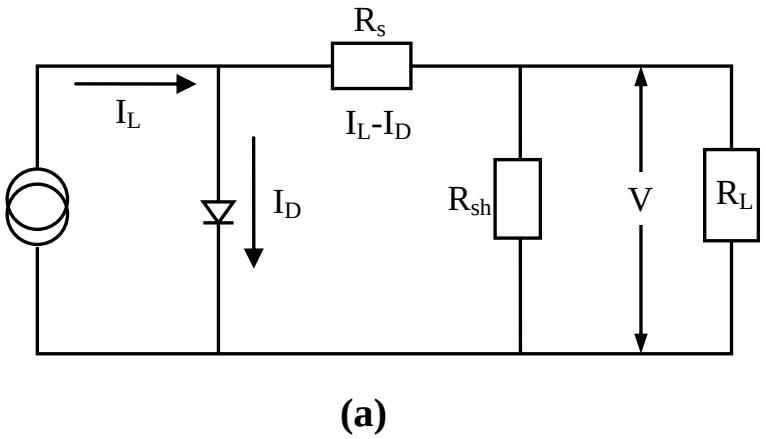

(a)

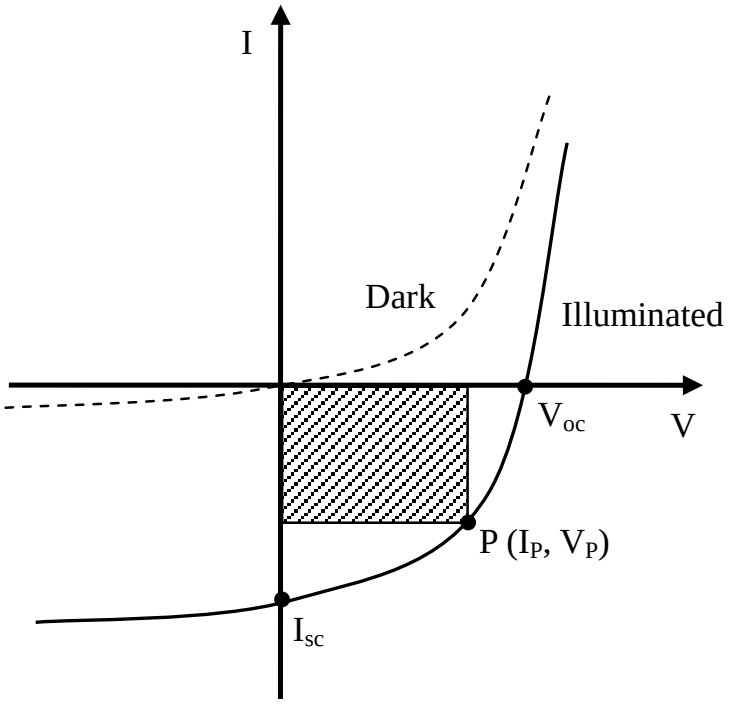

(b)

Fig. 1-7. (a) Equivalent circuit diagram of a solar cell; (b) I–V characteristics under dark and illumination conditions

(i) Dark I–V characteristics.

The dark current of a p-n junction solar cell under forward-bias conditions usually consists of two components: (1) the injection current due to injection of majority carriers across the p-n junction, (2) the recombination current due to the recombination of electrons and holes via deep-level traps in the junction space-charge region (SCR) or depletion region. In a high-quality p-n junction solar cell such as single crystal

silicon, the injection current is usually the dominant component. However, the recombination current can become a dominant component for solar cells fabricated from low-quality materials such as amorphous and polycrystalline thin film materials.

The injection current, which is due to the injection of holes from the p region into the n region and electrons from the n region into the p region of the junction, can be described by the ideal Shockley diode equation, which is given by [1-14],

$$I_d = I_s[\exp(\frac{qV}{kT}) - 1] \tag{1-2}$$

where

$$I_s = qn_i^2 A_j (\frac{D_h}{L_h N_D} + \frac{D_e}{L_e N_A}) \tag{1-3}$$

is the reverse saturation current due to the injection of electrons and holes across the p-n junction, A_j is the junction area, n_i is the intrinsic carrier density, D_e and D_h denote the electron and hole diffusion coefficients, L_e and L_h are the electron and hole diffusion lengths, respectively.

The recombination current in a p-n junction solar cell is due to the recombination of electrons and holes via deep-level defect centers inside the junction space-charge region. Based on the Shockley–Read–Hall (SRH) model, this recombination current component can be expressed by

$$I_r = \left(\frac{qn_i WA_j}{2\sqrt{\tau_{n0}\tau_{p0}}} \right) [\exp(\frac{qV}{mkT}) - 1] \tag{1-4}$$

where W is the width of the depletion region, τ_{n0} and τ_{p0} are the minority electron and hole lifetimes in the p and n regions, respectively. m is the diode ideality factor, the ideality factor may vary between 1 and 2, depending on the location of the defect level in the forbidden gap. For example, m equals 2 if the recombination of electron-hole pairs is via a mid-gap recombination center, and is smaller than 2 if the recombination center is not located at the mid-gap of if multilevel recombination centers exist in the junction space-charge region [1-15].

Therefore, the total dark current of a solar cell can be represented by the sum of injection and recombination current components given by Eq. (1-2) and Eq. (1-4), namely,

$$I_D = I_d + I_r \tag{1-4}$$

(ii) Photo I–V characteristics.

The photocurrent generated in a p-n junction solar cell under 1-sun conditions is discussed next. When photons with energy $hv \geq E_g$ impinge on a p-n junction solar cell, the rate of generation of electron–hole pairs as a function of distance x from the surface of the solar cell is given by

$$g_E(x) = \alpha \Phi_0 (1 - R) e^{-\alpha x} \tag{1-5}$$

where α is the optical absorption coefficient, Φ_0 is the incident photon flux density (photons/cm^{-2}s^{-1}), and R is the reflection coefficient at the semiconductor surface.

The total photocurrent density generated in a p-n junction solar cell by the incident sunlight for a given wavelength λ is

$$J_L(\lambda) = J_p(\lambda) + J_n(\lambda) + J_d(\lambda) \tag{1-6}$$

where $J_p(\lambda)$ is the photo-generated hole current density with wavelength λ in the n region of the n-p junction solar cell and $J_n(\lambda)$ is the photo-generated electron current density with wavelength λ in the p region of the n-p junction cell. $J_d(\lambda)$ is the drift component of the photocurrent density generated in the depletion region and can be expressed by,

$$J_d(\lambda) = q\int_W g_E(\lambda)dx = \alpha\Phi_0(1-R)e^{-\alpha x_j}(1-e^{-\alpha W}) \tag{1-7}$$

x_j is the junction depth.

Then, the quantum efficiency, which is defined as the number of electron-hole pairs generated per absorbed photon, for a p-n junction solar cell can be expressed by

$$\eta_Q = \frac{J_L(\lambda)}{q\Phi_0(1-R)} \tag{1-8}$$

The total photocurrent density generated in a solar cell under 1-sun conditions can be obtained by integrating Eq. (1-6) over the entire solar spectrum, which can be written as,

$$J_{ph} = \int_{\lambda_1}^{\lambda_2} J_L(\lambda)d\lambda \tag{1-9}$$

where λ_1 and λ_2 denote the cutoff wavelengths at the short- and long-wavelength limits of the solar spectrum, respectively.

(iii) Solar cell parameters.

The equivalent circuit for a p-n junction solar cell is shown in Fig. 1-7 (a), which is composed of the photocurrent component represented by a constant current source $I_{ph}=I_{sc}$, a dark current component I_D, a shunt resistance R_{sh}, and a series resistance R_s. If one neglects the effects of shunt resistance (assuming $R_{sh} \rightarrow \infty$), series resistance ($R_s \approx 0$), and the recombination current ($I_r=0$) in the depletion region, then the photo I-V characteristics of a p-n junction solar cell under illumination condition can be expressed by

$$I = -I_{ph} + I_s[\exp(\frac{qV}{kT}) - 1] \tag{1-10}$$

where I_{ph} is given by Eq. (1-9) and is the I_L in Fig. (1-7) (a), and I_s is given by Eq. (1-3). The short-circuit current can be obtained by setting V=0 in Eq. (1-10), which yields,

$$I_{sc} = -I_{ph} \tag{1-11}$$

which shows that the short-circuit current Isc is equal to the photo-generated current $-I_{ph}$. The open-circuit voltage V_{oc} can be obtained by setting I=0 in Eq. (1-10), and one obtains

$$V_{oc} = \frac{kT}{q}\ln(\frac{I_{sc}}{I_s}+1) \tag{1-12}$$

It can be seen from Eq. (1-12) that V_{oc} depends on the ratio of the short-circuit current and the dark current, and V_{oc} can be increased by keeping the ratio of I_{sc}/I_s as large as possible. This can be achieved by reducing the dark current, either by increasing the substrate doping density or by increasing the minority carrier lifetimes in the solar cell.

The output power of a solar cell can be given by,

$$P = IV = -I_{ph}V + I_s V[\exp(\frac{qV}{kT})-1] \tag{1-13}$$

Then the conditions for the maximum output power can be calculated by setting $dP/dV = 0$, where

$$I_m = \frac{qV_m I_s}{kT}\exp(\frac{qV_m}{kT}) \approx I_{ph}(1-\frac{kT}{qV_m}) \tag{1-14}$$

is the current corresponding to the maximum power output, and

$$V_m = \frac{kT}{q}\ln[\frac{I_{ph}/I_s+1}{1+qV_m/kT}] \approx Voc - \frac{kT}{q}\ln(1+\frac{qV_m}{kT}) \tag{1-15}$$

is the the voltage corresponding to the maximum power output, and the maximum power output is

$$P_m = I_m V_m = FF\cdot I_{sc}V_{oc} \approx I_{ph}[V_{oc} - \frac{kT}{q}\ln(1+\frac{qV_m}{kT}) - \frac{kT}{q}] \tag{1-16}$$

where FF is an important parameter known as the fill factor which measures the squareness of the photo I-V curve shown in Fig. (1-7) (b) and defined as

$$FF = \frac{I_m V_m}{I_{sc}V_{oc}} \tag{1-17}$$

Finally, the conversion efficiency of a p-n junction solar cell can be calculated by

$$\eta = \frac{P_m}{P_{in}} = \frac{I_m V_m}{P_{in}} = \frac{V_m^2 I_s (q/kT)\exp(qV_m/kT)}{P_{in}} \tag{1-18}$$

where P_{in} is the input power from the sunlight. The input power from the sunlight under 1-sun AM0, AM1, AM1.5G, and AM2 conditions are given by 135.3, 92.5, 100, and 69.1 mW/cm^2, respectively.

1.4 Solar cell efficiency chart

Table 1-1 describes the most recent achievement in solar cell technology [1-5]. All cells are measured under the global AM1.5 spectrum (1000 W/m^2) at 25 °C. Fig. 1-8 shows the efficiency trend of best research cells by technology type.

Table 1-1 Confirmed terrestrial cell and submodule efficiencies (IEC 60904-3: 2008, ASTM G-173-03 global) [1-5].

Classification	Efficiency (%)	Area (cm^2)	Voc (V)	Jsc (mA/cm^2)	Fill factor (%)	Test center
Silicon						
Si (crystalline)	25.6 ± 0.5	143.7 (da)	0.740	41.8	82.7	AIST
Si (multicrystalline)	20.4 ± 0.5	1.002 (ap)	0.664	38.0	80.9	NREL
Si (thin film transfer)	25.1 ± 0.4	242.6 (ap)	0.682	38.14	77.4	NREL
Si(thin film minimodule)	10.5 ± 0.3	94.0 (ap)	0.492	29.7	72.1	FhG-ISE
III-V Cells						
GaAs (thin film)	28.8 ± 0.9	0.9927 (ap)	1.122	29.68	86.5	NREL
GaAs (multicrystalline)	18.4 ± 0.5	4.011 (t)	0.994	23.2	79.7	NREL
InP (crystalline)	22.1 ± 0.7	4.02 (t)	0.878	29.5	85.4	NREL
Thin film chalcogenide						
CIGS (cell)	20.5± 0.6	0.9882 (ap)	0.752	35.3	77.2	NREL
CIGS (minimodule)	18.7± 0.6	15.892 (da)	0.701	35.29	75.6	FhG-ISE
CdTe (cell)	19.6± 0.6	1.0055 (ap)	0.8573	28.59	80.0	Newport
Amorphous/mc-Si						
Si (amorphous)	10.1± 0.3	1.036 (ap)	0.886	16.75	67.8	NREL
Si (microcrystalline)	11.0± 0.3	1.045 (da)	0.542	27.44	73.8	AIST
Dye sensitized						
Dye sensitized	11.9± 0.4	1.005 (da)	0.744	22.47	71.2	AIST
Dye (minimodule)	29.9± 0.4	17.11 (ap)	0.719	19.4	71.4	AIST
Dye (submodule)	8.8± 0.3	398.8 (da)	0.697	18.42	68.7	AIST
Organic						
Organic thin film	10.7± 0.3	1.013 (da)	0.872	17.75	68.9	AIST
Organic (minimodule)	9.1± 0.3	25.04 (da)	0.794	17.06	67.5	AIST
Organic (submodule)	6.8± 0.2	395.9 (da)	0.798	13.50	62.8	AIST
Multijunction devices						
InGaP/GaAs/InGaAs	37.9 ± 1.2	1.047 (ap)	3.065	14.27	86.7	AIST
a-Si/nc-Si/nc-Si(thin film)	13.4 ± 0.4	1.006 (ap)	1.863	9.52	71.9	NREL
a-Si/nc-Si (thin film cell)	12.3 ± 0.3%	0.962 (ap)	1.365	12.93	69.4	AIST
a-Si/nc-Si (thin film minimodule)	11.8 ± 0.6	40.26 (ap)	1.428	12.27	67.5	FhG-ISE

*ap, aperature area; da, designated illumination area; t, total area.

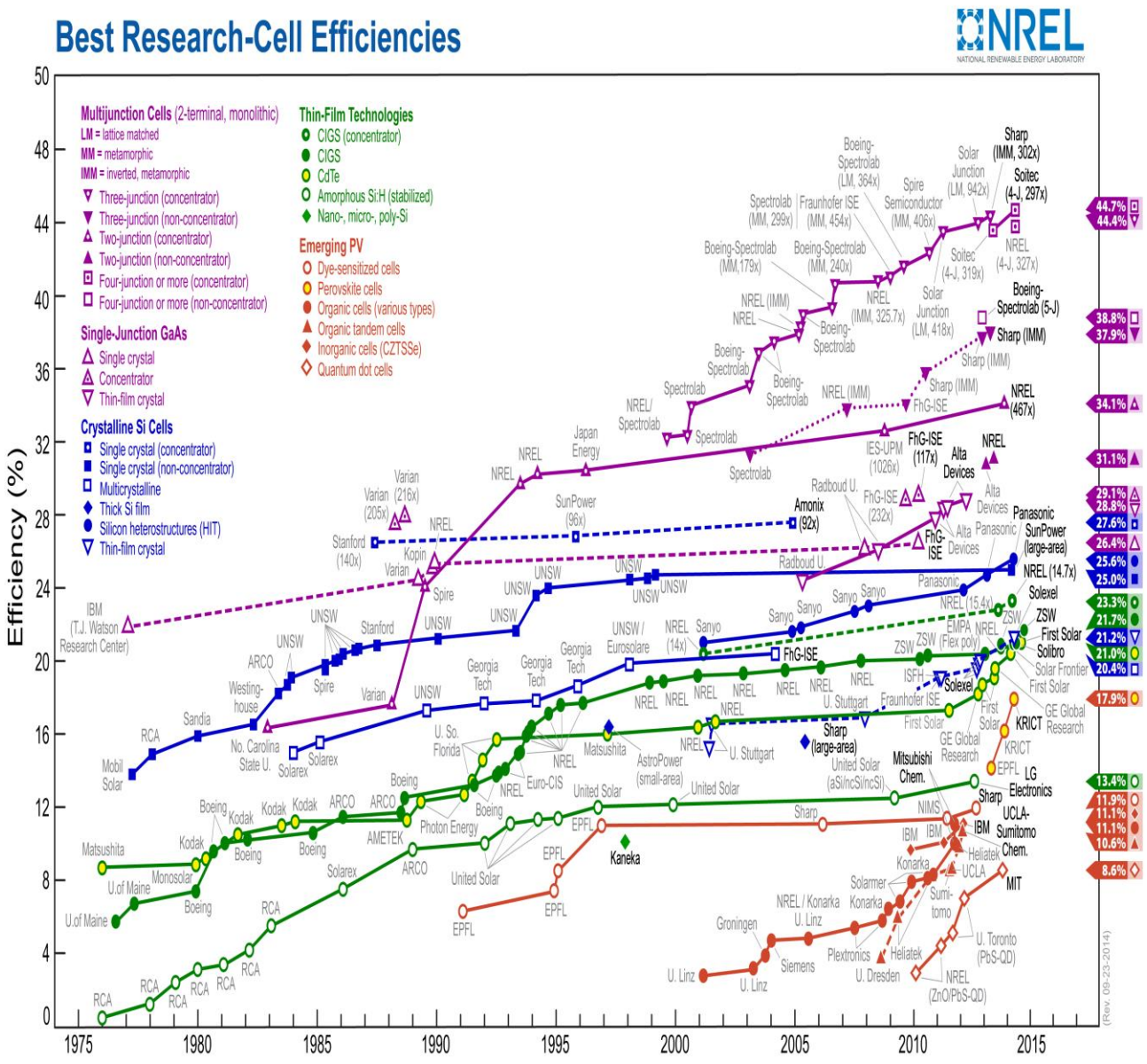

Fig. 1-8. Efficiency evolution of best research cells by technology type. This figure identifies those cells that have been measured under standard conditions and confirmed at one of the world's accepted centers for standard solar-cell measurements [1-16]

1.5 CIGS thin film solar cell

Thin-film solar cells are basically thin layers of semiconductor materials applied to a solid backing material. Thin films greatly reduce the amount of semiconductor material required for each cell when compared to silicon wafers and hence lowers the cost of production of photovoltaic cells. Among the many kinds of thin film materials (see the thin-film technologies in Fig. 1-8), copper ternary chalcogenide compounds and alloys have emerged over last 20 years as promising absorber layer. Efficiency of 21.7% [1-13] is achieved using $Cu(In_{1-x}Ga_x)Se_2$ (CIGS) absorber layer which equals world record solar conversion efficiency among all thin film technology.

1.5.1 Properties of CIGS absorber layer

1.5.1.1 Crystal Structure

Cu(In, Ga)Se_2 compounds (I-III-VI_2) crystallize in the chalcopyrite structure. The name "chalcopyrite" originally came from the mineral $CuFeS_2$ compound. This is a diamond-like structure similar to the sphalerite or zinc blende structure (Fig. 1-9 (a)) but with an ordered substitution of the group I (Cu) and group III (In or Ga) elements on the group II (Zn) sites of sphalerite. This gives a tetragonal unit cell depicted in Fig. 1-9 (b). Because of the different bond length strength and bond lengths of the group I-VI (Cu-Se) and III-VI (In-Se, Ga-Se) bonds, the lattice parameter c in general is not exactly 2a, and the deviation from c/a=2 is called the tetragonal distortion of the unit cell [1-17, 18].

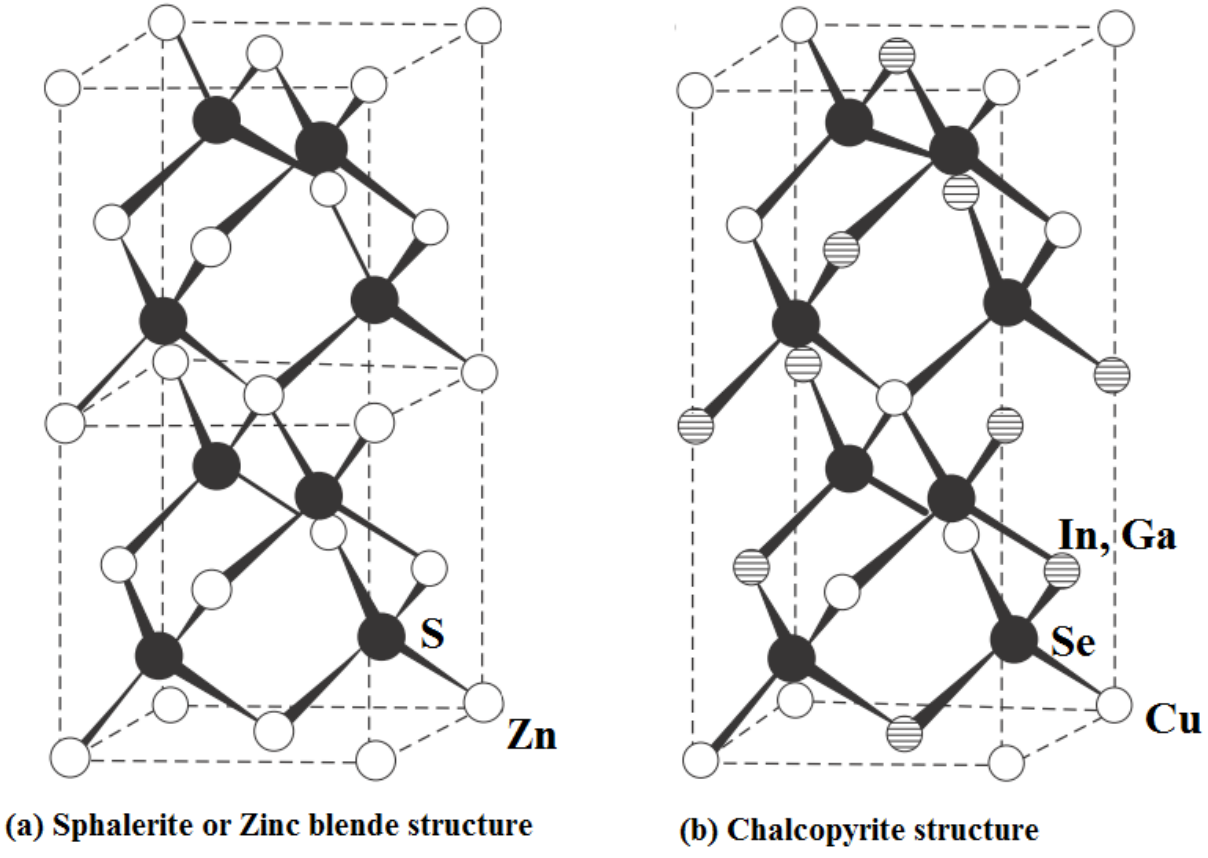

Fig. 1-9. Crystal structure of (a) sphalerite or Zinc blende (ZnS) and (b) chalcopyrite (Cu(In, Ga)Se_2).

1.5.1.2 Optical properties

CIGS absorbers have direct band gaps and large absorption coefficients $\alpha > 10^4$ cm^{-1} above the band gap. This makes this material very suitable as absorber material in thin-film solar cells, as only thickness of about 1-2 μm are needed to absorb most of the above-band gap light from the solar spectrum, without the need for light trapping. The absorption coefficients of some typical materials for solar cell dependent on the photon energy are shown in Fig. 1-10. Fig. 1-11 shows the absorption coefficients of three typical chalcopyrite materials

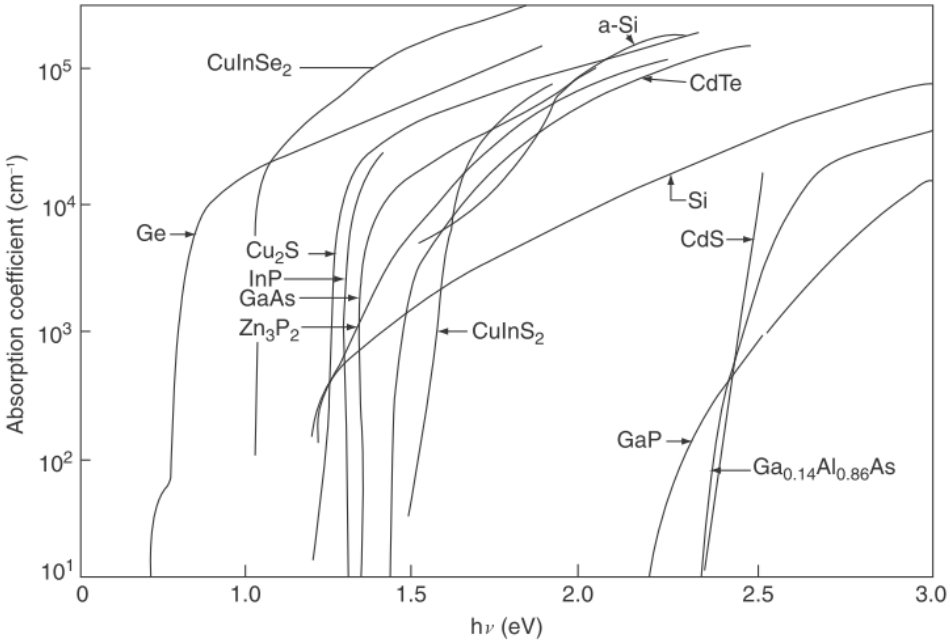

Fig. 1-10. Optical absorption coefficient spectral dependence for some typical semiconductor materials which are usually utilized as absorbers in solar cells [1-18]

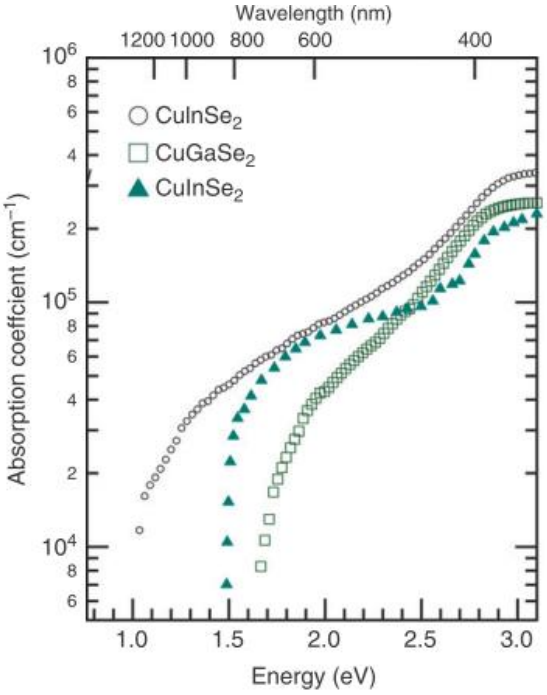

Fig. 1-11. Absorption coefficients of three typical chalcopyrite materials: $CuInSe_2$, $CuGaSe_2$, and $CuInS_2$ [1-19].

Usually in the absorption spectrum, the fundamental absorption edge is well described by

$$\alpha = A(E - E_g)^2 / E \tag{1-19}$$

for a typical direct band gap semiconductor. Where the proportionality constant *A* depends on the density of states associated with the photon absorption. From this relation, a band gap value of E_g=1.02±0.02 eV is obtained for $CuInSe_2$ (CIS).[1-20, 21]. The band gap of $CuGaSe_2$ (CGS) is obtained about 1.68 eV [1-22, 23]. For $CuIn_{1-x}Ga_xSe_2$, the bandgap can be described by the equation

$$E_g(x) = x \cdot E_g(CGS) + (1-x) \cdot E_g(CIS) - x \cdot (1-x) \cdot b \tag{1-20}$$

where the *b* is called optical bowing parameter. The value of b is calculated equaling to 0.21 by theoretical calculations as compared to values in the range of 0.11 to 0.26 determined in various experiments [1-24].
In our case, a value of "b" as 0.116 eV [1-25] is used to estimate the band gap and the resulting band gap energy of CIGS becomes

$$E_g = 1.00 + 0.564x + 0.116x^2 \tag{1-21}$$

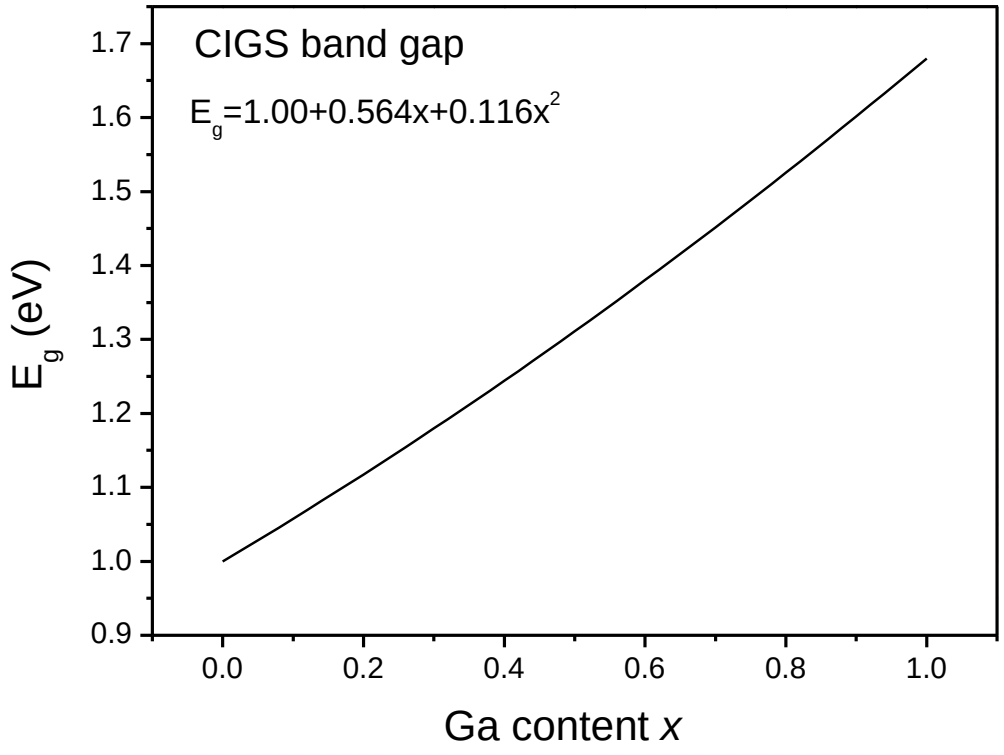

Fig. 1-12. Calculated CIGS band gap energy for different Ga composition.

1.5.1.3 Phase diagram

For CIGS, a number of different phases are possible depending on the exact compositions and the growth conditions. In Fig.1-13(a), a ternary phase diagram of $CuInSe_2$ with the corner points Cu, In and Se is shown. The thin-film materials prepared at varying Cu/(In+Ga) composition usually conform to the tie-line spanned by Cu_2Se and In_2Se_3. The desired chalcopyrite phase in this diagram is at the center of the tie-line. An equilibrium pseudobinary phase diagram composed of a mixture of In_2Se_3 and Cu_2Se, corresponding to the tie-line in Fig.1-13(a) is shown in Fig.1-13(b) [1-26]. Observed phases are indicated as a function of growth temperature: α denotes the chalcopyrite phase, β denotes ordered defect chalcopyrite phases, such as $CuIn_5Se_8$ or $CuIn_3Se_5$ and δ is the sphalerite phase occurring only at high temperatures. It can be seen that there is a small region between stoichiometry and the copper-poor side where single-phase chalcopyrite is obtained at 500 °C. This region narrows further for lower temperatures. On the Cu-rich side, Cu_xSe phases segregate and on the Cu-poor side a coexistence of chalcopyrite and defect chalcopyrite phases is expected. It is interesting to note that at low temperatures even for stoichiometric composition Cu_xSe phase segregation is expected, which has to be considered in the design of growth processes for these compounds. It has been found that the width of the chalcopyrite single-phase region is increased by alloying with gallium (Ga) and/or doping with Na [1-27].

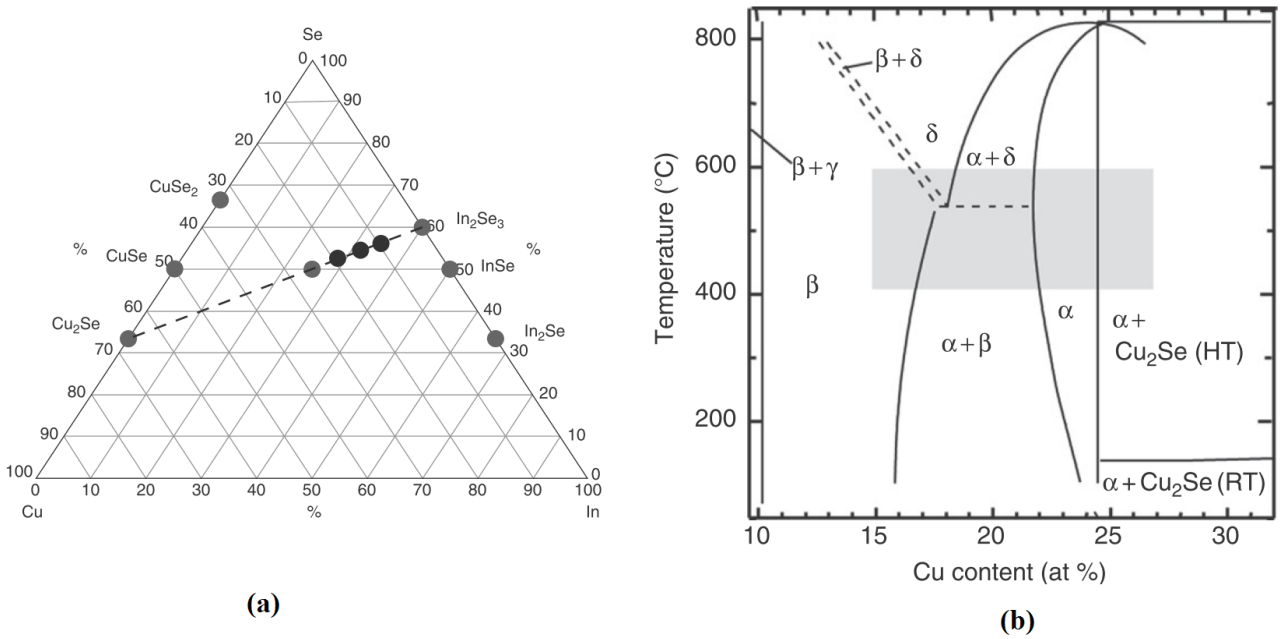

Fig. 1-13. (a) Ternary phase diagram for Cu–In–Se system. The dashed line indicates the pseudobinary tie-line between Cu_2Se and In_2Se_3. Material phases occurring during different growth processes are indicated as black circles. (b) Pseudobinary phase diagram for In_2Se_3-Cu_2Se tie-line shown in (a). The shaded area indicates the regions in the phase diagram relevant to multistage coevaporation of high-efficiency chalcopyrite solar cells [1-28].

1.5.2 CIGS solar cell

Fig. 1-14 shows a typical Cu(In,Ga)Se2 (CIGS) thin-film solar cell structure which consists of several semiconductor layers: a metallic (Mo) back contact, a p-CIGS absorber layer, an n-type (or intrinsic) CdS buffer layer; an intrinsic ZnO layer and an n^+-ZnO transparent front contact. Metallic Ni/Al contact grids are made to complete the cell. The whole structures are typically deposited on Soda-Lime glass (SLG) substrates. The typical thickness of each layer and the depositing method are also shown.

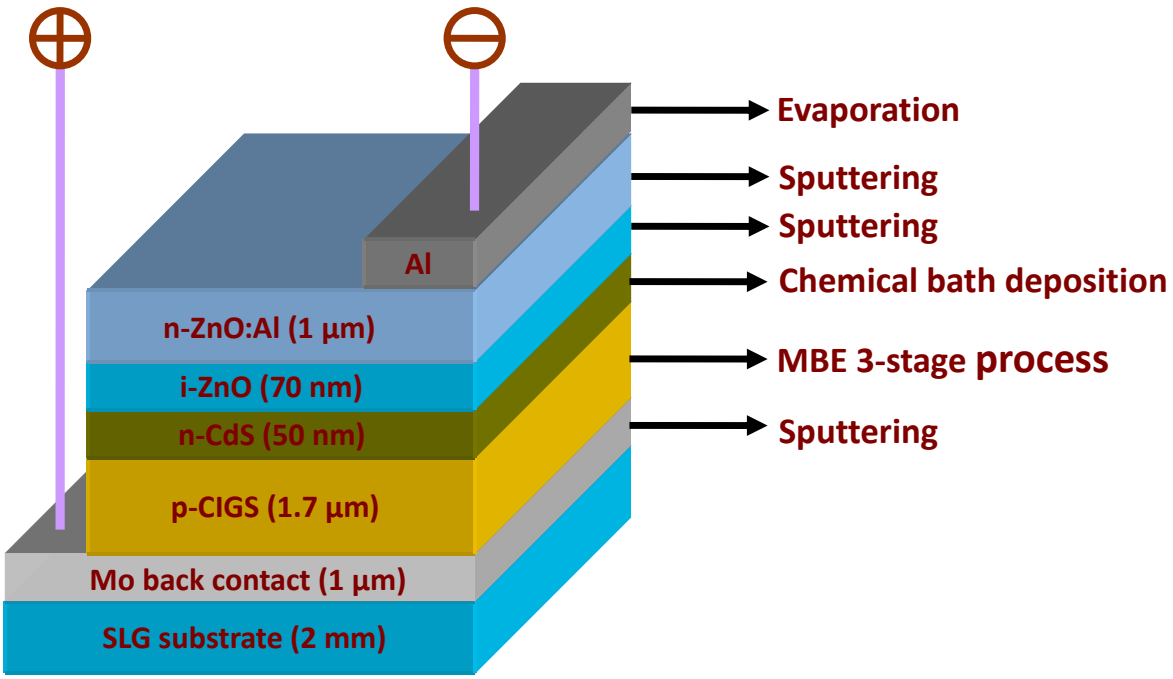

Fig. 1-14. Typical CIGS solar cell structure.

Glass substrate

Usually a sodium (Na) containing glass like soda-lime glass is taken as substrate for CIGS solar cells. It was recognized that, during absorber deposition, Na diffuses through the Mo layer into the absorber and has multiple positive influence on the material [1-29, 30, 31]. During growth, Na doping leads to a better morphology [1-32] by retarding of phase formation to higher temperatures [1-33]. In the material, it is mostly accumulated at grain boundaries [1-32]. There, the sodium leads presumably to passivation of grain boundaries and increases the p-type conductivity [1-34]. Another option instead of more or less uncontrolled sodium diffusion into the absorber layer, is the deposition of a Na diffusion barrier on top of the glass substrate and the providence of a defined amount of sodium in form of a precursor like NaF prior to or during deposition of the absorber layer [1-35, 36].

Molybdenum back contact

The molybdenum (Mo) is deposited on the glass substrate by RF magnetron sputtering method [1-37]. The metal does not diffuse into the absorber material, but forms a thin $MoSe_2$ film in presence of excess selenium during growth of CIGS in the Mo/Cu(In,Ga)Se_2 interface [1-38, 39]. Probably because of this layer, there is only a small potential barrier between molybdenum and CIGS, so that the back contact behaves as ohmic at room temperature.

Cu(In,Ga)Se_2 absorber layer

CIGS absorber layers in this study are grown by a three-stage process using a molecular beam epitaxy (MBE) system [1-37] as Fig. 1-15 shows. The three-stage growth method was developed where In, Ga, Se and Cu, Se are deposited alternatively with changing the Cu/III ratio [1-40], and by this method the most efficient CIGS solar cells to date were obtained [1-13]. Fig. 1-15 shows a schematic diagram for describing the three-stage growth process of CIGS layer. Fig. 16 (a) shows the temperature controlling of in the CIGS thin film during the three-stage growth process. Fig. 16 (b) shows the controlling of Cu/III ratio in the the three-stage growth process.

During stage-1, only In and Se (or In, Ga, and Se) are deposited at approximately 400°C, forming a (In, $Ga)_2Se_3$ (IGS) precursor film.

At the beginning of stage-2, the substrate temperature is increased to 520 °C. Only Cu-Se is deposited and the overall cation ratio Cu/III of the growing Cu-(In, Ga)-Se film is increasing continuously.

At stage-3, substrate temperature is maintained at 520 °C and again In, Ga and Se are deposited to make III-rich surface until the target composition of Cu/III=0.93 is reached.

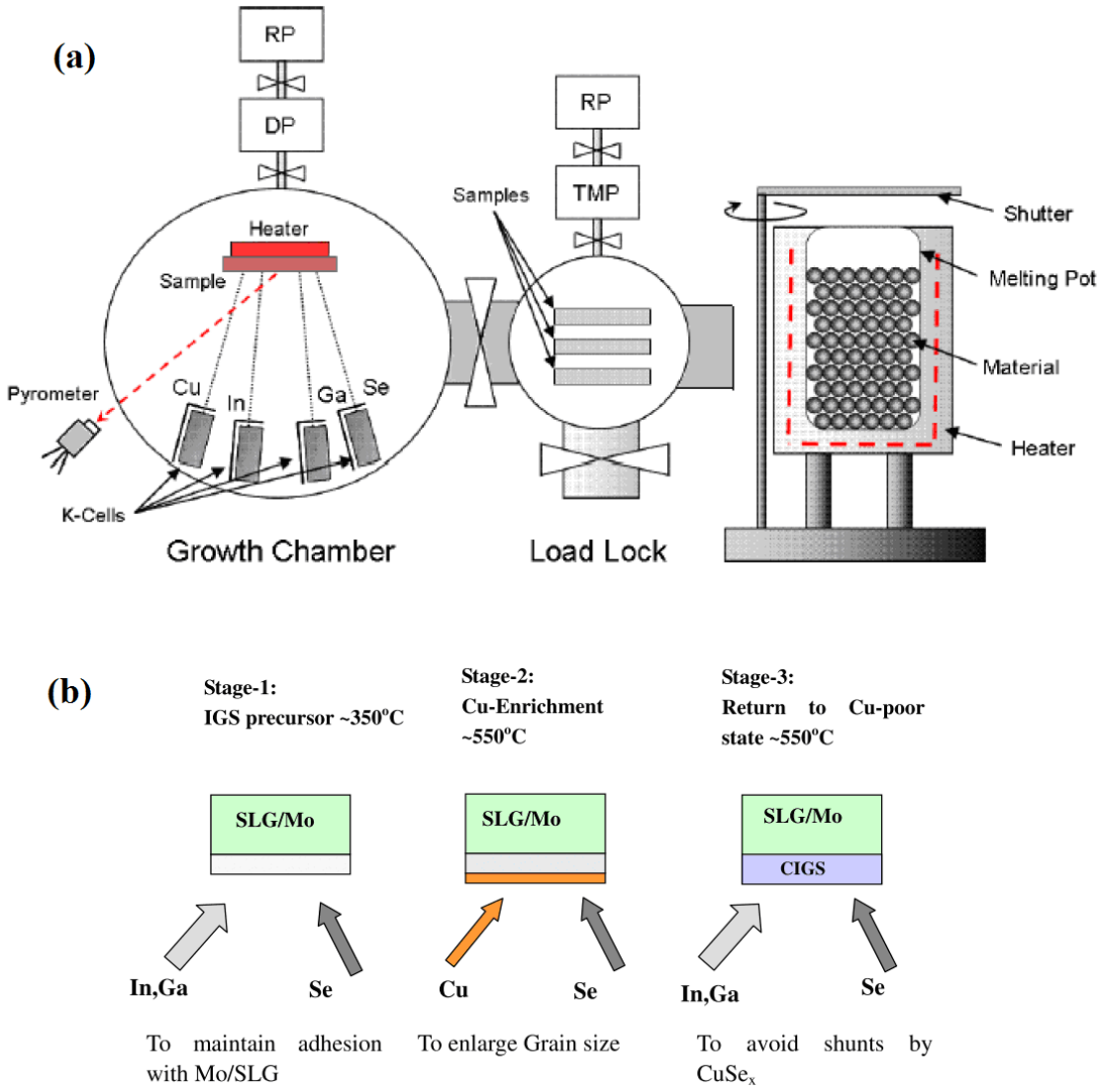

Fig. 1-15. (a) MBE system for CIGS growth, the right side shows the schematic diagram of a Knudsen-cell (K-cell); (b) Three-stage growth process of CIGS absorber layer. [1-41]

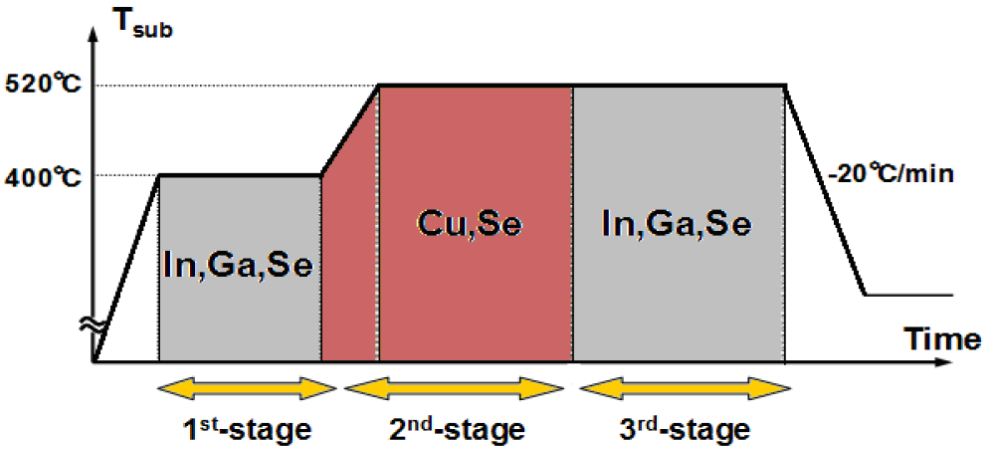

(a)

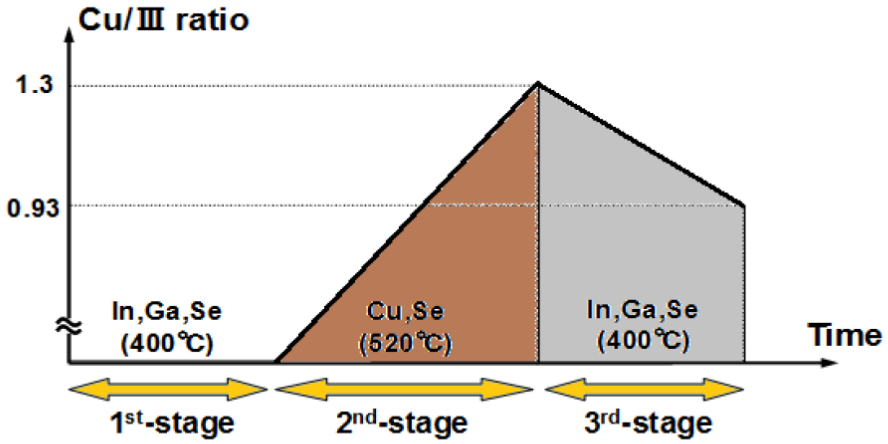

(b)

Fig. 1-16. (a) The temperature evolution of the substrate during the three-stage growth process of the CIGS thin film; (b) the controlling of Cu/III ratio in the three-stage growth process [1-41].

CdS buffer layer

CdS buffer layer deposited by Chemical Bath Deposition (CBD) has been being used for high efficiency standard CIGS solar cell. CBD is a non-vacuum process, which seems to be the best grown technique for CdS deposition [1-42]. Some of the beneficial effects of the CBD processed CdS buffer layer identified so far are removal of natural oxides from the CIGS surface [1-43] and protection of the CIGS layer from negative influences of the sputtering processes used to deposit the window layer.

Window layer (i-ZnO/Al:ZnO)

i- ZnO and n-ZnO:Al layers were deposited by sputtering at room temperature [1-37]. The n-doped zinc oxide provides a highly conductive front contact with a band gap large enough to be transparent in the relevant photon energy range [1-44.]. The band gap of i-ZnO is 3.4 eV [1-44] while the band gap of the aluminum doped zinc-oxide is a little larger [1-45]. The role of the resistive i-ZnO is still a matter of discussion. It was proposed that it reduces the impact of lateral inhomogeneities due to varying electrical properties of different crystallites [1-46, 47]. Maybe it also prevents the aluminum from diffusion into the absorber layer.

1.6 Defect physics in CIGS

1.6.1 Theoretical prediction

The defect structure of the ternary compounds $CuInSe_2$, $CuGaSe_2$ and their alloys, is of special importance because of the large number of possible intrinsic defects and the role of deep recombination centers for the performance of the solar cells [1-48]. The features that are somewhat special to the Cu-chalcopyrite compounds are the ability to dope these compounds with native defects, their tolerance to large off-stoichiometries, and the electrically neutral nature of structural defects in these materials. It is obvious that the explanation of these effects significantly contributes to the explanation of the photovoltaic performance of these compounds. Doping of $CuInSe_2$ is controlled by intrinsic defects. Samples with p-type conductivity are grown if the material is Cu-poor and annealed under high Se vapour pressure, whereas Cu-rich material with Se deficiency tends to be n-type [1-49, 50]. Thus, the Se vacancy V_{se} is considered to be the dominant donor in n-type material (and also the compensating donor in p-type material), and the Cu vacancy V_{Cu} the dominant acceptor in Cu-poor p-type material. Zhang et al. [1-51] has found that the defect formation energies for some intrinsic defects are so low by calculating the metal-related defects in $CuInSe_2$ and $CuGaSe_2$ that they can be heavily influenced by the chemical potential of the components (i.e., by the composition of the material) as well as by the electrochemical potential of the electrons. For V_{Cu} in Cu-poor and stoichiometric material, a negative formation energy is even calculated. This would imply the spontaneous formation of large numbers of these defects under equilibrium conditions. Low formation energies are also found for the antisite Cu_{In} in Cu-rich material (this defect is a shallow acceptor which would be responsible for the p-type conductivity of Cu-rich, non-Se-dificient $CuInSe_2$). The dependence of the defect formation energies on the electron Fermi level could explain the strong tendency of $CuInSe_2$ to self-compensation and the difficulties of achieving extrinsic doping. Table 1-1 summarises the ionization energies and the defect formation energies of the 12 intrinsic defects in $CuInSe_2$ [1-52]. The energies (bold values in Table 1-1) for V_{Cu}, V_{In}, Cu_i, Cu_{In}, In_{Cu}, are obtained from a first principle calculation [1-51] whereas the formation energies in italics (Table 1-1) and for the other defects are calculated from the macroscopic cavity model [1-53].

Table 1-1. Electronic transition energies and formation energies of the 12 intrinsic defects in $CuInSe_2$[1-52]

Defects (Transition energies and formation energies in eV)												
Transition	V_{Cu}	V_{In}	V_{Se}	Cu_i	In_i	Se_i	In_{Cu}	Cu_{In}	Se_{Cu}	Cu_{Se}	Se_{In}	In_{Se}
(-/0)	**0.03**	**0.17**						**0.29**				
	0.03	*0.04*	*0.04*[a]			*0.07*		*0.05*		*0.13*	*0.08*	
(-/2-)		**0.41**						**0.58**				
(2-/3-)		**0.67**										
(0/+)				**0.2**			**0.25**					
			0.11[b]	*0.08*	*0.07*		*0.04*		*0.06*			*0.09*
(+/2+)							**0.34**					
ΔE/eV	**0.60**	**3.04**		**2.88**			**3.34**	*1.54*				
	2.9	*2.8*	*2.6*	*4.4*	*9.1*	*22.4*	*1.4*	*1.5*	*7.5*	*7.5*	*5.5*	*5.0*

a) covalent, b) ionic

In Ref. [1-51], the formation energies of defect complexes such as ($2V_{Cu}$, In_{Cu}), (Cu_{In}, In_{Cu}), and ($2Cu_i$, Cu_{In}), where Cu_i is an interstitial Cu atom were also given. These formation energies are even lower that those of the corresponding isolated defects. The ($2V_{Cu}$, In_{Cu}) complex does not exhibit an electronic transition within the forbidden gap, in contrast to the isolated In_{Cu} anti-site, which is a deep recombination center. As the ($2V_{Cu}$, In_{Cu}) complex is most likely to occur in In-rich material, it can accommodate a large amount of excess In (or deficient Cu) and maintain the electrical performance of the material. Furthermore, ordered arrays of this complex can be thought as the building blocks of a series of Cu-poor Cu-In-Se compounds such as $CuIn_3Se_5$ and $CuIn_5Se_8$ [1-51].

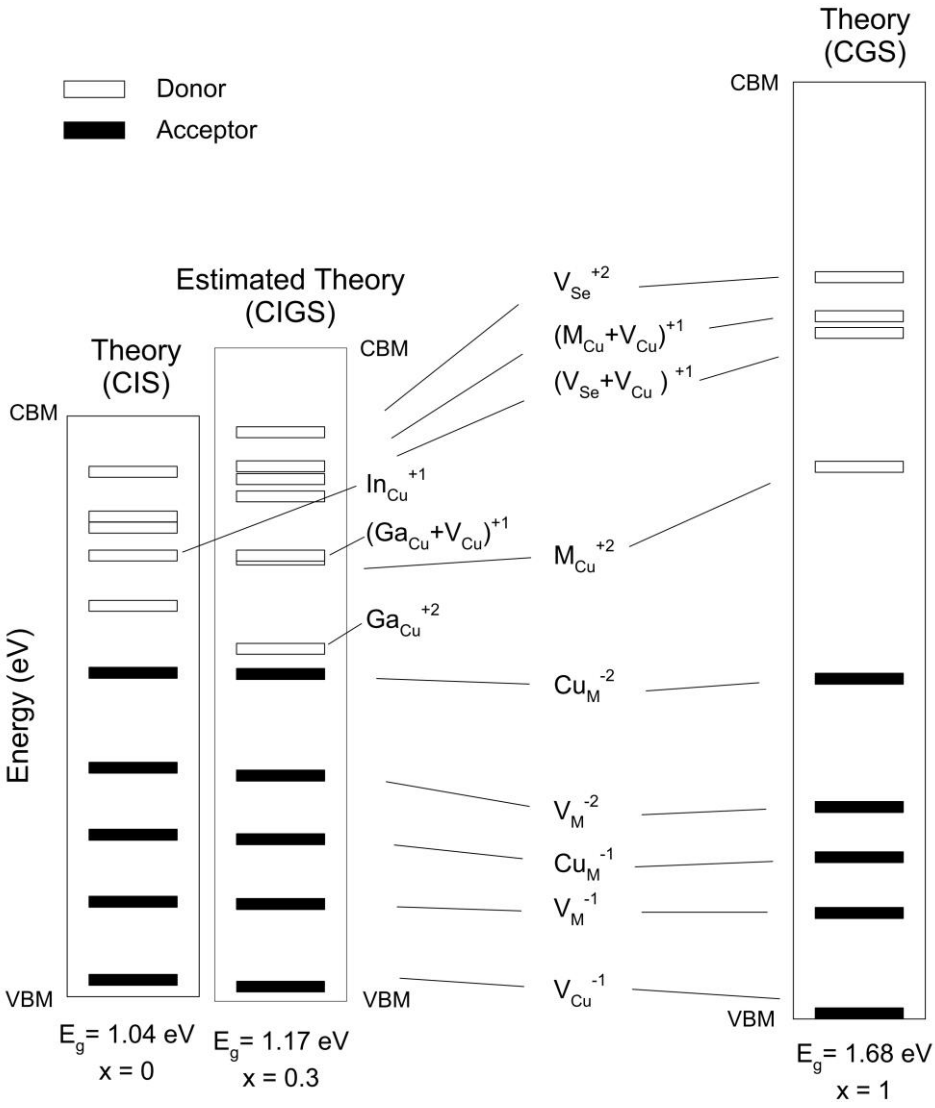

Fig. 1-17. Calculated defect levels in the CIS and CGS band gap [1-51, 54], and interpolated defect levels in CIGS. M pertains to Ga for CGS, In for CIS, In for CIGS donors, and either In or Ga in the case of acceptors in CIGS. Only the levels most likely to form in each material type are shown [1-55].

1.6.2 Experimental results

Experimentally, some dominant defects in photovoltaic grade (In-rich) polycrystalline films were investigated. The shallow acceptor level V_{Cu} (which lies about 30 meV above the valence band) is assumed to be the main dopant in this material. As compensating donors, the Se-vacancy V_{se} as well as the double donor In_{Cu} are considered. Two defects usually labeled as N1 and N2 are the major detected defects experimentally, N1 has been assigned by some groups to donor-like defects (electron traps) found at the interface of CIGS and the window layer with typical activation energies range from 50-200 meV [1-56, 57]. However, another group argued that [1-58] that N1 is not an energetically continuous interface state, but rather a bulk state. N2 was to typically assigned to acceptor-like defects (hole traps) with an activation energy generally ranging from 200-300 meV [1-56, 59]. Table 1-2 lists some typically reported activation energies of the defects detected in CIGS solar cells [1-55].

Table 1-2. Experimentally reported activation energies of the defects detected in CIGS solar cells [1-58]

Detection Method	Electron trap level (meV)	Hole trap level (meV)	Reference
AS	60, 70, 110		[1-60]
AS, DLTS	77		[1-56]
DLTS	90, ~100	270	[1-61]
AS	~100	105	[1-62]
AS	120-140	290	[1-63]
DLTS	200		[1-64]
AS, DLTS	347		[1-56]
AS		50, 75	[1-65]
AS		66, 74	[1-58]
AS		120-190	[1-66]
AS		~150, 187, ~200	[1-58]
DLTS		260	[1-64]
DLTS, AS & MPC		260-280	[1-67]
AS		280-330	[1-68]
AS		280	[1-59]
AS		~300	[1-62]
AS		400	[1-69]
AS, DLTS		470, 508	[1-56]
AS: Admittance Spectroscopy; DLTS: deep-level transient spectroscopy; MPC: modulated photocurrent			

An acceptor level at about 270-300 meV above the valence band, which is reported by several groups from deep-level transient spectroscopy [1-70] and admittance spectroscopy [1-71]. The importance of this transition results from the fact that its concentration is related to the open-circuit voltage of the device [1-72]. Also, an additional defect state in $Cu(In,Ga)Se_2$ at about 0.8 eV from the valence band was unveiled from Transient photocapacitance studies by Heath et al. [1-73] and the defect energy is independent of the Ga content in the alloy, this defect may act as an active recombination center since it is near the midgap especially for wide gap or high Ga content CIGS.

1.7 Motivation and objective of the research

One of the problems still existing in CIGS based solar cells is the energy loss problem for wide bandgap or high Ga concentration CIGS since the experimental efficiency of CIGS with wide bandgap is still much below the ideal predictions [1-74]. As Fig. 1-18 shows, the ideal band gap energy for a single-junction solar cell is predicted to be 1.4 eV, which corresponds to an Ga content x of about 0.70 [1-74, 75], however, most of the highest efficiencies reported which are in excess of 20% are based on CIGS with Ga content x of about 0.30, which corresponds to a bandgap energy of about 1.1 eV [1-13, 76, 77].

The saturation of open-circuit voltage in the wide bandgap region is one important factor to limit the efficiency [1-78], as Fig. 1-18 (b) shows, theoretically, the open-circuit voltages V_{oc} should follow a relation with the band gap according to V_{oc} = (E_g /q)-500 mV [1-61], where q is the elementary charge. As experimental results are consistent with this relation in the case of CIGS with narrow gap (E_g<1.2 eV), however, for wider gap CIGS (E_g<1.2 eV), the experimental results start to deviate with this relationship and as the gap becomes wider, the deviation becomes larger.

Defects may play significant role as they may act as active recombination centers to limit the open-circuit voltage as Ga content increases in CIGS films [1-62]. So in order to enhance the performance of the cell with high Ga content, the reduction of the carrier recombination and a removal of the defects in CIGS are indispensable. Our motivation focused on studying the mechanism that may decrease the efficiency of wide-bandgap CIGS solar cells [1-79].

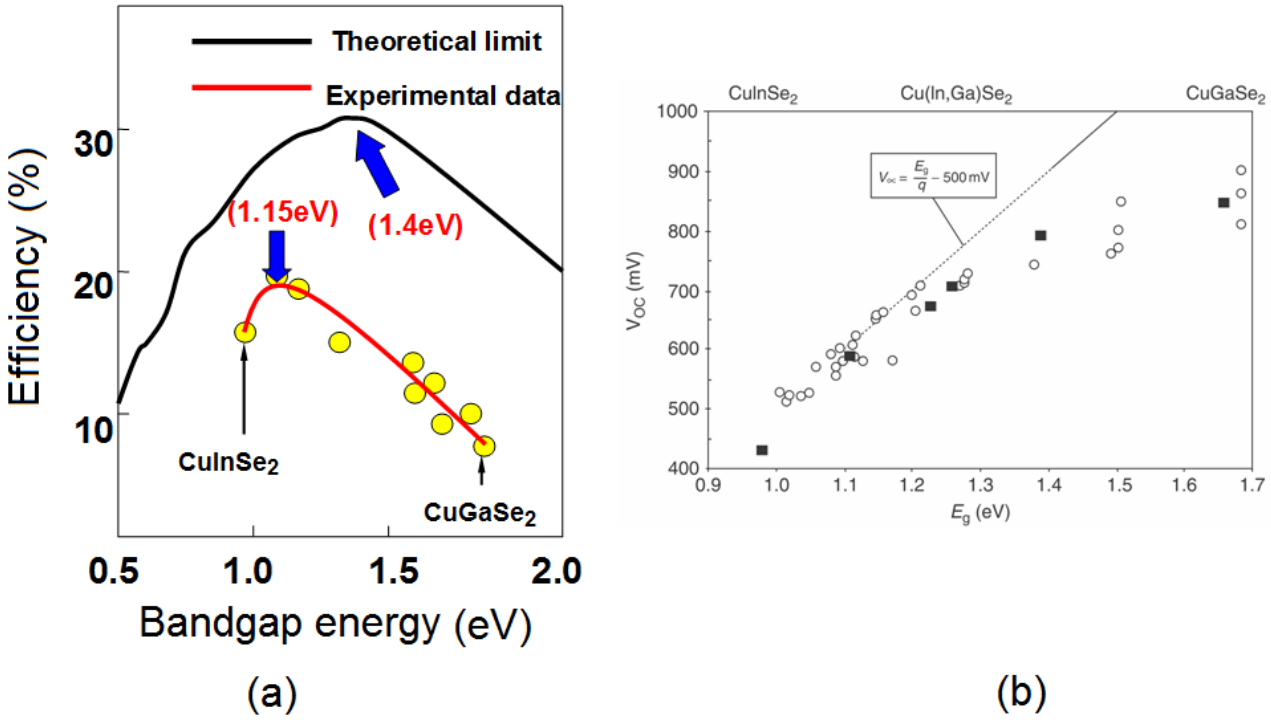

Fig. 1-18. (a) Theoretical efficiency of CIGS compared with the experimental obtained efficiency, (b) The saturation effect of V_{oc} for high bandgap CIGS

Considering above mentioned issues, we have set our objectives as follows:

(i) Study of the properties of defects existing in the CIGS thin films and find the correlation of the properties to the performance of CIGS solar cells as the Ga content varies.

(ii) Find the dominant defects (active recombination centers) that influence the the performance of CIGS solar cells as the Ga content varies.

(iii) Investigate the origins of the defects to conduct to develop high efficiency wide-gap CIGS solar cell.

1.8 Thesis Organization

This thesis mainly focuses on studying of defects especially deep-level defect in CIGS thin films with different Ga content, the possible correlation of the studied defects to the poor performance of the CIGS solar cells with high band gap or high Ga content would be discussed.

In this chapter, we have introduced our motivation and objective of this research. The properties of the CIGS material and solar cells are also introduced.

In chapter 2, the correlation of shallow-level defects to the performance of CIGS solar cells with varying Ga content will be discussed by using an admittance spectroscopy method.

In chapter 3, the deep-level defects which can not be detected by the admittance spectroscopy method would be measured by a sub-band gap optical method called transient photocapacitance spectroscopy method. The properties such as the position of the deep defects and the relative density versus Ga content will be discussed.

In chapter 4, the recombination properties of the determined 0.8 eV deep-level defect above the valence band in chapter 3 would be investigated by a two-wavelength excitation photocapacitance method, that is, whether this defect acts as an active recombination center.

In chapter 5, quantitative characterization of the 0.8 eV deep-level defect such as the absolute defect density, optical and thermal capture cross sections would be investigated by using a steady-state photocapacitance method and time-resolved photoluminescence method.

In chapter 6, the electronic structure of the 0.8 eV deep-level defect will be discussed based on the results of temperature dependent transient photocapacitance and steady-state photocapacitance.

In chapter 7, some possible origins of the 0.8 eV deep-level defect will be discussed by correlating the results from different experiments.

Finally, chapter 8 will give conclusions about the investigations regarding the deep-level defects in CIGS solar cell.

References

[1-1] British petroleum. Statistical review of world energy, June 2011
http://www.bp.com/content/dam/bp-country/de_de/PDFs/brochures/statistical_review_of_world_energy_full_report_2011.pdf

[1-2] German Advisory Council on Global Change.

[1-3] Trends in Photovoltaic Applications, Survey report of selected IEA countries between 1992 and 2011, IEA report 2012.

[1-4] PV Status Report 2010, office for official Publications of the European Union, Brussels, 2010.

[1-5] M.A. Green, K. Emery, Y. Hishikawa, W. Warta, E. D. Dunlop, Solar cell efficiency tables (version 44), Prog. Photovolt: Res. Appl. **22** (2014) 701.

[1-6] M.A. Green, *Third-Generation Photovoltaics: Advanced Solar Energy Conversion*. Springer, Berlin, 2006.

[1-7] International Energy Agency (IEA), 2012. Technology Roadmap: Solar photovoltaic energy (published 2010), May 2012. http://www.iea.org

[1-8] X. Gu, X.Yu, K. Guo, L. Chen, D. Wang, D. Yang, Seed-assisted cast quasi-single crystalline silicon for photovoltaic application: towards high efficiency and low-cost silicon solar cells. Sol. Energy Mater. &Solar Cells **101** (2012) 95.

[1-9] S. Delbos, Kesterite thin films for photovoltaics: a review. EPJ Photovolt. **3** (2012) 35004.

[1-10] K. W. Mitchell, Status of new thin film photovoltaic technologies. Ann. Rec. Mater. Sci. **12** (1982) 401-415.

[1-11] S. Mehta, GTM Research, Thin Film 2010: Market Outlook to 2015, March 2010.

[1-12] R. Noufi, K. Zweibel, High-Efficiency CdTe and CIGS Thin-Film Solar Cells: Highlights and Challenges, Sci. 22-34 (2006)1061.WPEC4, Hawaii

[1-13] http://www.zsw-bw.de/uploads/media/pr12-2014-ZSW-WorldrecordCIGS.pdf

[1-14] S. M. Sze and Kwok K. Ng, *Physics of semiconductor devices*, John Wiley & Sons, Hoboken, 2006.

[1-15] Sheng S. Li, *Semiconductor Physical Electronics*, Springer, Berlin, 2006

[1-16] http://www.nrel.gov/pv/

[1-17] J. L. Shay and J. H. Wernick, *Ternary Chalcopyrite Semiconductors: Growth, Electronic Properties and Applications*. Oxford: Pergamon Press, 1975.

[1-18] S. R. Kodigala, *Thin Films and Nanostructures: Cu(In1-xGax)Se2 Based Thin Film Solar Cells*, Elsevier Inc., 2010.

[1-19] R. Scheer and H. W. Schock, *Chalcogenide Photovoltaics: Physics, Technologies, and Thin Film Devices*. Wiley-VCH, Berlin, 2011.

[1-20] A. Luque and S. Hegedus, *Handbook of Photovoltaic Science and Engineering*, John Wiley & Sons, Ltd, 2003, chapter 13.

[1-21] S. Ishizuka, K. Sakurai, A. Yamada, H. Shibata, K. Matsubara, M. Yonemura, S. Nakamura, H.

Nakanishi, T. Kojima and S. Niki, Progress in the Efficiency of Wide-Gap $Cu(In_{1-x}Ga_x)Se_2$ Solar Cells Using CIGSe Layers Grown in Water Vapor. Jpn. J. Appl. Phys. **44** (2005) L679–682.

[1-22] S.-H. Wei, A. Zunger, Band offsets and optical bowings of chalcopyrites and Zn-based II-VI alloys, J. Appl. Phys. **78** (1995) 3846-3856.

[1-23] M. I. Alonso, K. Wakita, J. Pascual, M. Garriga and N. Yamamoto, Optical functions and electronic structure of $CuInSe_2$, $CuGaSe_2$, $CuInS_2$, and $CuGaS_2$. Phys. Rev. B **63** (2001) 075203.

[1-24] S.-H. Wei, A. Zunger, Calculated natural band offsets of all II–VI and III–V semiconductors: Chemical trends and the role of cation *d* orbitals, Appl. Phys. Lett. **72** (1998) 2011–2013.

[1-25] M. Turcu, I. M. Kotschau and U. Rau, Band alignments in the $Cu(In,Ga)(S,Se)_2$ alloy system determined from deep-level defect energies, Appl. Phys. A **73** (2001) 769.

[1-26] R. D. Tomlins, A. E. Hill, and R. D. Pilkington (eds.), Ternary and multinary compounds. Proceedings of the 11th International Conference on Ternary and Multinary Compounds, ICTMC-11, University of Salford, Institute of Physics Series Number 152, 8–12 September 1997.

[1-27] R. Herberholz, U. Rau, H. W. Schock, T. Haalboom, T. Godecke, F. Ernst, C. Beilharz, K. W. Benz and D. Cahen, Phase segregation, Cu migration and junction formation in $Cu(In, Ga)Se_2$. EPJ-Appl. Phys. **6** (1999) 131–139.

[1-28] T. Unold and C. A. Kaufmann, *Reference Module in Earth Systems and Environmental Sciences Comprehensive Renewable Energy*, (2012) pp.399-422.

[1-29] S. Ishizuka, A. Yamada, M. M. Islam, H. Shibata, P. Fons, T. Sakurai, and S. Niki, Na-induced variations in the structural, optical, and electrical properties of $Cu(In, Ga)Se_2$ thin films. J. Appl. Phys., **106** (2009) 034908.

[1-30] L. Kronik, D. Cahen, and H. W. Schock, Effects of Sodium on Polycrystalline $Cu(In,Ga)Se_2$ and Its Solar Cell Performance, Adv. Mater. **10** (1998) 31.

[1-31] S. H. Wei, S. B. Zhang, and A. Zunger, Effects of Na on the electrical and structural properties of $CuInSe_2$, J. Appl. Phys. **85** (1999) 7214.

[1-32] M. Bodegard, L. Stolt, and J. Hedstrom, in Proc 12th European Phot0voltaic Solar Energy Conf., UK.

[1-33] D. Wolf, G. M¨uller, W. Stetter, and F. Karg, in Proc. 2nd World Conf.on Photovolt. Energy Conf., p. 2426, E. C. Joint Res.Centre, Luxembourg, 1998.

[1-34] M. Ruckh, D. Schmid, M. Kaiser, R. Schaffler, T. Walter, and H. W. Schock, in Proc. 1st World Conf. on Solar Energy Conversion, p. 156, IEEE, New York, 1994.

[1-35] V. Lyahovitskaya, Y. Feldman, K. Gartsman, H. Cohen, C. Cytermann, and D. Cahen, Na effects

on $CuInSe_2$: Distinguishing bulk from surface phenomena, J. Appl. Phys. **91**(2002) 4205.

[1-36] D. Rudmann, G. Bilger, M. Kaslin, F. J. Haug, and H. Zogg and A. N. Tiwari, Effects of NaF coevaporation on structural properties of $Cu(In,Ga)Se_2$ thin films, Thin Solid Films **431** (2003) 37.

[1-37] S. Ishizuka, K. Sakurai, A. Yamada, K. Matsubara, P. Fons, K. Iwata, S. Nakamura, Y. Kimura, T. Baba, H. Nakanishi, T. Kojima, S. Niki, Fabrication of wide-gap $Cu(In_{1-x}Ga_x)Se_2$ thin film solar cells: a study on the correlation of cell performance with highly resistive i-ZnO layer thickness, Solar Energy Materials & Solar Cells **87** (2005) 541–548.

[1-38] L. Assmann, J.C. Bernède, A. Drici, C. Amory, E. Halgand, and M. Morsli, Study of the Mo thin films and Mo/CIGS interface properties, Appl. Surf. Sci. **246** (2005) 159.

[1-39] M. Nishitani, N. Kohara, T. Negami, and T. Wada, $MoSe_2$ layer formation at $Cu(In,Ga)Se_2$/Mo Interfaces in High Efficiency $Cu(In_{1-x}Ga_x)Se_2$ Solar Cells, Jpn. J. Appl. Phys. **37** (1998) L71.

[1-40] A. M. Gabor, J. R. Tuttle, D. S. Albin, M. A. Contreras, R. Noufi, A. M. Hermann, High-efficiency $CuIn_xGa_{1-x}Se_2$ solar cells made from $(In_x,Ga_{1-x})_2Se_3$ precursor films, Appl. Phys. Lett. **65** (1994) 198–200.

[1-41] M. M. Islam, *Growth and Defect Characterization of $Cu(In_{1-x}Ga_x)Se_2$ Thin Film and Fabrication of Solar Cell*, PhD thesis, University of Tsukuba, 2010.

[1-42] N. G. Dhere, D. L. Waterhouse, K. B. Sundaram, O. Melendez, N. R.Parik, and B. Patnaik, Studies on chemical bath deposited cadmium sulphide films by buffer solution technique, J. Mater. Sci. Mater. Electronics **6** (1995) 52.

[1-43] J. Kessler, K. O. Velthaus, M. Ruckh, R. Laichinger, H. W. Schock, D. Lincot, R. Ortega, and J. Vedel, in Proc. 6th Intern. Photovolt. Science Eng. Conf., edited by B. K. Das and S. N. Signh, p. 1005, Oxford Publ., New Delhi, 1992.

[1-44] S. M. Sze, *Physics of Semiconductor Devices*, Wiley, New York, 1981.

[1-45] J. Mass, P. Bhattacharya, and R. S. Katiyar, Effect of high substrate temperature on Al-doped ZnO thin films grown by pulsed laser deposition, Mater. Sci. Eningeer. B **103** (2003) 9.

[1-46] U. Rau and U. Schmidt, Electronic properties of ZnO/CdS/$Cu(In,Ga)Se_2$ solar cells — aspects of heterojunction formation, Thin Solid Films **387** (2001) 141.

[1-47] D. Eich, U. Herber, U. Groth, U. Stahl, C. Heske, M. Marsi, M. Kishinova, W. Riedel, R. Fink, and E. Umbach, Lateral inhomogeneities of $Cu(In,Ga)Se_2$ absorber films, Thin Solid Films **361** (2000) 258.

[1-48] A. McEvoy, T. Markvart, L. Castaner, *Solar Cells: Materials, Manufacture and Operation*, Elsevier Inc., 2012, chapter 4.

[1-49] P. Migliorato, J. L. Shay, H. M. Kasper and S. Wagner, Analysis of the electrical and luminescent

properties of $CuInSe_2$, J. Appl. Phys., **46** (1975) 1777.

[1-50] R. Noufi, R.Axton, C. Herrington, and S. K. Deb, Electronic properties versus composition of thin films of $CuInSe_2$, Appl. Phys. Lett., **45** (1984) 668.

[1-51] S. B. Zhang, S. H. Wei, A. Zunger, and H. Katayama-Yoshida, Defect physics of the $CuInSe_2$ chalcopyrite semiconductor. Phys. Rev B, **57** (1998) 9642.

[1-52] U. Rau, H. W. Schock, Electronic properties of $Cu(In,Ga)Se_2$ heterojunction solar cells–recent achievements, current understanding, and future challenges, Appl. Phys. A **69** (1999) 131–147.

[1-53] H. Neumann, Vacancy formation in $A^IB^{III}C_2^{VI}$ chalcopyrite semiconductors, Cryst. Res. Technol. **18** (1983.) 901.

[1-54] S.-H. Wei, S. B. Zhang, and A. Zunger, Effects of Ga addition to $CuInSe_2$ on its electronic, structural, and defect properties, Appl. Phys. Lett. **72** (1998) 3199.

[1-55] P. K. Johnson, *The effect of trapping defects on CIGS solar-cell performance*, PhD thesis, Colorado State University, 2003.

[1-56] M. Turcu, I. M. Kötschau, and U. Rau, Composition dependence of defect energies and band alignments in the $Cu(In_{1-x}Ga_x)(Se_{1-y}S_y)_2$ alloy system, J. Appl. Phys. **91** (2002) 1391.

[1-57] T. Sakurai, , N. Ishida, S. Ishizuka, M. M. Islam, A. Kasai, K. Matsubara, K. Sakurai, A. Yamada, K. Akimoto, and S. Niki. Effects of annealing under various atmospheres on electrical properties of Cu(In, Ga)Se_2 films and CdS/Cu(In, Ga)Se_2 heterostructures. Thin Solid Films **516** (2008) 7036.

[1-58] J. T. Heath, *Electronic Transitions in the Bandgap of Copper Indium Gallium Diselenide Polycrystalline Thin Films*, PhD thesis, University of Oregon, 2002.

[1-59] G. Hanna, A. Jasenek, U. Rau, and H. W. Schock, Influence of the Ga-content on the bulk defect densities of Cu (In,Ga)Se_2, Thin Solid Films **387** (2001) 71.

[1-60] A. Niemegeers, M. Burgelman, R. Herberholz, U. Rau, D. Hariskos and H. W. Schock, Model for Electronic Transport in $Cu(In,Ga)Se_2$ Solar Cells, Prog. Photovoltaics: Res. Appl. **6** (1998) 407.

[1-61] R. N. Bhattacharya, A. Balcioglu, K. Ramanathan, W. K. Batchelor, and R. K. Ahrenkiel, Proc. of the 16th European Photovoltaic Solar Energy Conference (2000).

[1-62] G. Hanna, A. Jasenek, U. Rau, and H. W. Schock, Open circuit voltage limitations in $CuIn_{1-x}Ga_xSe_2$ thin film solar cells dependence on alloy compositon, phys. Stat. sol. (a) **179** (2000) R7.

[1-63] U. Rau, D. Braunger, R. Herberholz, H. W. Schock, J. F. Guillemoles, L. Kronik, and D. Cahen, oxygenation and air-annealing effects on the electronic properties of $Cu(In,Ga)Se_2$ films and devices, J. Appl. Phys. **86** (1999) 497.

[1-64] P. Zabierowski and M. Igalson, Thermally assisted tunnelling in Cu(In,Ga)Se_2-based photovoltaic devices, Thin Solid Films **361** (2000) 268.

[1-65] U. Rau, M. Schmitt, F. Engelhardt, O. Seifert, J. Parisi, W. Riedl, J. Rimmasch and F. Karg, Impact of Na and S incorporation on the electronic transport mechanisms of Cu(In,Ga)Se_2 solar cells, Solid State Commun. **107** (1998) 59.

[1-66] M. Schmitt, U. Rau, and J. Parisi, Proc. of the 13th European Photovoltaic Solar Energy Conference (1995).

[1-67] M. Burgelman, F. Engelhardt, J. F. Guillemoles, R. Herberholz, M. Igalson, R. Klenk, M. Lampert, T. Meyer, V. Nadenau, A. Niemegeers, J. Parisi, U. Rau, H. W. Schock, M. Schmitt, O. Seifert, T. Walter and S. Zott, Defects in Cu(In, Ga)Se_2 semiconductors and their role in the device performance of thin-film solar cells, Prog. Photovoltaics: Res. Appl., **5** (1997) 121.

[1-68] M. Schmitt, U. Rau, J. Parisi, J. Rimmasch, and F. Karg, Characterizing Plasma-exposed $In_{0.52}Al_{0.48}As$ Surface Using Photoreflectance-, Raman-, and Photoluminescence Spectra Method, Cryst. Res. Technol. **31**(1996)119.

[1-69] I. M. Kötschau, M. Turcu, U. Rau, and H. W. Schock, Mat. Res. Soc. Symp. Proc. 668 (2001).

[1-70] M. Igalson, and H. W. Schock, The metastable changes of the trap spectra of $CuInSe_2$-based photovoltaic devices. J. Appl. Phys., **80** (1996) 5765.

[1-71] T. Walter, R. Herberholz, C. Mtiller, and H. W. Schock, Determination of defect distributions from admittance measurements and application to Cu(In,Ga)Se_2 based heterojunctions, J. Appl. Phys., **80** (1996) 4411.

[1-72] R. Herberholz, V. Nadenau, U. Riihle, C. Koble, H. W. Schock, and B. Dimmler, Prospects of wide-gap chalcopyrites for thin film photovoltaic modules. Solar Energy Mater. Solar Cells, **49** (1997) 227.

[1-73] J. T. Heath, J. D. Cohen, W. N. Shafarman, D. X. Liao, A. A. and Rockett, Effect of Ga content on defect states in $CuIn_{1-x}Ga_xSe_2$ photovoltaic devices, Appl. Phys. Lett., **80** (2002) 4540.

[1-74] S. Niki, M. Contreras, I. Repins, M. Powalla, K. Kushiya, S. Ishizuka, and K. Matsubara, CIGS absorbers and processes, Prog. Photovoltaics **18** (2010) 453-466.

[1-75] W. Shockley and H. J. Queisser, Detailed Balance Limit of Efficiency of p‐n Junction Solar Cells, J. Appl. Phys. **32** (1961) 510.

[1-76] P. Jackson, D. Hariskos, E. Lotter, S. Paetel, R. Wuerz,R. Menner, W. Wischmann and M. Powalla, New world record efficiency for Cu(In,Ga)Se_2 thin-film solar cells beyond 20%, Prog. Photovoltaics **19** (2011) 894–897.

[1-77]I. Repins, M. A. Contreras, B. Egaas, C. DeHart, J. Scharf, C. L. Perkins, B. To, and R. Noufi, 19·9%-efficient ZnO/CdS/CuInGaSe^2 solar cell with 81·2% fill factor, Prog. Photovoltaics **16** (2008) 235-239.

[1-78] S.R. Kodigala et al., *Thin Films and Nanostructures: CIGS based thin film solar cells*, Elsevier Inc., 2010, chapter 1.

[1-79] S. Ishizuka, A. Yamada, H. Shibata, and S. Niki, Grand Renewable Eenergy 2014, Tokyo, Japan (2014) O-Pv11-2.

Chapter 2 Shallow-level Defect Characterization by Admittance Spectroscopy

2.1 Principle of Admittance Spectroscopy

The band diagram of a typical CIGS/CdS/ZnO hetero-junction solar is shown in Fig. 2-1. The width of the space charge region (SCR) in the CIGS absorber material is w_p. The quantities E_C, E_T, E_V, and E_F denote the conduction band, trap of defect level, valence band, and the Fermi energy, respectively. Starting from the band diagram in Fig. 2-1 we now discuss the admittance of this hetero-junction. V_{bi} is the built-in voltage.

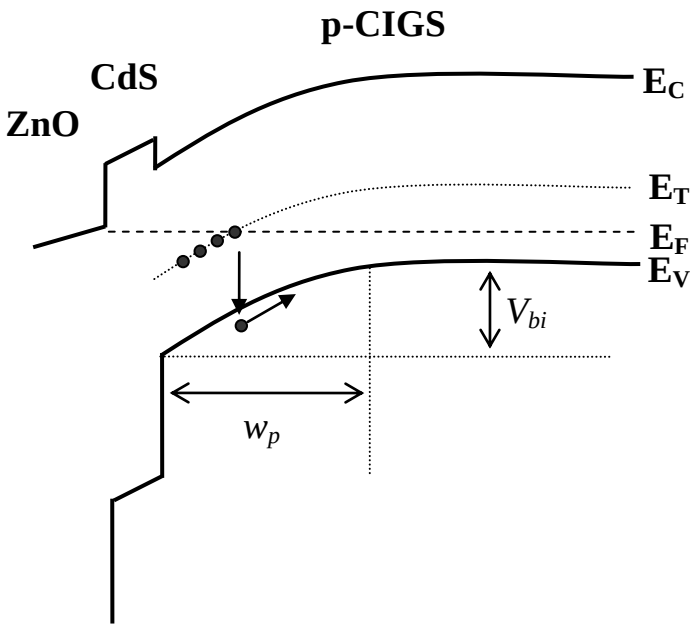

Fig. 2-1 Equilibrium band diagram of a CIGS/CdS/ZnO heterostructure.

Admittance is a technique which involves the measurement of admittance, i.e., capacitance C and conductance G of a rectifying junction as a function of frequency ω (angular). The complex admittance is defined as

$$Y(\omega)=G(\omega)+i\omega C(\omega) \tag{2-1}$$

where the real and imaginary part of $Y(\omega)$ are related by the Kramers-Kronig relations [2-1], and both $G(\omega,T)$ and $C(\omega,T)$ spectrums contain completely the same information of the full spectrum. In the following, only the capacitance $C(\omega)$ will be discussed. Admittance spectroscopy investigates the frequency and temperature dependence of the capacitance $C(\omega,T)$ of a rectifying junction.

The junction capacitance, in most simple case, is given by the space charge capacitance C_{SCR}. For a Schottky contact on p-type semiconductor material or an n^+p junction C_{SCR} (per unit area) can simply be given as [2-2],

$$C_{SCR} = \frac{\varepsilon_s}{w} = \sqrt{\frac{\varepsilon_s q N_A}{2V_{bi}}} \tag{2-2}$$

where w is the width of space charge region (in our case, the space charge region in the n-type CdS buffer layer and n-type ZnO window layer was neglected since the width was very small compared to the CIGS layer, thus, we gave a rough approximation $w=w_p$ in Fig. 2-1), ε_s is the dielectric constant of the semiconductor, V_{bi} is the built-in voltage, N_A is the acceptor concentration and q is the elementary charge. The response of majority carriers (holes here) in the valence band at a measurement frequency ω is limited by the dielectric relaxation time [2-3, 4],

$$\omega_D = \frac{1}{\tau_D} = \frac{\sigma}{\varepsilon_s} = \frac{qp\mu_p}{\varepsilon_s} = \frac{qN_V\mu_p}{\varepsilon_s}\exp(-\frac{E_F - E_V}{kT}) \tag{2-3}$$

where σ is the conductivity, which is the is the product of mobility μ_p and concentration p of the holes. N_V is the effective density of states in the valence band. The hole concentration p in the Boltzmann approximation is a function of the energetic distance of the Fermi energy E_F from the valence band energy E_V. When angular modulation frequency $\omega=2\pi f$ exceeds $1/\tau_D$, the majority carriers can not respond to the measurement frequency. This happens usually at low temperatures when $\omega>\omega_D$, the free carriers cannot follow the external excitation and the semiconductor acts as a dielectric. The capacitance measured at such frequency is the geometric capacitance $C_{geo}=\varepsilon_s/d$, where in our case, d is the distance between the molybdenum back contact and the ZnO window layer.

Now, without the limitation of the dielectric relaxation time ($\omega_D > \omega$), which occurs usually in the condition of lower frequencies and/or higher temperatures, electronically active traps in the SCR of the n+P junction contribute to the capacitance spectrum. In case of this, the occupation of trapping levels located in the Fermi level E_F changes with the application of an ac signal. Then, the contribution of a single majority trap level to the junction is [2-5],

$$C = C_{SCR}(\omega) + \frac{C_{lf} - C_{SCR}}{1 + \omega^2\tau^{*2}} \tag{2-4}$$

where C_{lf} is the capacitance at low frequency and depends on the trap density N_T and N_A in case of p-type material. The time constant τ^* is generally a function of N_A, N_T and the width of the SCR [2-5]. In the limit of small trap concentrations, *e.g.* $N_T << N_A$, the time constant approximates the value $\tau^*=1/\omega_o$, where ω_o is the inflection frequency of the electronic transition [2-6]. ω_o was simply defined as [2-7, 8],

$$\omega_o = 2N_V\upsilon_{th}\sigma_p \exp(-E_a/kT) = 2\xi_o T^2 \exp(-E_a/kT) \tag{2-5}$$

where σ_p represents the capture cross section for holes, υ_{th} is the thermal velocity, N_V is the effective density of states in the valence band and E_a is the activation energy of the defect with respect to the corresponding band edge (E_T-E_V in Fig. 2-1). ξ_o is the emission factor which contains all the temperature independent parameters.

Hence, in the case of a p-type semiconductor, hole traps within the space charge region having an energetic distance $E_a= E_T$-E_V to the valence band can be charged and discharged at frequencies $\omega<\omega_o$.

When the angular frequency of ac signal is smaller than the inflection frequency ($\omega<\omega_o$), the occupation of the trap level can follow the applied ac signal. Hence, the trap level contributes to the total capacitance.

This additional capacitance can be written as a function of the applied ac signal as,

$$C_{Trap} \propto \frac{\omega_o^2(T)}{\omega_o^2(T)+\omega^2} = \frac{1}{1+\left(\frac{\omega}{\omega_o(T)}\right)^2} \tag{2-6}$$

Fig. 2-2 shows the contribution of trap to the capacitance, it is very clear to see that the inflection frequency ω_o corresponds to minima of $\omega\frac{dC}{d\omega}$ versus ω variation.

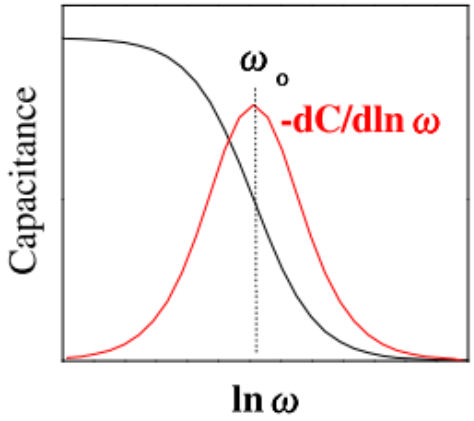

Fig. 2-2 The contribution of trap charge to the capacitance and the inflection frequency ω_o

The analytical calculation of the capacitance spectrum for a semiconductor with more than one trap level or a distribution of traps requires a more complex theory [2-9]. Walter et al.[2-10] developed a model which allows to directly determine the energetic distribution of defects $N_T(E)$ from experimentally obtained capacitance data $C(\omega,T)$ using differentiated capacitance spectra. This model yields a useful visualization of the energetic distribution of trap states for the case of small trap densities $N_T(E)<<N_A$. The defect density distribution with energy scale is expressed as [2-10],

$$N_T(E_a) = -\frac{2V_{bi}^{3/2}}{wkT\sqrt{q}\sqrt{qV_{bi}-(E_g-E_a)}} \cdot \frac{dC}{d\ln\omega} \tag{2-7}$$

where E_g is the band gap energy.

2.2 Experimental

Admittance spectroscopy measurements were carried out to determine the density of states and activation energy of traps by varying frequency (*f*) and temperature (*T*). We also analyze the electrical properties of the junctions by capacitance-voltage (C-V) and current-voltage (I-V) measurements. Device structure for admittance measurement is n-ZnO/i-ZnO/CdS/CIGS/Mo/SLG.

2.2.1 Experimental Setup

Fig. 2-1 shows the basic setup for the admittance spectroscopy measurements. CIGS solar cell samples were fixed on a copper plate in a cryostat chamber. Cooling of the samples was done by using a Helium compressor, and heating and stabilizing the samples' temperature were controlled by a temperature controller (Model 9700, Scientific Instruments). The temperature was controlled in the range of 10 K~340 K. The capacitance was measured using an LCR meter (Agilent 4284A), with the ac frequencies varying between 1 kHz and 1 MHz.

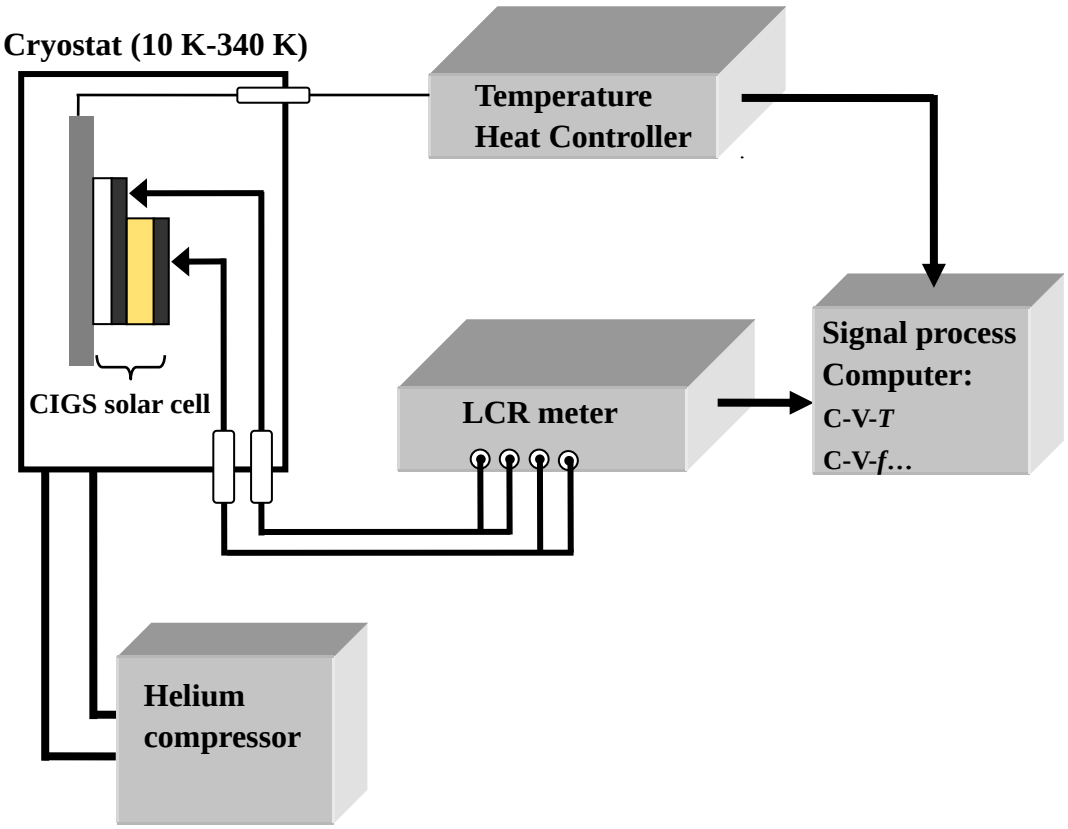

Fig. 2-3 Basic setup for admittance spectroscopy measurement

2.2.2 *C(f, T)* and Arrhenius plot

Typical capacitance spectra measured in the frequency range between 100 Hz and 1 MHz and in the temperature range between 20 K and 340 K in steps of 20 K are shown in Fig. 2-4. Below 60 K, the capacitance changes only slightly in the whole frequency range. The value for the capacitance below 60 K and 1 MHz is attributed to the depletion region capacitance. Capacitance steps observed above 60 K are attributed to the release of trapped charges.

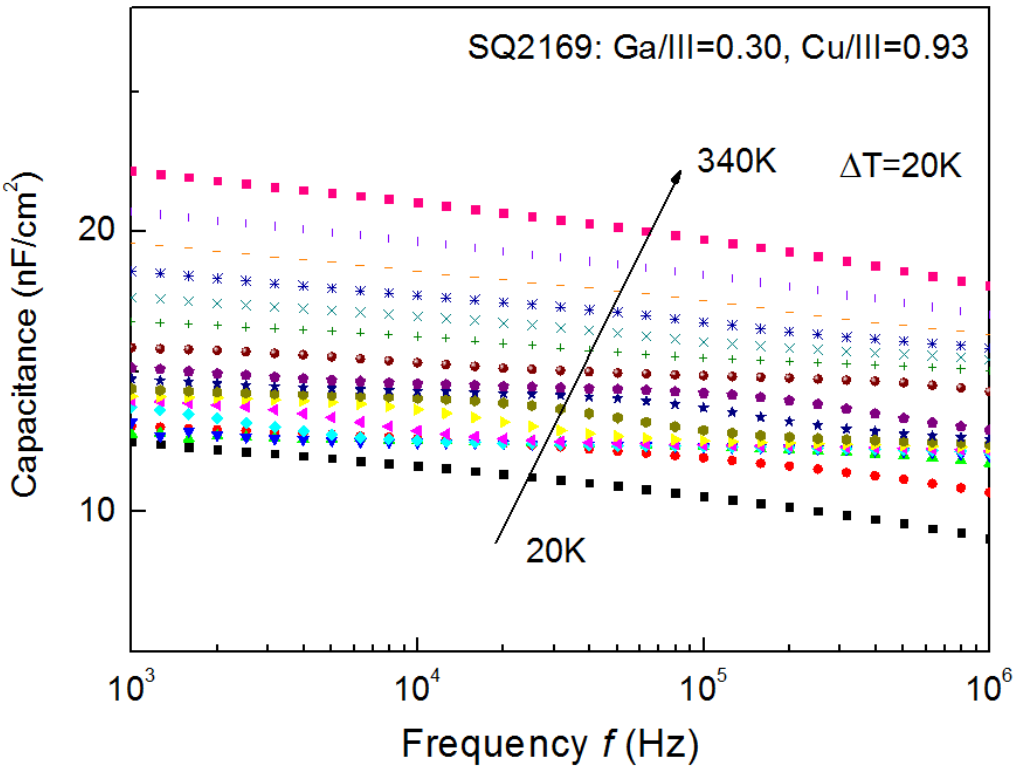

Fig. 2-4 Capacitance spectra *C(f, T)* of a typical Cu(In,Ga)Se_2 solar cell

In order to analyze this step, the derivative of the capacitance spectra with respect to frequency is calculated. The inflection frequency ω_o for the trap level as a function of temperature is determined from the minima position of the frequency in a plot of $dC/dln\omega$ versus ω (not shown here, but the principle is shown in Fig. 2-2).

Admittance spectroscopy measures dc/dlnω as a function of temperature in the 1kHz-1MHz of frequency range. Fig. 2-5 shows a typical admittance spectroscopy of a CIGS thin film solar cell with Ga content of 0.30. Peak α, β and ζ are the maxima of corresponding *-dc/dlnω* versus *ω* curve or inflection frequency ω_o that is appeared at a particular temperature. These peaks corresponds to a particular defect level either inside the band gap of the CIGS absorber layer or/and at the CIGS/CdS interface.

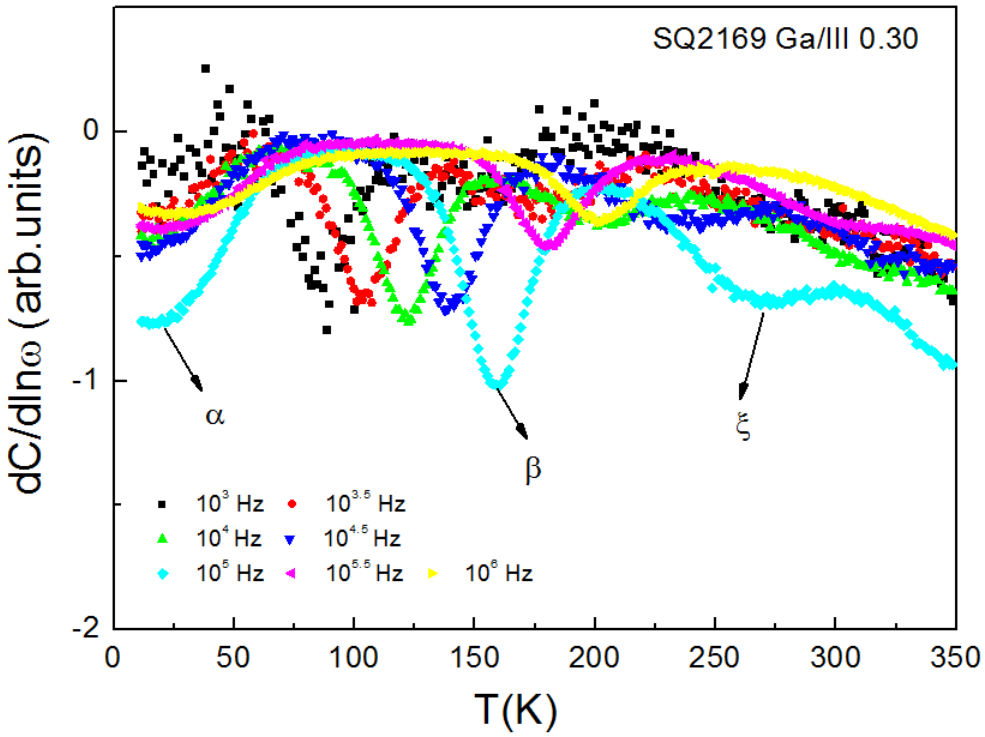

Fig. 2-5 Admittance spectroscopy of a CIGS thin film solar cell.

By recording the frequency and temperature of the steps in capacitance, one can determine the activation energy, E_a of the defect, which gives information about the energy depth of the feature that causes the defect according to Eq (2-5). From Eq (2-5), we could get

$$E_a = kT \cdot \ln \frac{2\xi_o T^2}{\omega} \tag{2-8}$$

and then,

$$\ln(\frac{\omega}{T^2}) = -\frac{E_a}{k} \cdot \frac{1}{T} + \ln(2\xi_o) \tag{2-9}$$

The plot of $\ln(\omega/T^2)$ versus *1/T* using Eq (2-9) is usually called the Arrhenius plot. In this curve, we plot inflection frequency ω_o as a function of inverse temperature. Each plotting of ω_o gives information about the corresponding defect peak. Thus from the slope and intercept of equation (2-9), we can get the information of activation energy E_a and pre-emission factor ξ_o. One typical Arrhenius plot of a CIGS solar cell is shown in Fig. 2-6.

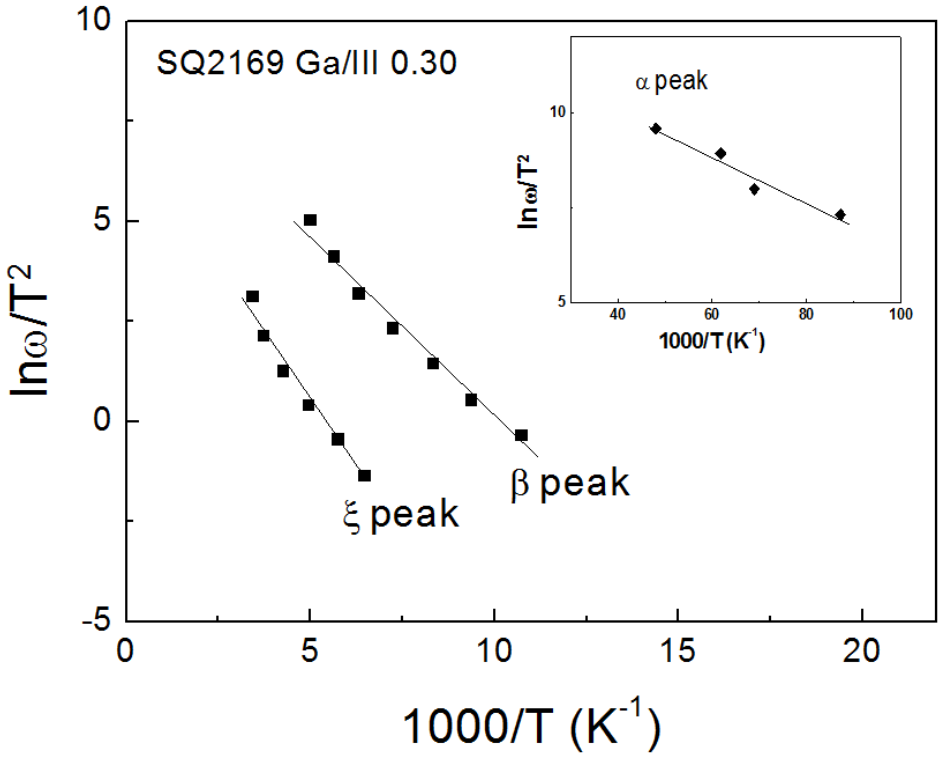

Fig. 2-6 Arrhenius plot of a CIGS thin film solar cell.

2.2.3 Density of defect

As described previously, by using Eq (2-7), the distribution of defect density with energy scale could be obtained. Fig. 2-7 shows a typical defect spectrum of CIGS thin film solar cell with Ga/III ratio of 0.30.

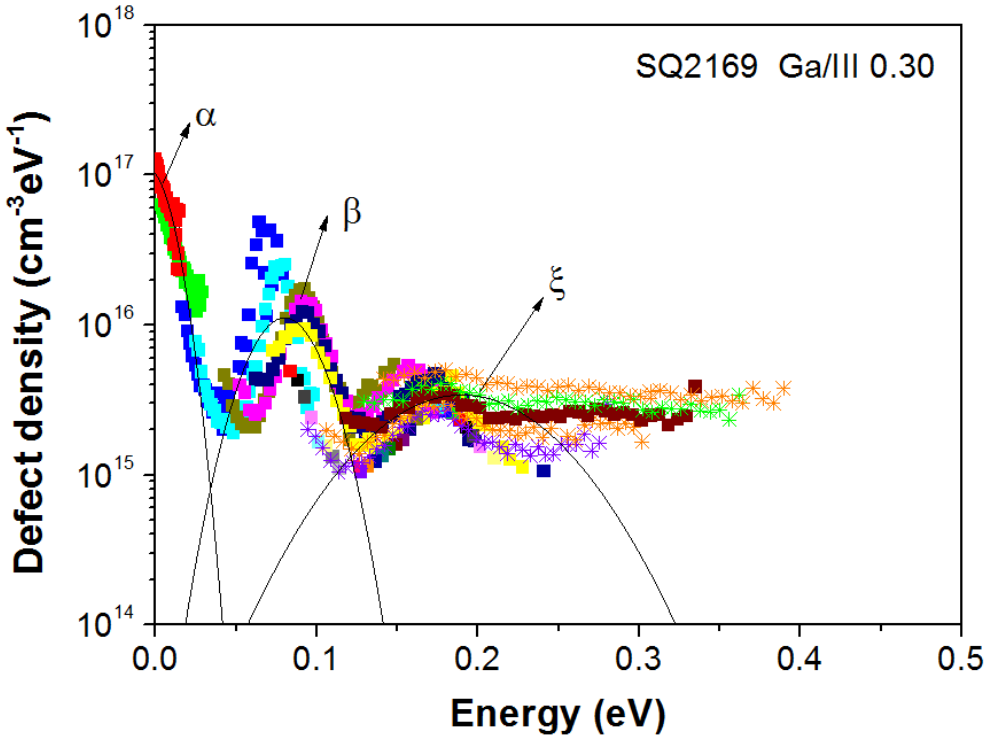

Fig. 2-7 Typical defect spectrum of CIGS thin film solar cell.

In Fig. 2-7, three peaks could be distinguished from the defect spectrum which are named as α, β and ζ which correspond to the three peaks detected from the Admittance spectroscopy as Fig. 2-5 showed. Each peak is associated with a particular defect that is present inside the band gap of CIGS material as well as at hetero-interface. These peaks are usually considered as shallow-level defects since the distance between the defect levels and the valence band edge are small (10 meV-300 meV) [2-11]. The densities of these trap levels are obtained by integrating over energy using a Gaussian approximation. Peak α observed could be considered as shallow acceptor level and attributed as V_{Cu} according to theoretical and experimental observation [2-12, 13]. Peak β is attributed to the defect level at the CdS film or the CdS/CIGS interface [2-14]. Finally for peak ζ, the V_{Cu}-V_{Se} complex defect is considered as a probable candidate for the generation of this peak in CIGS solar cell [2-13].

2.3 Results and discussion

2.3.1 Density of shallow defects versus Ga/III ratio

Fig. 2-8 shows the relationship between the density of the three shallow defects (α, β and ζ) and Ga/III ratio. It is seen from the figure that, only slight changes are observed for all three defects as a function of Ga/III ratio in the absorber layer. Moreover, no clear correlation was found between open circuit voltage, V_{oc} of several CIGS solar cells and defect density [2-15]. While, saturation of V_{oc} is considered as one of the main reasons for the degradation of performances in high Ga-content solar cell, our investigation for the defects suggest that the shallow defects might not play as active recombination centers which are responsible for voltage loss in CIGS solar cell.

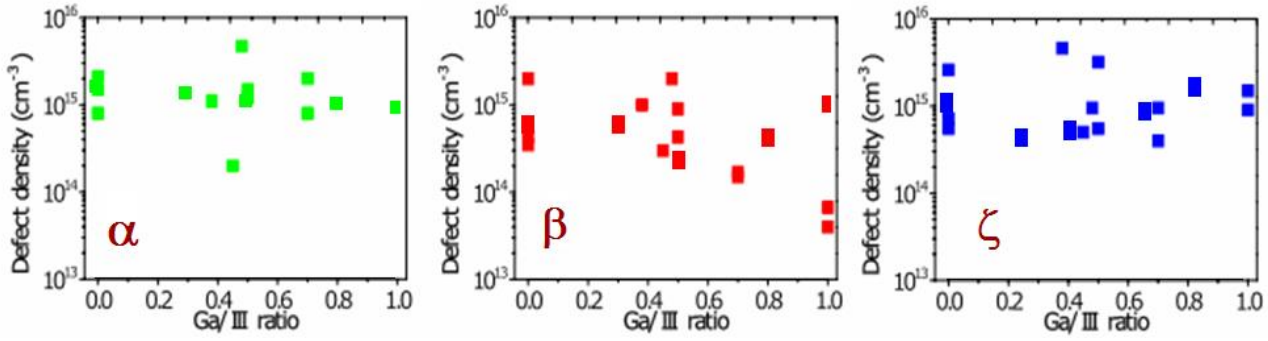

Fig. 2-8 The relationship between the density of shallow defects and Ga/III ratio [2-15].

2.3.2 Capture lifetime of shallow defects versus Ga/III ratio

As we have shown that the emission factor ξ_o is related with the capture cross section for holes σ_p represents of defect. We rewrite ξ_o as follows,

$$\xi_0 = (\sigma_p \upsilon_{th} N_V) / T^2 \tag{2-10}$$

Then, the carrier life time, τ, could be calculated as,

$$\tau = \frac{1}{\sigma_p \upsilon_{th} N_t} \tag{2-11}$$

where N_t is the defect density of each defect. Then the carrier lifetime was calculated for different samples

and the results were shown in Table 2-1. Most of the carrier lifetimes were found in the order of μs, this large carrier life time usually suggests these defects, may not so effective to act as trapping or recombination centers. Thus, shallow defects may not play important role to influence the efficiency of CIGS as Ga/III ratio increases. Thus we will focus on study of deeper level defects which are near mid-gap energy.

Table 2-1. Carrier life time (s) of shallow defects for CIGS of various Ga content

Ga/III	0.30	0.45	0.50	0.65	0.80
τ_β	2.4×10^{-5}	1.7×10^{-4}	5.4×10^{-7}	-	1.0×10^{-5}
τ_ζ	4.7×10^{-4}	2.0×10^{-6}	1.7×10^{-6}	8.5×10^{-7}	9.8×10^{-7}

2.4 Summary

In CIGS thin films, shallow defects which are near band edge seem not to play as active recombination centers which are responsible for efficiency loss in CIGS solar cell as Ga/III ratio increases.

Reference

[2-1] J. D. Jackson, *Classical Electrodynamics*, Wiley, New York, 1975, p. 311.

[2-2] S. M. Sze and Kwok K. Ng, *Physics of semiconductor devices*, John Wiley & Sons, Hoboken, 2006.

[2-3] K.W. Boer, *Survey of Semiconductor Physics*, Van Nostrand Reinhold, New York, 1990, p.1135.

[2-4] A. K. Jonscher, *Dielectric Relaxation in Solids*, Chelsea Dielectrics Press, London, 1983, p. 158.

[2-5] Y. Zohta, Frequency dependence of C and $\Delta V/\Delta(C^{-2})$ of Schottky barriers containing deep impurities, Solid State Electron, **16** (1973) 1029.

[2-6] D. Mencaraglia, S. Ould Saad, and Z. Djebbour. Admittance spectroscopy for non-crystalline thin film devices characterization: comparison of Cu(In, Ga)Se_2 and a-Si: H cases. Thin solid films **431** (2003) 135.

[2-7] A. Jasenek, U. Rau, V. Nadenau, and H. W. Schock. Electronic properties of $CuGaSe_2$-based heterojunction solar cells. Part II. Defect spectroscopy, J. Appl. Phys., **87** (2000) 594.

[2-8] R. Herberholz, M. Igalson, and H. W. Schock. Distinction between bulk and interface states in $CuInSe_2$/CdS/ZnO by space charge spectroscopy, J. Appl. Phys. **83** (1998) 318.

[2-9] D. L. Losee, Admittance spectroscopy of impurity levels in Schottky barriers, J. Appl. Phys. **46** (1975) 2204.

[2-11] M. Burgelman, F. Engelhardt, J. F. Guillemoles, R. Herberholz, M. Igalson, R. Klenk, M. Lampert, T. Meyer, V. Nadenau, A. Niemegeers, J. Parisi, U. Rau, H. W. Schock, M. Schmitt, O. Seifert, T. Walter

and S. Zott, Defects in Cu(In, Ga) Se_2 Semiconductors and their Role in the Device Performance of Thin-film Solar Cells, Prog. Photovolt: Res. Appl., **5** (1997) 121-130.

[2-12] S. B. Zhang, S. H. Wei, A. Zunger, and H. Katayama-Yoshida, Defect physics of the $CuInSe_2$ chalcopyrite semiconductor. Phys. Rev B, **57** (1998) 9642.

[2-13] T. Sakurai, N. Ishida, S. Ishizuka, M. M. Islam, A. Kasai, K. Matsubara, K. Sakurai, A. Yamada, K. Akimoto, S. Niki, Effects of annealing under various atmospheres on electrical properties of $Cu(In,Ga)Se_2$ films and $CdS/Cu(In,Ga)Se_2$ heterostructures, Thin Solid Films **516** (2008) 7036.

[2-14] H. W. Schock and U. Rau, The role of structural properties and defects for the performance of Cu-chalcopyrite-based thin-film solar cells, Physica B **308** (2001) 1081.

[2-15] M. M. Islam, *Growth and Defect Characterization of $Cu(In_{1-x}Ga_x)Se_2$ Thin Film and Fabrication of Solar Cell*, PhD thesis, University of Tsukuba, 2010.

Chapter 3 Deep-level Defect Characterization by Transient Photocapacitance Spectroscopy

A large number of studies on the properties of defects in CIGS, such as the density of states and effects on device performance, have been carried out over the past decade [3-1~8]. Admittance spectroscopy and deep-level transient spectroscopy (DLTS) are most commonly used two techniques to study of majority carrier traps, which are defects generally lying in the lower half of the gap [3-9]. However, characterization of deep-level defects which are near the midgap and upper half of the gap is especially difficult, since deep levels cannot follow AC electrical signals owing to their extremely large time constants [3-10]. Among the few available characterization techniques, sub-bandgap optical absorption methods are useful for the detection of deep defects. In particular, transient photocapacitance (TPC) spectroscopy is a powerful tool for the analysis of deep levels in a photoabsorber layer because of the very low detection limit [3-11, 12]. In this chapter, the deep-level defects in CIGS thin films will be investigated by transient photocapacitance spectroscopy.

3.1 Basic principle of Transient photocapacitance spectroscopy (TPC)

The principle and implementation of the TPC method is similar to the familiar DLTS technique [3-13]. In order to explain DLTS, we must first consider the more basic problem of capacitance transients. This technique is used to obtain information about an impurity level in the depletion region of a Schottky barrier or p-n junction by observing the capacitance transient associated with the return to thermal equilibrium of the occupation of the level following an initial non-equilibrium condition. For simplicity, we will describe the situation in p-type material in an asymmetric n^+p diode. Fig. 3-1 is a schematic summary of the emission and capture processes which characterize a particular trap. The capture and thermal emission rates for the minority carriers (electrons in the example) are c_1 and e_1, respectively. The capture and thermal emission rates for majority carriers (holes) are c_2 and e_2, respectively. In the quiescent state of the system, the diode is reverse biased and the observable traps are within the depletion region. Thus, the capture rates are zero and the occupation of the level is determined by the thermal emission rates e_1 and e_2. As indicated in Fig. 3-1, the steady-state electron occupation of a level is

$$\bar{n}_1 = [e_2/(e_1 + e_2)]N \tag{3-1}$$

where N is the concentration of the trap. We define an electron (minority-carrier) trap as one which tends to be empty ($\bar{n}_1 = 0$) of electrons, and thus capable of capturing them. Likewise, a hole (majority-carrier) trap is one which tends to be full ($\bar{n}_1 = N$) of electrons, and thus capable of having a trapped electron recombine with a hole or capture a hole. Then, according to Eq. (3-1), an electron trap has to have $e_1 >> e_2$, and a hole trap $e_2 >> e_1$. This is indicated by the heavy and light arrows at the bottom of Fig. 3-1. The emission rates are proportional to a Boltzmann factor, and thus depend exponentially on the energy difference between the trap level and

conduction band (electron emission) and the trap level and the valence band (hole emission). Because of this, electron traps tend to be in the upper half of the gap and hole traps in the lower half. As shown in Fig. 3-1, a capacitance change is caused by using a bias pulse to introduce carriers, and thus changes the electron occupation of a trap from the steady-state value in Eq (3-1). As this population returns to equilibrium, the capacitance returns to its quiescent value. For the simple linear rate equations illustrated in Fig. 3-1, the transient is an exponential function of time with a rate constant equal to $e_1+ e_2$. One of these rates usually dominates, thus the transient rate for a majority-carrier trap is e_2 and for a minority-carrier trap is e_1. The sign of the capacitance change depends on whether the electron occupation of the trap had been increased or decreased by the pulse. An increase in trapped minority carriers causes an increase in the junction capacitance. As indicated in the bottom of Fig. 3-1, the capacitance transient due to a minority-carrier trap is always positive and is induced only by injected minority carriers, whereas the transient due to a majority-carrier trap is always negative and is induced only by majority carriers.

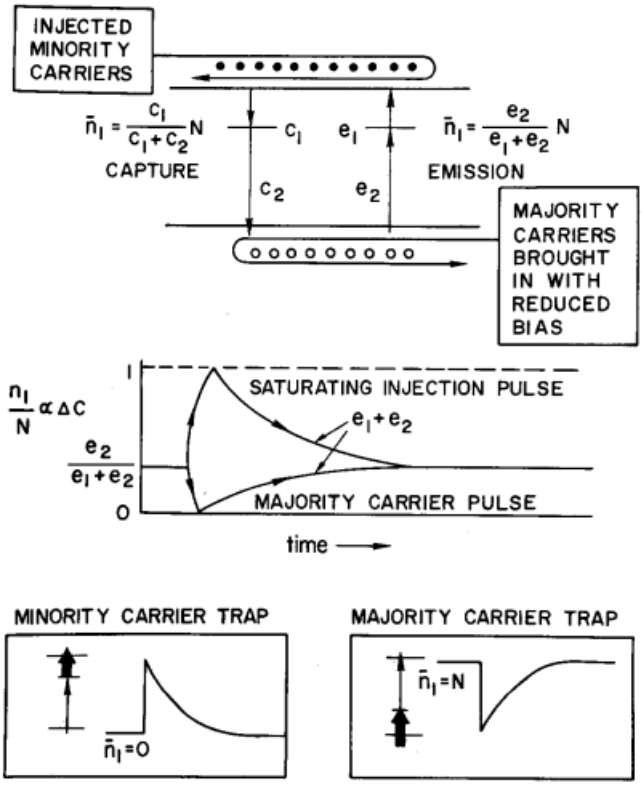

Fig. 3-1 Schematic summary of the emission and capture processes which describe a particular trap in p-type material and give rise to the characteristic capacitance transient of that trap [3-13].

Now we consider a majority-carrier pulse which momentarily reduces the diode bias and introduces only majority carriers into the region of observation, the pulse sequence is shown in Fig. 3-2. The process is illustrated as follows:

I. An n+p junction is under quiescent reverse D.C. bias and the charge is in equilibrium;

II. Then, a "filling pulse" forward voltage is biased on the junction, during this voltage, the trap will capture electrons from the conduction band. A sudden decrease of junction capacitance would occur.

III. Finally, the reverse bias is restored and the electrons above the Fermi energy E_F in the trap will slowly released to the conduction band due to thermal excitation. A slow increase of junction capacitance would occur.

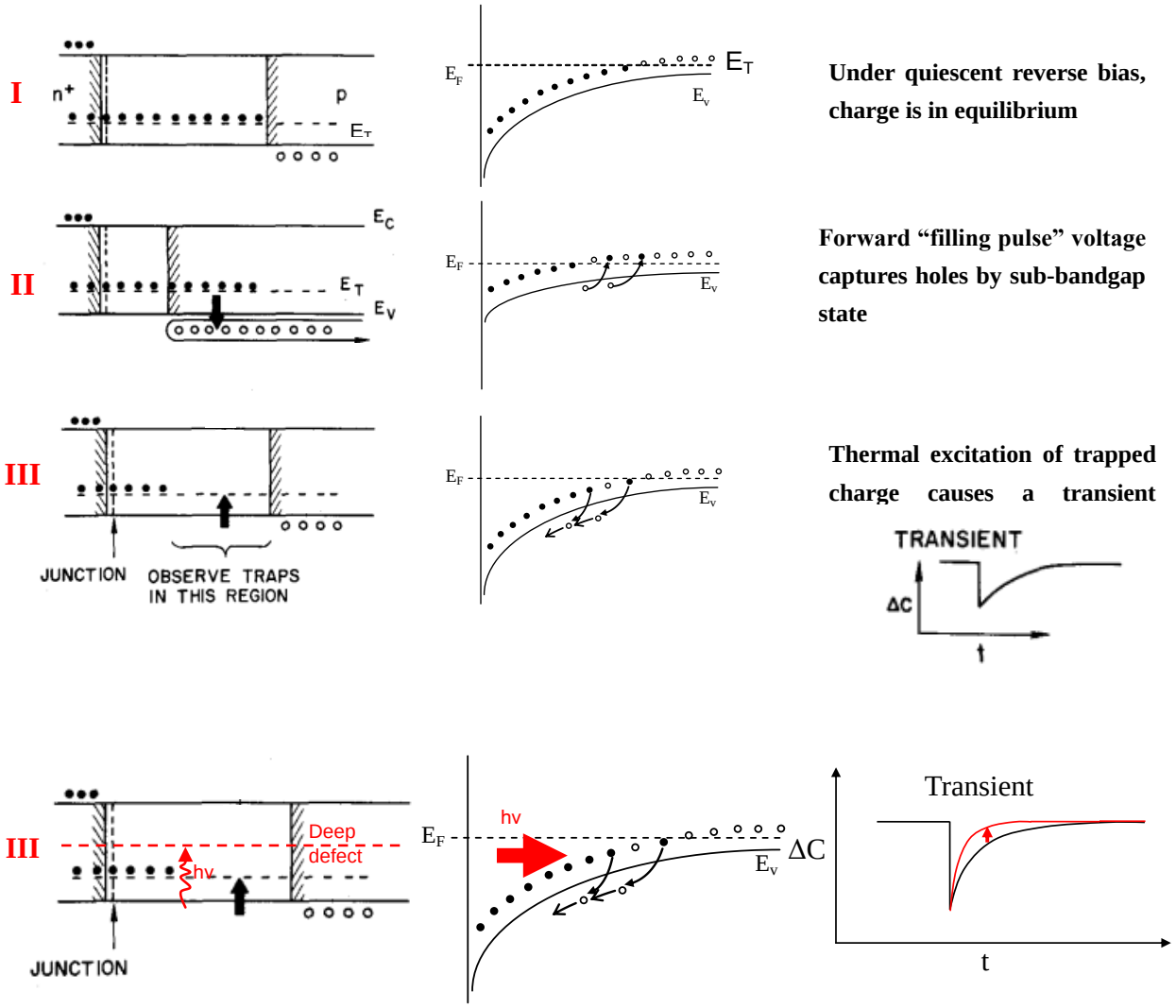

Fig. 3-2 Majority-carrier pulse sequence and optically induced response of deep-level defect in addition to the thermal response of the shallow-level defect

Now, in process III, an additional sub-bandgap light is used to excite a deep-level defect which locates far away from the valence band, then, an enhanced junction capacitance due to the occupation of the deep-level defect would be observed as Fig. 3-2 (bottom) shows. After subtracting the thermal effect due to the shallow trap to the capacitance transient, the contribution of optical effect due to deep defect could be obtained, which is the basic idea of TPC.

3.2 Experimental

3.2.1 Experimental Setup

The experimental setup for TPC measurements is shown in Fig. 3-4. The measurements are performed with a halogen lamp as the excitation source, using a monochromator-based setup. The intensity of the light source was calibrated by a photodiode (PM100D, THORLABS, Inc.) and the output spectrum of the halogen lamp is shown in Fig. 3-5. Higher order wavelengths were filtered by long pass filters. The spot size of the light beam is about 1.76 mm^2. The samples for the measurements are small circles with diameter of 1 mm and cell structures, which were patterned by photolithography process. CIGS solar cell

samples are fixed in the cryostat chamber which is the same as the one used in the admittance spectroscopy measurements. The samples' temperature could be maintained from 60 K to 300 K. Prior to the measurements, the samples are allowed to relax under dark conditions at room temperature for a sufficiently long time.

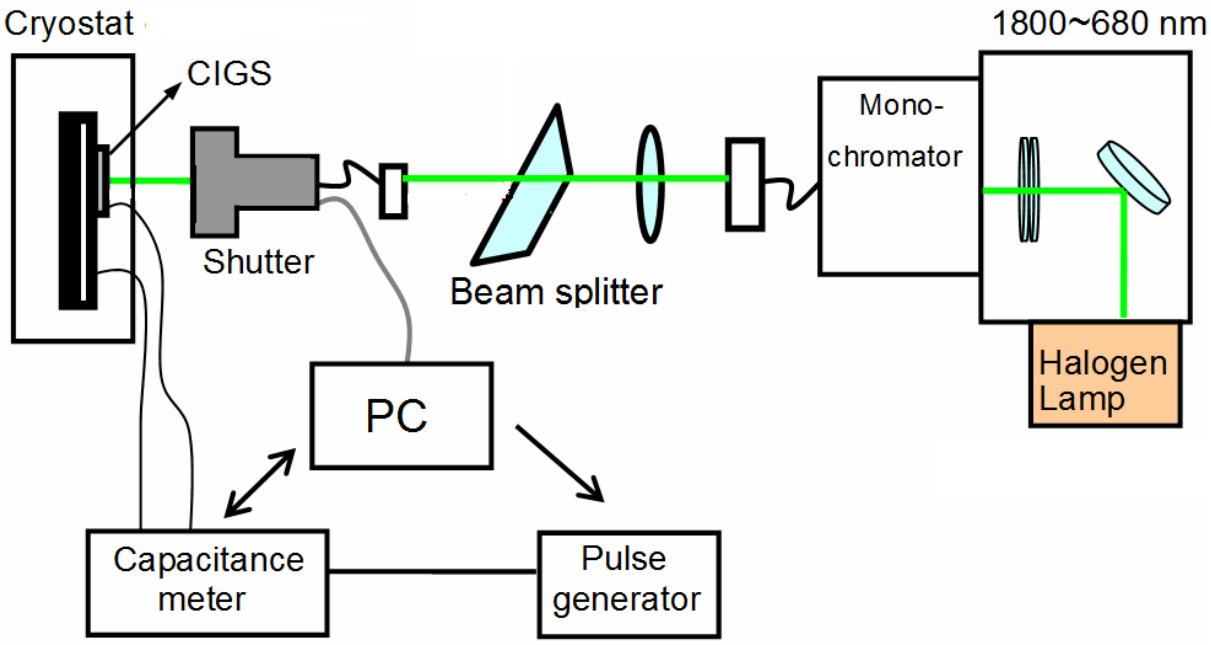

Fig. 3-3 Experimental setup for TPC measurements

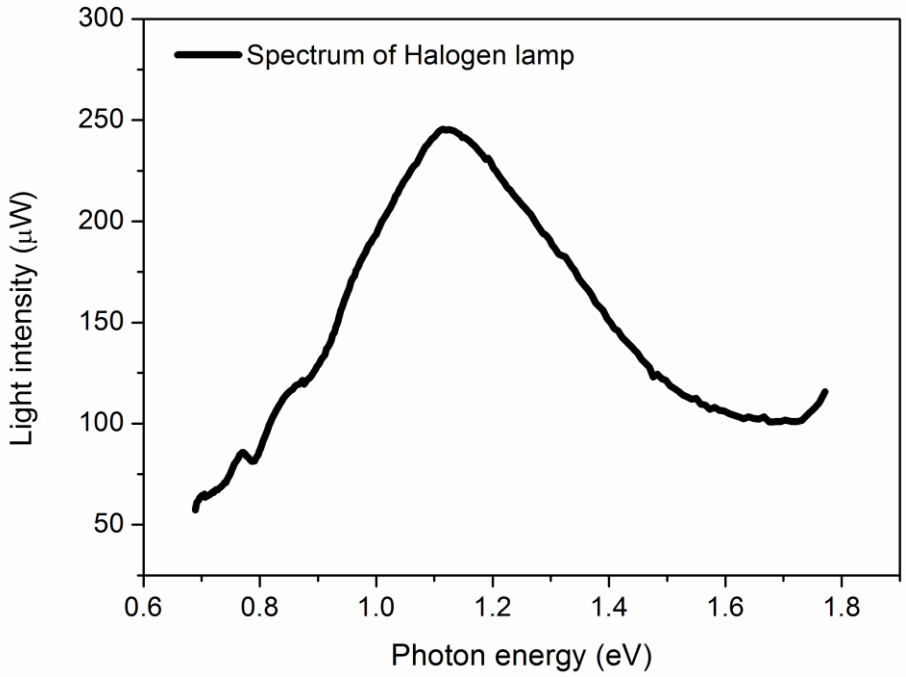

Fig. 3-4 Spectrum of halogen lamp in the range of 680 nm-1800 nm.

3.2.2 Time sequence for TPC measurements

TPC measurements are carried out with a fill pulse bias of 0 V and a quiescent bias of 0.5 V (reverse bias) by using a Boonton 72B capacitance meter (shown in Fig. 3-3, ac frequency: 1 MHz). The pulse width and period were fixed at 50 ms and 1 s, respectively. The timing chart for the measurements is shown in Fig. 3-5. The transient response, which arises after the pulse, is integrated over a fixed time window (integration time=0.75 s) by using an analog-to-digital converter with 24-bit resolution. The rate window was fixed at 2 s^{-1}.

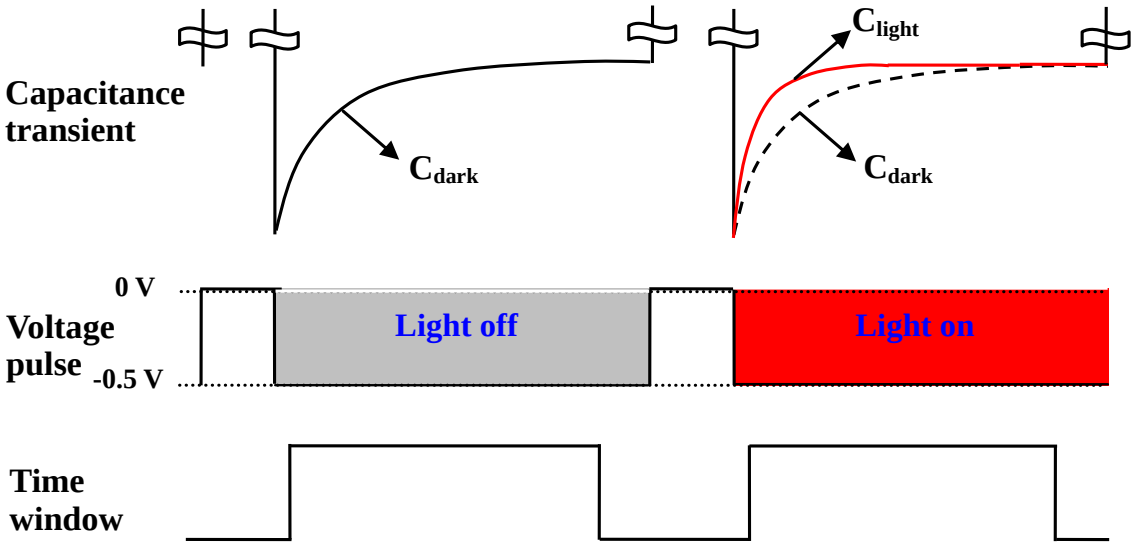

Fig. 3-5 Timing sequence for the TPC measurement. The voltage pulse is applied on top of an applied DC bias.

3.2.3 Definition of TPC signal S_{TPC} and S^*_{TPC}

The TPC signal (S_{TPC}) is obtained by extracting the difference from the capacitance transient signals without (C_{Dark}) and with (C_{Light}) light by integrating the signals over a time window (t) as Fig. 3-5 shows. Thus, the resultant difference signal contained no thermal component. After normalizing the difference to the photon flux, the TPC spectrum could be obtained. The TPC signal is defined as

$$S_{TPC} = \frac{\int C_{light}dt - \int C_{dark}dt}{Photon\ \ flux} \equiv \frac{\Delta C}{Photon\ \ flux}, \tag{3-2}$$

The definition of S_{TPC} was obtained from [3-9]. Here, we define $\int C_{light}dt - \int C_{dark}dt$ as ΔC for convenience. ΔC was always kept linear with incident photon flux so that the TPC signal had no relationship with the incident light spectrum including the shape and intensity.

The capacitance change dC' of the abrupt p-n junction when sub-bandgap light was induced under periodical reverse bias was related to the density of deep defects as expressed by [3-14]

$$dC'/C' = -N_T(x)\cdot x\cdot dx\cdot \delta f_T/(W^2\cdot N_A) \tag{3-3}$$

where C' is the quiescent capacitance at an applied bias, N_A is the net majority carrier concentration, $N_T(x)$ is the defect density at a distance of x from the metallurgical junction, δf_T is the occupancy ratio change of electrons at the defect level with an applied bias, and W is the width of the depletion region at an applied bias. By integrating the entire depletion region and considering δf_T of 1 after one period, we can determine the defect density

$$N_T = 2(\Delta C'/C') \cdot N_A \tag{3-4}$$

where $\Delta C'$ is the total capacitance change caused by light irradiation.

Therefore, to make the comparison of sub-bandgap TPC signals for samples with different Ga contents possible, an extra handling of the signals was carried out by defining a new TPC signal S^*_{TPC} as shown by

$$S^*_{TPC} = \frac{(\Delta C/C) \cdot N_A}{Photon\ flux} = S_{TPC} \cdot \frac{N_A}{C} \tag{3-5}$$

where ΔC and S_{TPC} are defined in Eq. (3-2), C is the quiescent capacitance at an applied bias, and N_A is the net majority carrier concentration deduced from the capacitance-voltage (C-V) measurements. The new signal eliminates the effects of the carrier concentration and width of the depletion region for different samples as in the case of DLTS experiments, where $(2\Delta C/C)N_A$ was simply used to quantitatively estimate the trap concentration [3-13]. Thus, S^*_{TPC} enables a relatively quantitative comparison of densities of deep defects while assuming all samples as n^+p step junctions.

3.2.4 CIGS solar cells for TPC measurements

Polycrystalline CIGS thin films were grown on Mo-coated soda-lime glass substrates by a three-stage process using a molecular beam epitaxy (MBE) system. The Ga content (x) was controlled to be 0.30-0.80, and the copper content of the CIGS films was roughly fixed at around Cu/(In+Ga)=0.90. The detailed deposition conditions for the CIGS films have been described in Chapter 1. The device parameters of CIGS thin-film solar cells used in this study are listed in Table 3-1.

Table 3-1. CIGS device parameters used in this study measured under AM1.5 illumination at 25 °C.

Ga/III	E_g (eV)	J_{sc} (mA/cm^2)	V_{oc} (V)	Eff. (%)
0.30	1.18	29.73	0.68	15.88
0.40	1.24	27.88	0.73	15.67
0.45	1.28	29.53	0.66	14.70
0.50	1.31	27.52	0.71	14.36
0.52	1.32	26.47	0.70	13.56
0.62	1.39	24.39	0.71	12.67
0.76	1.49	22.35	0.74	11.15
0.80	1.52	20.29	0.73	10.14

3.3 Results and discussion

Fig. 3-6 shows the TPC spectra for CIGS with different Ga contents, which were measured at 60 K since at such a low temperature, the thermal emission effect of deep defects could be neglected, compared with that of the optical transition process. All the spectra were normalized to the maximum values of the signals above the bandgap energy to obtain a maximum amplitude of 1. This is reasonable when assuming a common high density of states in the valence and conduction bands for all samples since the above bandgap TPC signal is proportional to the density of states in the valence and conduction bands. All the TPC spectra shown for each sample can be divided into two regions, namely, the interband and sub-bandgap regions.

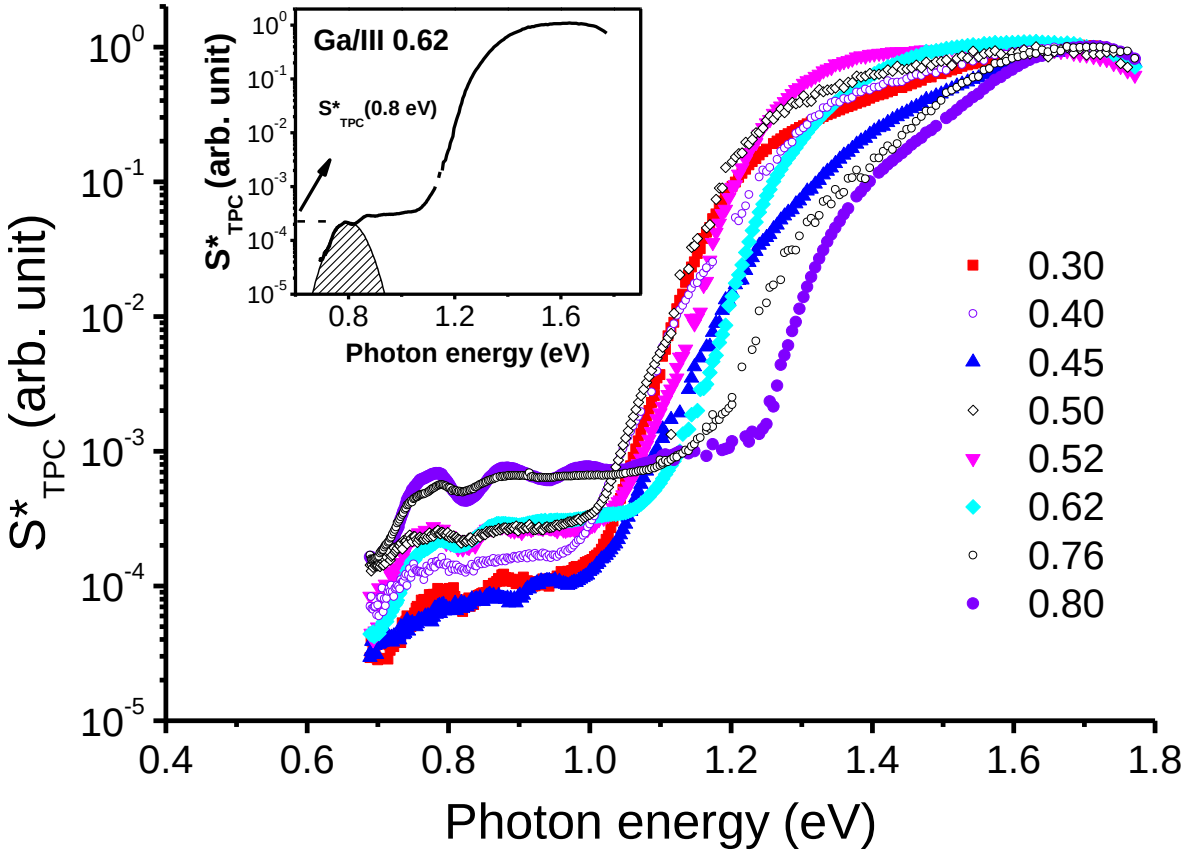

Fig. 3-6. TPC spectra (S^*_{TPC}) of CIGS samples with various Ga contents from 0.30 to 0.80 measured at 60 K. The inset shows a fitting example to obtain the S^*_{TPC} signal at a deep defect level for a CIGS sample with a Ga content of 0.62.

For the interband region, the signal is contributed by the optical transition between the valence and conduction bands. In Fig. 3-6, a sharp increase in the intensity of the TPC signal with an increase in photon energy can be seen in all samples; the increase is attributed to the large cross section of the direct interband transition [3-6]. Moreover, an increase in the threshold energy of the interband absorption with the Ga concentration in CIGS can also be seen, which is due to the variation in bandgap. In Ref. [3-15], the bandgap energy was estimated from the TPC spectra by using the points where the band edge started to deviate from the exponential relationship with photon energy. Although this was not a precise method compared with the method used to obtain the theoretically predicted value (basically smaller than the theoretical values for all samples) [3-16], it could still be used to estimate the relative relationship between the bandgaps of different samples and an increase in bandgap energy with increasing Ga content could still be seen in Fig. 3-6.

For the sub-bandgap region, the signal is contributed by the optical transition below the bandgap, such as that between gap states and the valence or conduction band. The wavy profile of the sub-bandgap spectrum that could be seen in almost all samples was thought to be due to spectrum interference [3-6]. All the sub-bandgap spectra could be well fitted by a Gaussian-shaped defect band, the center of which is around 0.8 eV. The spectrum broadening was thought to be caused by the strong electron–phonon interaction due to the deep defect that could be understood easily when considering a coordinate configuration model for the defect structure [3-6]. An example is shown in the inset of Fig. 3-6 for the CIGS sample with a Ga/III ratio of 0.62. The estimated S^*_{TPC} (0.8 *eV*) was thought to be proportional to the density of deep defects. A similar defect level at around 0.8 eV (the defect position was designated at 0.8 eV, although there was a deviation of about 0.05 eV from this position for different samples) above the valence band was estimated for all samples, since the positive signal change indicates that the signal actually corresponds to the transition of electrons from the valence band to the empty defect levels in the p-type CIGS samples. Thus, a common deep defect, the level of which is constant with respect to the valence band maximum (VBM) for samples with different Ga contents, was confirmed. A few structural models have been reviewed. Those models may be related to the 0.8 eV defect, such as the V_{Se} -V_{Cu} divacancy defect model and $(In, Ga)_{Cu}$ antisite defect model in Ref. [3-1]; however, the origin of this defect is still not definite and needs further investigation. Possible origins other than the two defect models will be discussed in Chapter 7.

Then, by extracting the intensity of S^*_{TPC} at an energy level of 0.8 eV from Fig. 3-6, the dependence of the signal intensity, which reflects the defect density, on the Ga content was obtained as shown in Fig. 3-7. It indicates that the defect density generally increases with increasing Ga/III ratio. Since the deep defect may act as an effective recombination center that deteriorates the open-circuit voltage and thus reduces the efficiency, decreasing the concentration of 0.8 eV defects is a promising method of improving cell efficiency, especially for solar cells with high Ga content.

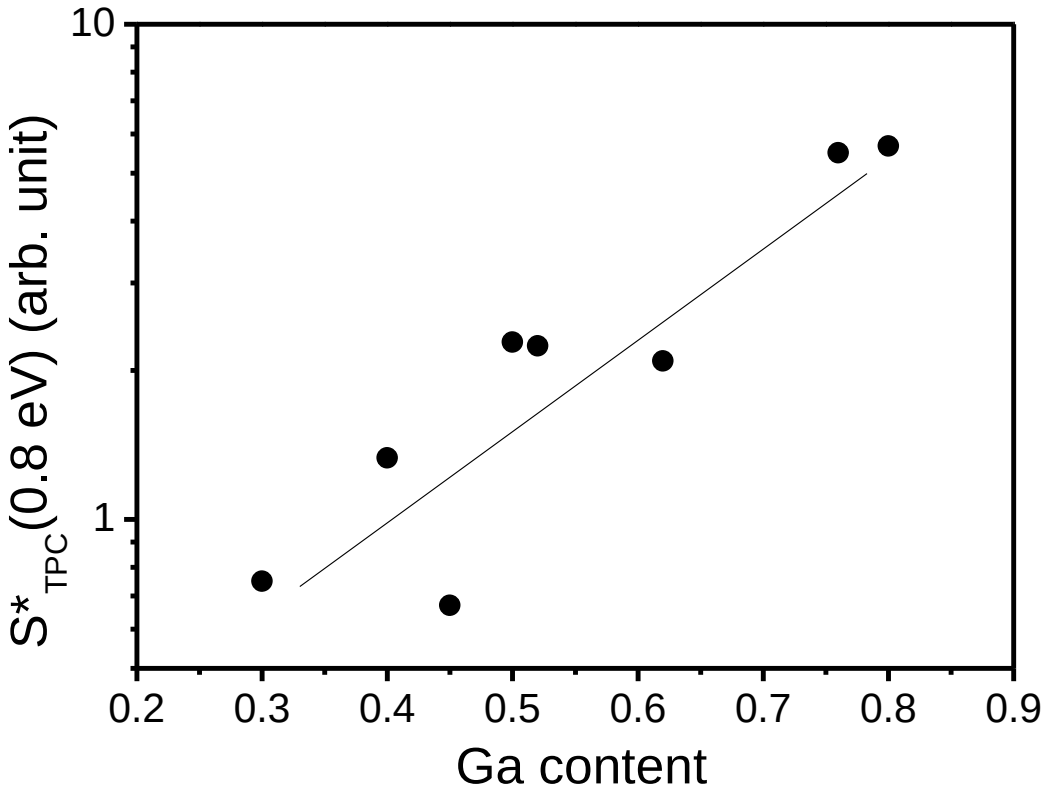

Fig. 3-7. Dependence of $S^*_{TPC}(0.8\ eV)$, which reflects the defect density N_t(0.8 eV), on the Ga content.

3.4 Summary

The deep defects in Cu(In,Ga)Se_2 were characterized by transient photocapacitance spectroscopy. A defect level at around 0.8 eV with respect to the valence band maximum (VBM), which is independent of Ga content, was observed in all samples. A method for a relatively quantitative comparison of deep defect densities was proposed and the defect density seemed to increase with increasing Ga/III ratio. Since the 0.8 eV defect may be responsible for the low device performance, especially for CIGS samples with high Ga content, it is necessary to decrease the density of defects to improve cell efficiency.

Reference

[3-1] S. Siebentritt, M. Igalson, C. Persson, and S. Lany, The electronic structure of chalcopyrites—bands, point defects and grain boundaries, Prog. Photovoltaics **18** (2010) 390.

[3-2] J. T. Heath, J. D. Cohen, W. N. Shafarman, D. X. Liao, and A. A. Rockett, Effect of Ga content on defect states in $CuIn_{1-x}Ga_xSe_2$ photovoltaic devices, Appl. Phys. Lett. **80** (2002) 4540.

[3-3] M. Turcu and U. Rau, Fermi level pinning at CdS/Cu(In,Ga)$(Se,S)_2$ interfaces: effect of chalcopyrite alloy composition, J. Phys. Chem. Solids **64** (2003) 1591.

[3-4] M. Igalson and C. Platzer-Bjorkman, The influence of buffer layer on the transient behavior of thin film chalcopyrite devices, Sol. Energy Mater. Sol. Cells **84** (2004) 93.

[3-5] V. Aubin, L. Binet, and J. F. Guillemoles, Electron spin resonance studies of Cu(In,Ga)Se2 thin films, Thin Solid Films **431** (2003) 167.

[3-6] T. Sakurai, H. Uehigashi, M. M. Islam, T. Miyazaki, S. Ishizuka, K.Sakurai, A. Yamada, K. Matsubara, S. Niki, and K. Akimoto, Temperature dependence of photocapacitance spectrum of CIGS thin-film solar cell, Thin Solid Films **517** (2009) 2403.

[3-7] S. Siebentritt and U. Rau, *Wide-Gap Chalcopyrites*, Springer, Heidelberg, 2006, p. 113-156.

[3-8] M. Gloeckler, J. R. Sites, and W. K. Metzger, Grain-boundary recombination in Cu(In,Ga)Se_2 solar cells, J. Appl. Phys. **98** (2005) 113704.

[3-9] S. Siebentritt and U. Rau, *Wide-Gap Chalcopyrites*, Springer, Heidelberg, 2006, p. 70-90.

[3-10] J. Barbolla, S. Duenas, and L. Bailon, Admittance spectroscopy in junctions, Solid-State Electron. **35** (1992) 285.

[3-11] J. D. Cohen, T. Unold, A. V. Gelatos, and C. M. Fortmann, Deep defect structure and carrier dynamics in amorphous silicon and silicon-germanium alloys determined by transient photocapacitance methods, J. Non-Cryst. Solids **141** (1992) 142.

[3-12] P. M. Mooney, G. A. Northrop, T. N. Morgan, and H. G. Grimmeiss, Evidence for large lattice relaxation at the DX center in Si-doped $Al_xGa_{1-x}As$, Phys. Rev. B **37** (1988) 8298.

[3-13] D. V. Lang, Deep‐level transient spectroscopy: A new method to characterize traps in semiconductors, J. Appl. Phys. **45** (1974) 3023.

[3-14] M. Stavola, Identification of Defects in Semiconductors, Academic press, San Diego, 1999, chapter 2.

[3-15] M. D. Westley, C. W. Warren, O. Gunawan, T. Gokmen, D. B. Mitzi, and J. D. Cohen, Electronically active defects in the $Cu_2ZnSn(Se,S)_4$ alloys as revealed by transient photocapacitance spectroscopy, Appl. Phys. Lett. **101** (2012) 142106.

[3-16] M. Turcu, I. M. Kotschau, and U. Rau, Band alignments in the $Cu(In,Ga)(S,Se)_2$ alloy system determined from deep-level defect energies, Appl. Phys. A **73** (2001) 769.

Chapter 4 Deep-level Defect Characterization by Two-wavelength Excitation Photocapacitance Spectroscopy

In Chapter 3, a deep-level defect at around 0.8 eV from the valence band edge in CIGS films was determined by the TPC. As the Ga content increases this defect approaches the midgap position, this defect potentially evolving into an effective recombination center since deep-level defects usually possess long carrier emission time and large capture cross sections. However, whether this defect really acts as a recombination center needs more investigation. In this chapter, a two-wavelength excitation photocapacitance method was utilized to investigate the defect properties and the optical process for photo-excited electrons related to the 0.8 eV deep-level defect from the valence band and investigate whether this defect acts as a recombination.

4.1 Baisc principle

To identify the role of the 0.8 eV defect, a two-wavelength light irradiation method with a tunable monochromatic probe light and a laser light (with a photon energy of 0.8 eV) was introduced. The principles of this method involving the 0.8 eV defect are illustrated in Fig. 4-1.

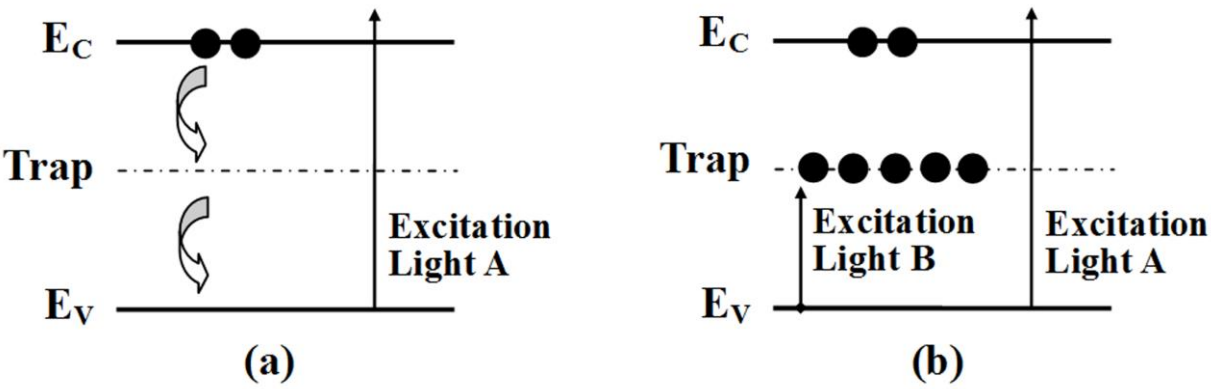

Fig. 4-1. Schematic diagram demonstrating the principle of the two-wavelength method involving the 0.8 eV defect. Excitation light A: monochromatic probe light; Excitation light B: 0.8 eV laser light.

Fig. 4-1(a) shows the electron distribution during a normal photo-capacitance measurement using only a monochromatic probe light called excitation light A (denoted as normal conditions), and Fig. 4-1(b) shows the electron distribution when the defect is saturated by carriers using 0.8 eV laser irradiation called excitation light B (denoted as saturated conditions). The TPC signal represents the net minority carrier's concentration (here is electron) left in the depletion region [4-1]. Here we focused on the minority carrier (electron) concentration left in the conduction band (which would be defined as ΔI in the next paragraph) after the optical transitions and recombination processes which may include interband recombination and SHR recombination. When the laser light was on, the filling states' fraction (occupied by electrons) of the defect level was large, the capture probability of electrons in conduction band by the defect level was small,

and the main recombination process was the interband recombination. Thus there was only one recombination path to decrease the electrons' concentration in the conduction band. When the laser light was off, the filling states' fraction of the defect was small, which mean there were still many empty states, so the electrons in the conduction band could be more easily captured and recombine with the holes captured from the valence band. Thus there were two possible recombination paths to decrease the electrons' concentration in the conduction band. Therefore, by assuming that the interband recombination process was unchanged before and after the laser was turned on, it was possible to identify whether the center works as a recombination center or not. If the defect level acts as a recombination center, the carrier density, corresponding to the TPC signal, in the conduction band under saturated conditions should be larger than under normal conditions. On the contrary, if the defect level does not act as a recombination center, the carrier density at the conduction band under saturated conditions should be the same as under normal conditions.

To more precisely evaluate the difference in charge distribution in the conduction band between normal and saturated conditions, the R value defined below was examined using the following equations,

$$\Delta I_s = I_s(1.5\,\mathrm{eV}) - I_s(0.8\,\mathrm{eV}) \tag{4-1}$$

$$\Delta I_n = I_n(1.5\,\mathrm{eV}) - I_n(0.8\,\mathrm{eV}) \tag{4-2}$$

$$R = \Delta I_s / \Delta I_n \tag{4-3}$$

where I_s(1.5 eV) and I_s(0.8 eV) represent the signal intensity of the TPC measured at photon energies of 1.5 eV and 0.8 eV under saturated conditions, respectively. Similarly, I_n(1.5 eV) and I_n(0.8 eV) represent values measured under normal conditions. In our case, I_n(0.8 eV), which represents the signal intensity of the sub-bandgap transition, is negligible since it is two orders of magnitude lower than I_n(1.5 eV), which represents the signal intensity of the interband transition. A schematic illustration of I_s and I_n is shown in Fig. 4-2, in which the photon energies of 0.9 eV and 1.4 eV were selected as examples representing the sub-bandgap transition energy and the interband transition energy, respectively. When the 0.8 eV defect acts only as a trapping center, the R value should be 1, and when the defect acts as a recombination center, the R value should be greater than 1.

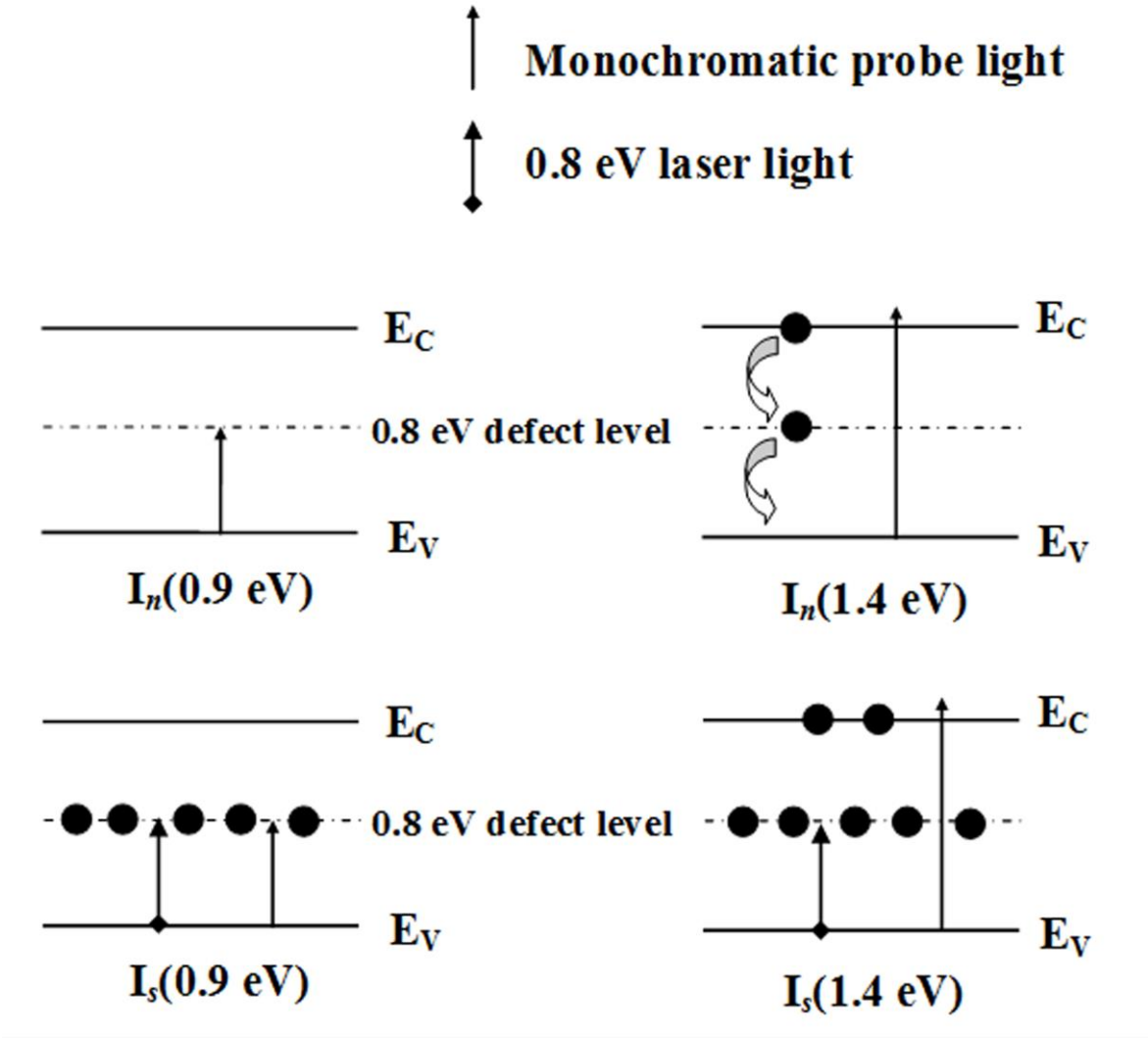

Fig. 4-2. Schematic illustration of I_n(0.9 eV) and I_n(1.4 eV) under normal conditions and I_s(0.9eV) and I_s(1.4eV) under saturated conditions. Two different types of arrows are shown in the top which represent the monochromatic probe light and 0.8 eV laser light, respectively.

4.2 Experimental

4.2.1 Experimental setup

Fig. 4-3 shows the experimental setup for the two-wavelength excitation photocapacitance measurements. The setup is very similar to the one for the TPC measurements except that a second laser light (Light source B) with a wavelength of 1.55 μm, corresponding to 0.8 eV, is introduced for irradiation on the CIGS solar cell samples besides the monochromator light (probe light) from the halogen lamp source (Light source A). The 0.8 eV laser beam corresponding to the defect level was irradiated simultaneously with the probe light using a collimator lens and a beam splitter. The two light sources were chopped synchronously to the excitation pulse using an electronic shutter. The measurements were carried out under two kinds of temperature condition, 140 K and RT which represents low temperature and high temperature. The other experimental details such as the timing sequence are the same as the TPC measurements which has been demonstrated in chapter 3.

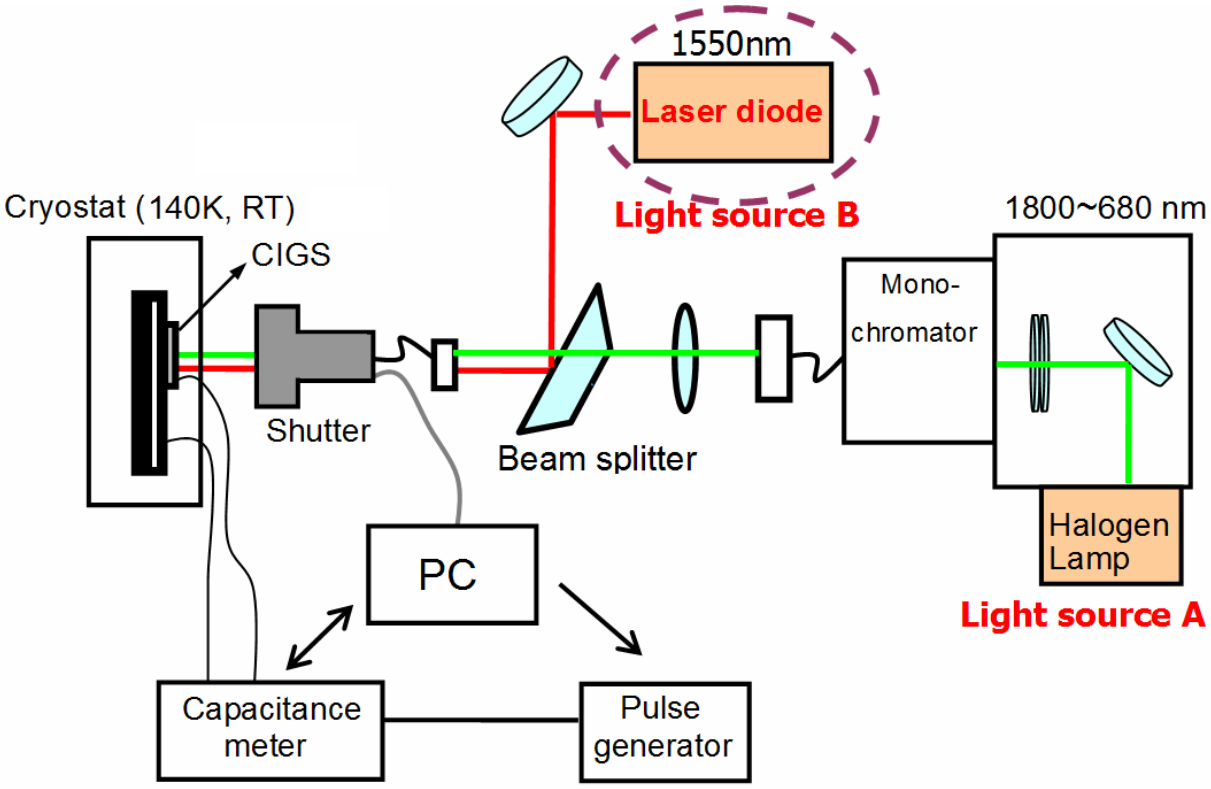

Fig. 4-3. Schematic diagram of the experimental setup for the two-wavelength excitation photocapacitance measurements

4.2.2 CIGS solar cells for measurements

Polycrystalline CIGS thin-films were grown on Mo-coated soda-lime glass substrates by a three-stage process using a molecular beam epitaxy (MBE) system. The Ga content x was controlled to be 0.45-1.0, and the copper content of the CIGS films was roughly fixed at approximately Cu/(In+Ga) = 0.9. The detailed deposition conditions for the CIGS films were described previously in Chapter 1. The device parameters of the CIGS thin-film solar cells used in this measurement are listed in Table 4-1.

Table 4-1. CIGS device parameters used in this study, measured under AM1.5 illumination at 25°C.

x=Ga/(Ga+In)	E_g (eV)	J_{sc} (mA/cm^2)	V_{oc} (V)	Efficiency (%)
0.45	1.28	30.48	0.703	16.1
0.50	1.31	31.01	0.664	12.8
0.50	1.31	29.30	0.740	16.3
0.62	1.39	24.22	0.682	12.04
0.70	1.45	25.29	0.736	11.9
0.70	1.45	26.2	0.740	11.7
1.0	1.68	14.0	0.724	7.00

4.3 Results and discussion

Low temperature condition: Fig. 4-4 shows a typical Photo-capacitance spectrum of CIGS with Ga/III=0.70, measured under normal conditions and saturated conditions at 140 K. The R value defined previously was shown in Fig. 4-4(a) and was almost equal to 1 (the possible reason that the value was lightly smaller than 1 will be discussed later). This indicates that no suppression of carrier recombination due to saturation of the defect level was observed as Fig. 4-4(b) shows. The TPC signal at 0.8 eV at normal condition is much smaller than that at 1.5 eV (I_n(0.8 eV)<< I_n(1.5 eV)) and could be neglected.

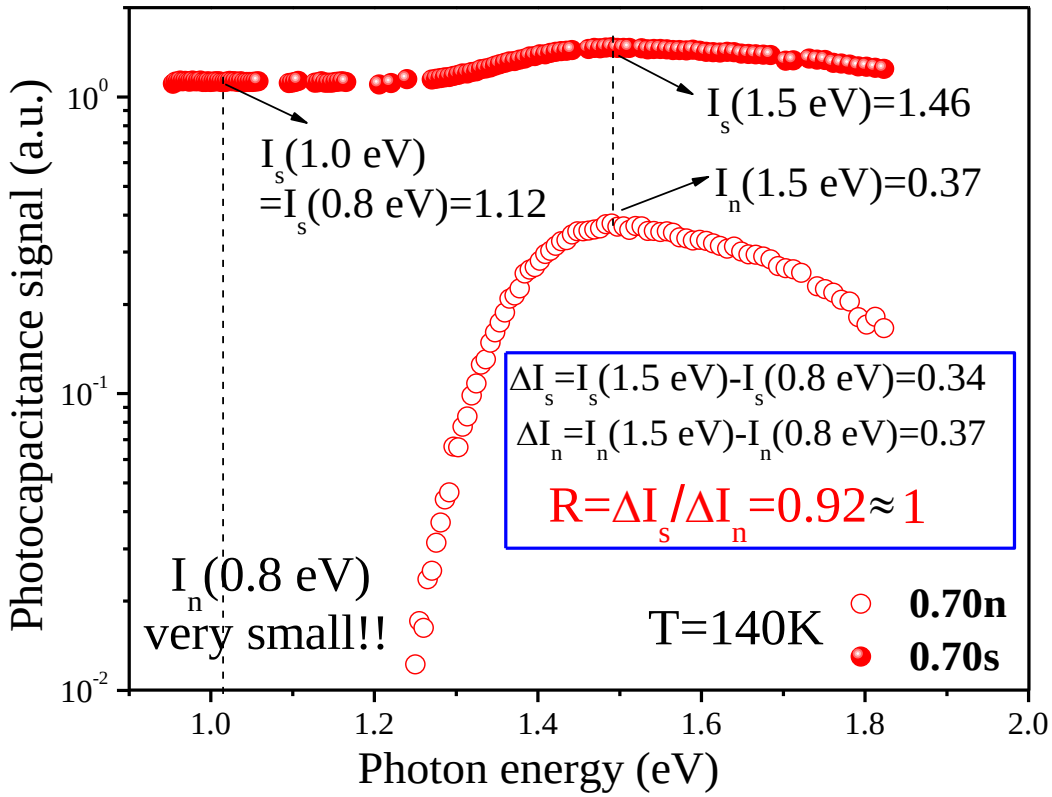

(a)

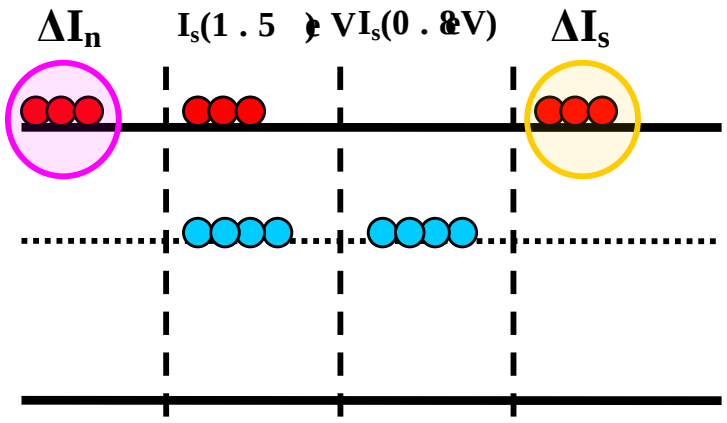

(b)

Fig. 4-4. (a) A typical Photo-capacitance spectrum of CIGS with Ga/III=0.70, measured under normal conditions and saturated conditions at 140 K. The numbers express Ga content, and n indicates normal conditions while s indicates saturated conditions (0.70n and 0.70s). (b) A Schematic diagram which is used to illustrate that at 140 K, no saturation effect was observed due to $\Delta I_n = \Delta I_s$ or R=1.

High temperature condition: Fig. 4-5 shows a typical Photo-capacitance spectrum of CIGS with Ga/III=0.70, measured under normal conditions and saturated conditions at room temperature (RT). The R value defined previously was shown in Fig. 4-5(a) and was greater to 1. This indicates that a suppression of carrier recombination due to saturation of the defect level occured as Fig. 4-5(b) shows.

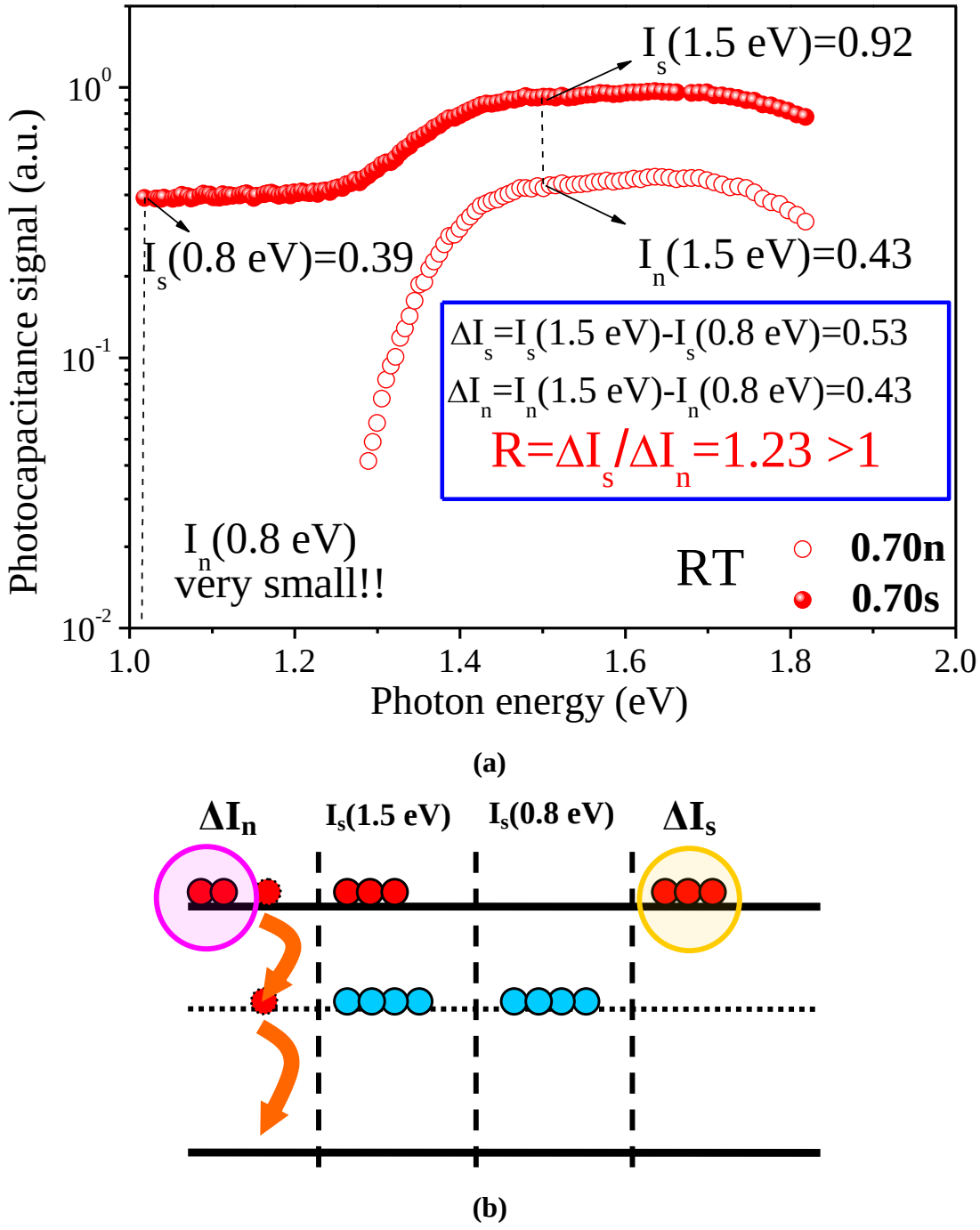

Fig. 4-5. (a) A typical Photo-capacitance spectrum of CIGS with Ga/III=0.70, measured under normal conditions and saturated conditions at room temperature (RT). The numbers express Ga content, and n indicates normal conditions while s indicates saturated conditions (0.70n and 0.70s). (b) A Schematic diagram which is used to illustrate that at RT, saturation effect was observed due to $\Delta I_n < \Delta I_s$ or R>1.

Fig. 4-6(a)(c) and (b)(d) show photo-capacitance spectrum of CIGS with various Ga contents, measured under normal and saturated conditions at 140 K and room temperature, respectively. The sample numbering, such as 0.45n and 0.45s, indicates that the Ga content was 0.45 and the measurements were made under normal and saturated conditions, respectively. The photo-capacitance spectra of six typical samples with different Ga content are shown.

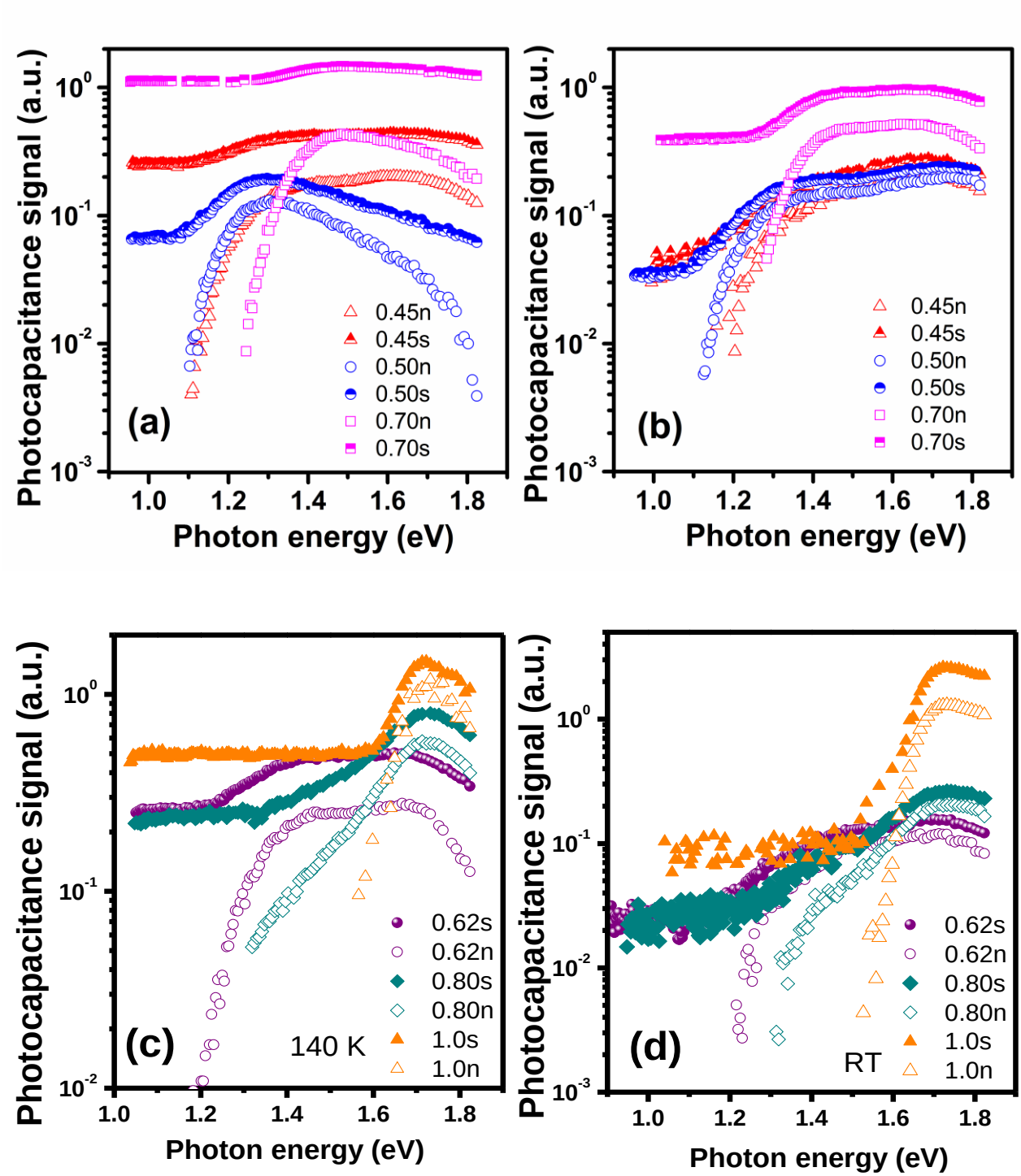

Fig. 4-6. Photo-capacitance spectrum of CIGS with various Ga contents, measured under normal conditions and saturated conditions. The temperatures were (a) (c)140 K and (b) (d) room temperature (RT). The numbers express Ga content, and n indicates normal conditions while s indicates saturated conditions.

Then, the R values obtained from CIGS samples with various Ga contents are shown in Fig. 4-7. At 140 K, almost all of the R values are close to 1. This means that the saturation effect of the 0.8 eV defect can be neglected, since no carrier recombination occurs through this defect level even under normal conditions when the laser light is off. The R values, however, are generally slightly less than 1, which can be explained as follows. Under saturation conditions, there are extra holes left in the valence band that were induced by the 1.55 μm laser light, and this may cause more effective interband recombination than that under normal conditions, since the interband recombination rate is proportional to the effective carrier concentrations in the valance and conduction bands [4-2]. On the other hand, at room temperature, all of the R values were greater than 1. This means that carrier recombination occurs through the defect level under normal conditions, and that there is a suppression of carrier recombination under saturated conditions. Therefore, the 0.8 eV defect acts as a recombination center at room temperature.

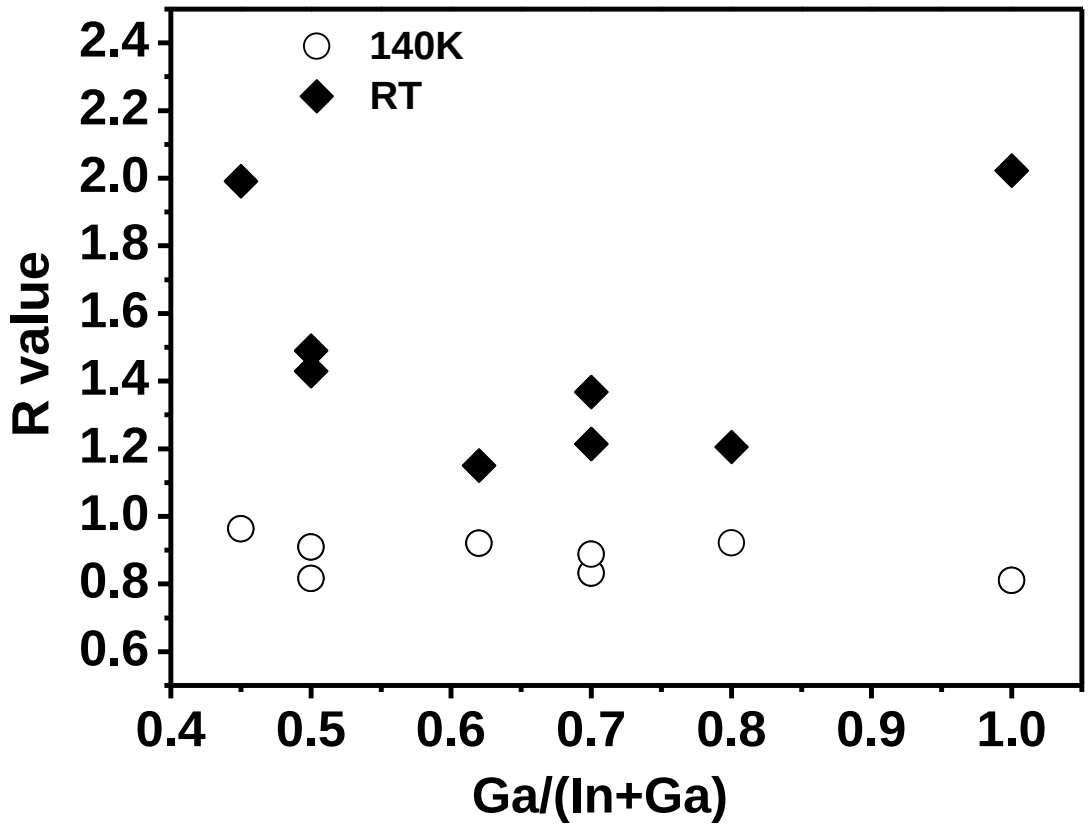

Fig. 4-7. R values for CIGS with various Ga contents. The open circles and solid squares represent results measured at 140 K and room temperature (RT), respectively.

4.4 Summary

A two-wavelength excitation photocapacitance method using a monochromatic probe light in conjunction with a laser light was utilized to study the properties of the defect level centered at 0.8 eV above the valence band in CIGS. A suppression of carrier recombination due to saturation of the defect level was observed at room temperature while no saturation effect was observed at 140 K. The results indicate that the defect level at 0.8 eV acts as a recombination center at least at room temperature. Since the presence of a recombination center often deteriorates the open-circuit-voltage and thus reduces the efficiency, decreasing the concentration of 0.8 eV defects is a promising means of improving cell efficiency.

Reference

[4-1] S. Siebentritt and U. Rau, *Wide-Gap Chalcopyrites*, Springer Verlag, Berlin Heidelberg, 2006, p.69-90.

[4-2] S. M. Sze and Kwok K. Ng, *Physics of semiconductor devices*, John Wiley & Sons, Hoboken, 2006, p.40-45

Chapter 5 Quantitative Investigation of The Properties of Deep-level Defect by Steady-State Photocapacitance and Time-Resolved Photoluminescence Methods

Chapter 3 and Chapter 4 qualitatively characterized the 0.8 eV deep-level defect such as the energy position and its recombination role. However, quantitative information such as the absolute defect density and the cross sections of the defect (including optical cross sections and thermal capture cross sections) are still not known. Thus, in this chapter, quantitative properties of the deep-level defect will be investigated using steady-state photocapacitance method and Time-Resolved Photoluminescence Methods.

5.1 Principle of Steady-state photocapacitance

When photons are sent into the depletion region of a junction, the deep-level occupancy can be changed by the optically induced emission of carriers, leading to a change of the capacitance of the junction. This is the basic idea of either steady-state or transient photocapacitance measurements. If temperature is low enough so that thermal release of trapped carriers can be neglected, the evolution of the occupancy of the level under illumination is given by the classical differential equation [5-1]

$$\frac{dn_t}{dt} = -e_n^o n_t + e_p^o p_t = -\sigma_n^o \Phi n_t + \sigma_p^o \Phi p_t \tag{5-1}$$

where nt and $p_t=N_t-n_t$ are the concentrations of electrons and holes trapped on the level, e_n^o *and* e_p^o are the optical emission rates of the electron from the defect to the conduction band and hole from the defect to the valence band, respectively. σ_n^o and the optical cross sections for the emission of electrons in the conduction band and holes in the valence band, respectively, and Φ is the intensity of the incident light. Fig. 5-1 shows a schematic diagram which describes the related optical parameters of a deep-level defect.

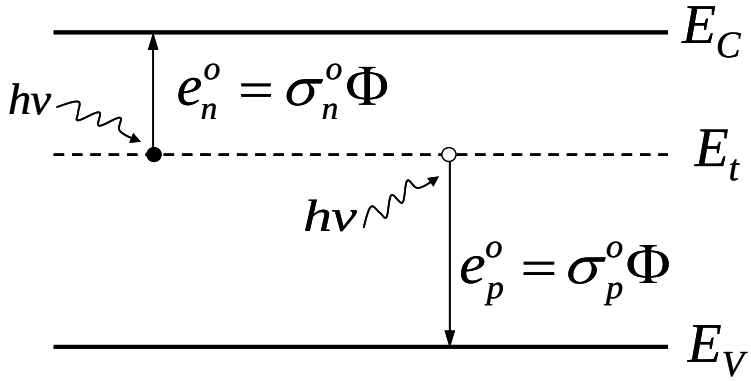

Fig. 5-1. Parameters describing the optical properties of a deep-level defect.
E_C: conduction band; E_t: defect level; E_V: valence band

One of the way to use the relation is to study the time constant τ of the capacitance transient corresponding to Eq. (5-1) [5-2]:

$$\tau = \frac{1}{e_n^o + e_p^o} = \frac{1}{\sigma_n^o \Phi + \sigma_p^o \Phi} \tag{5-2}$$

From Eq. (5-2) we can see that the time constant is related to the sum of the two optical cross sections. Thus this method can be used in a simple way only when one of the two terms is negligible. Very often the steady-state measurements are used when the measurement time is long enough, that is Eq. (5-1) in the time limit $t \to \infty$:

$$(n_t)_\infty = N_t \frac{\sigma_p^o}{\sigma_n^o + \sigma_p^o} \tag{5-3}$$

where both the information of the defect density N_t and optical cross sections are involved. In the case when one of the cross sections dominates (for example $\sigma_p{}^o > \sigma_n{}^o$), the defect density N_t could be obtained.

In real experiments, the parameters of the defect are usually extracted by measuring the photocapacitance transients. The steady-state photo-capacitance of a one-side junction can be expressed as [5-3, 4],

$$\frac{\Delta C_{ss}}{C} = \frac{N_t}{2N_A} \frac{\sigma_p^o}{\sigma_p^o + \sigma_n^o}, \tag{5-4}$$

where N_t is the filled deep-level concentration, N_A is the acceptor concentration, C is the quasi-equilibrium junction capacitance, ΔC_{ss} is the total change (steady-state) in capacitance by photo-irradiation. $\sigma_p{}^o$ and $\sigma_n{}^o$ is the optical cross section of hole and electron, respectively.

In general, for a single deep level contributing to the photo-capacitance transient, the change in capacitance can be written as [5-3, 4],

$$\Delta C(t) = \Delta C_{ss} \cdot (1 - e^{-t/\tau}), \tag{5-5}$$

where ΔC_{ss} is the steady-state photo-capacitance and τ is the time constant of the carrier emission process which is the reciprocal of the emission rate. And τ is given by Eq. (5-2). Fig. 5-2 shows a schematic diagram for describing the capacitance transient for a one-side junction or Schottky junction when only considering a single deep-level defect.

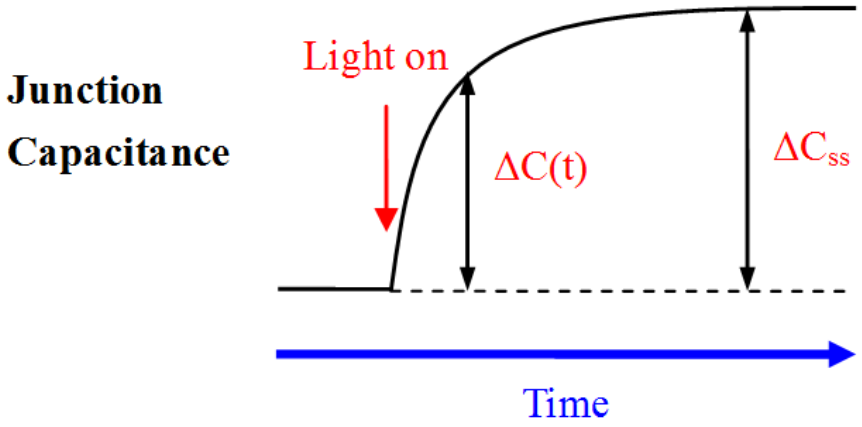

Fig. 5-2. A schematic diagram for describing the capacitance transient for a one-side junction or Schottky junction when only considering a single deep-level defect

5.2 Principle of time-resolved photoluminescence (TRPL)

Time-resolved photoluminescence (TRPL) is a useful method to measure the lifetime of minority carriers in semiconductors. Usually, the minority carrier lifetime is determined by three recombination mechanisms including radiative recombination, non-radiative recombination or Shockley-Read-Hall (SRH) recombination and Auger recombination. Fig. 5-3 shows the schematic diagram for describing the three kinds of recombination processes.

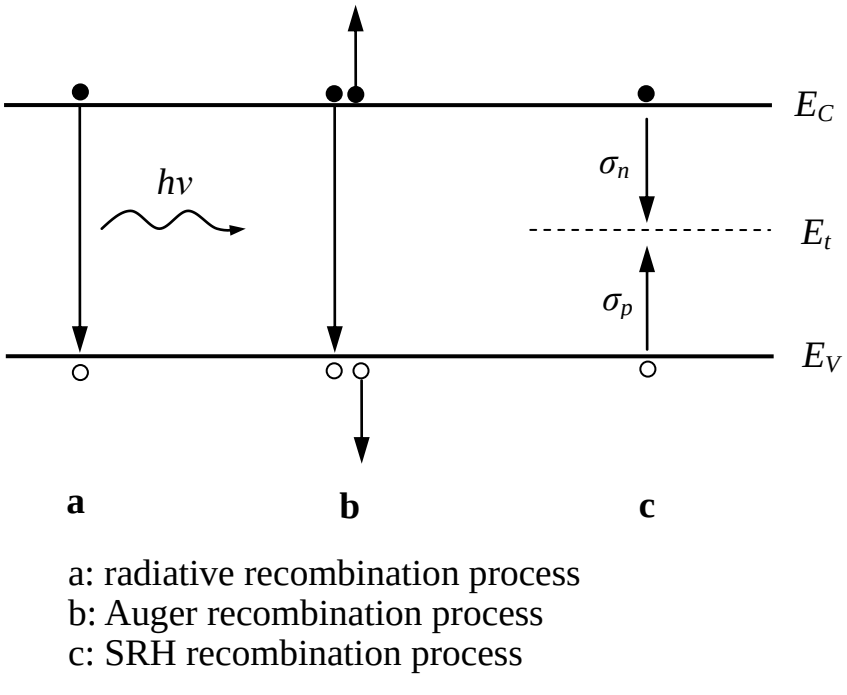

Fig. 5-3. Schematic diagram for describing the three kinds of recombination mechanisms. E_C: conduction band; E_t: defect level in the forbidden gap; E_V: valence band; σ_n: capture cross section of electrons; σ_p: capture cross section of holes

5.2.1 Radiative recombination and radiative lifetime

Radiative recombination is the process by which a electron in the conduction band and a hole in the

valence band recombine to produce a photon of energy $h\nu \sim E_g$ as Fig. 5-3 (process a) shows. The photon emitted may have the energy of the band gap difference or less, depending on how much energy is lost in the mechanism. Photoluminescence is a common way for the optical generation of recombination luminescence. Room-temperature photoluminescence spectra usually show an intense band peaking near E_g which comes from the direct recombination of electron and holes. Other peaks that are observed at energies less than E_g are related to transitions from impurity or exciton states [5-5].

The total radiative recombination rate, given below as R, is proportional to the product of the concentration of occupied states (electrons, n) in the conduction band and that of the unoccupied states in the valence band (holes, p):

$$R = Bnp \qquad (cm^{-3}s^{-1}) \tag{5-6}$$

where B is a constant for a given semiconductor that can actually be calculated from the semiconductor's absorption coefficient (due to the relationship between optical absorption and the recombination process) [5-6]. B has units of cm^3/s.

Eq. (5-6) gives the light output per unit volume of a semiconductor with n electrons and p holes per cm^3. For a semiconductor under illumination, a density of $\rho(r)$ electron-hole pairs is generated, and the general expression for the net photoluminescence from the volume V is written in terms of an integral:

$$\begin{aligned} I_{PL} &= B\int_V [(p_0 + \rho(r))(n_0 + \rho(r)) - n_i^2]dV \\ &= B\int_V [\rho(r)^2 + \rho(r)(p_0 + n_0)]dV \end{aligned} \tag{5-7}$$

where n_0 is the free electron density, p_0 is the free hole-density, n_i is the intrinsic density per cm^3 which is related to the effective densities of states in conduction band (N_C) and valence band (N_V) [5-7]. $\rho(r)$ is the concentration of excess hole-electron pairs produced by the excitation. Here, Bn_i^2 is the equilibrium or blackbody luminescence. Under steady-state excitation, $\rho(r)$ remains constant in time, and therefore I_{PL} remains constant. Under pulsed excitation, $\rho(r)$ decreases because of recombination and I_{PL} decays accordingly. This is the physical process basic to measuring the minority carrier lifetime by time-resolved photoluminescence. Using the symmetric notation (N and ρ) and neglecting the steady state minority carrier density, when assuming spatially uniform and instantaneous injection ρ_0 of electron-hole pairs per cm^3, the radiative decay of ρ is given by

$$\frac{d\rho}{dt} = -B(N\rho + \rho^2) \tag{5-8}$$

The solution to this differential equation is

$$\rho(t) = \frac{\rho_0 \exp(-t/\tau_R)}{1 + \frac{\rho_0}{N}(1 - \exp(-t/\tau_R))} \tag{5-9}$$

Here, the radiative lifetime τ_R is defined as

$$\tau_R \equiv \frac{1}{BN} \tag{5-10}$$

5.2.2 SRH recombination and SRH lifetime

Non-radiative recombination is the process by which electron-hole pairs recombined via deep defect levels within the forbidden band as Fig. 5-3 (process c) shows. Due to the contribution of Shockley, Read [5-8] and Hall [5-9], this common mechanism in minority carrier kinetics is the frequently called Shockley-Read-Hall (SRH) recombination mechanism. The physics involves minority carrier capture at defects that have quantum levels in the bandgap of the semiconductor. The SRH recombination rate is usually shown to be [5-10, 11, 12]

$$R_{SRH} = \frac{\sigma_p \sigma_n \upsilon_{th} N_t (pn - n_i^2)}{\sigma_n \left[n + n_i \exp(\frac{E_t - E_i}{kT}) \right] + \sigma_p \left[p + n_i \exp(\frac{E_i - E_t}{kT}) \right]} \tag{5-11}$$

where N_t is the volume density of deep levels; σ_n and σ_p are capture cross sections of electrons and holes, respectively; and Et is the energy level of the trap. n and p are the electron and hole concentrations, respectively, and υ_{th} is the thermal velocity of the electron or hole. If electron-hole pairs of volume density $\rho=\Delta n, \Delta p$ are injected, then the instantaneous values of p and n can be written as

$$p = p_0 + \rho, \quad n = n_0 + \rho \tag{5-12}$$

For a doped semiconductor, one has either $n_0 >> p_0$ (n-type) *or* $p_0 >> n_0$ (p-type). Taking the case of an p-type material, one can derive the recombination rate for electrons at a single energy level at E_t in the forbidden gap. This case is symmetrical to that of hole recombination in n-type material. In this expression, $p_0=N_A$ (acceptor concentration) and n_0~0. Therefore,

$$R_{SRH} = \frac{\sigma_p \sigma_n \upsilon_{th} N_t (\rho N_A + \rho^2)}{\sigma_n \left[\rho + n_i \exp(\frac{E_t - E_i}{kT}) \right] + \sigma_p \left[N_A + \rho + n_i \exp(\frac{E_i - E_t}{kT}) \right]} \tag{5-13}$$

A logarithmic plot of RSRH versus E_i-E_t shows a steep peak at $E_t=E_i$. The maximum recombination rate occurs at defects levels that lie at or near midgap.

The SRH lifetime is defined as

$$\tau_n \equiv \frac{1}{\sigma_n N_t \upsilon_{th}} \quad \textit{and} \quad \tau_p \equiv \frac{1}{\sigma_p N_t \upsilon_{th}} \tag{5-14}$$

Then Eq. (5-13) is rewritten as

$$R_{SRH} = \frac{[\rho N_A + \rho^2]}{\tau_p \left[\rho + n_i \exp(\frac{E_t - E_i}{kT}) \right] + \tau_n \left[N_A + \rho + n_i \exp(\frac{E_i - E_t}{kT}) \right]} \tag{5-15}$$

Generally, N_A is much greater than the terms containing n_i in Eq. (5-15), when using the symmetric notation with the majority-carrier doping equal to N ($N = N_A$), we can get,

$$R_{SRH} = \frac{[\rho N_A + \rho^2]}{\tau_{maj}\rho + \tau_{\min}\left[N + \rho\right]} \tag{5-16}$$

Here, τ_{min} and τ_{maj} are the minority and majority carrier SRH lifetimes, respectively. For the low injection case of $\rho << N$, Eq. (5-16) simplifies to

$$R_{SRH} = \frac{\rho}{\tau_{\min}} \tag{5-17}$$

here

$$\tau_{\min} = \frac{1}{\sigma N_t \upsilon_{th}} \tag{5-18}$$

σ is the capture cross section for the minority carrier.

From Eq. (5-17), we can see that the recombination rate at the SRH level is controlled by the capture of the minority carrier by the defect. Thus the product of the capture cross section and the defect density appears in the recombination rate. In low injection, the majority carrier density is much greater than the minority carrier density. After minority carrier capture, the center is reset by the subsequent capture of a majority carrier. Because of the high concentration of majority carriers, capture occurs at a very high rate. Thus, in low injection, the SRH lifetime is determined solely by the minority carrier capture rate. When more than one deep-level defect type is present, the total SRH low-injection lifetime is described by a single minority carrier lifetime τ, where

$$\frac{1}{\tau} = \sum_i \frac{1}{\tau_i} \tag{5-19}$$

where τ_i is the SRH lifetime for each specific type of defect.

5.2.3 Auger recombination and Auger lifetime

Auger recombination is a nonradiative recombination process in which the energy of the electron-hole pair is transformed into the kinetic energy of a free particle. In Auger recombination, the excess energy given off by an electron recombining with a hole is given to a second electron (in either band) instead of just emitting the energy as a photon as Fig. 5-3 (process b) shows. The newly excited electron then gives up its additional energy in a series of collisions with the lattice [5-6], relaxing back to the edge of the band. The Auger process is usually seen at relatively high carrier concentrations [5-13].Thus, this effect is a result of interactions between multiple particles, including multiple electrons and a hole. For the usual three-carrier Auger recombination lifetime, τ_a, for n and p-type semiconductors varies as [5-14],

$$\frac{1}{\tau_a} = Anp + Cn^2 \quad \text{(n-type)}, \qquad \frac{1}{\tau_a} = A\,n\,p + C_1^2 \quad \text{(p-type)} \tag{5-20}$$

where, the coefficient *C* is a cross section that is proportional to the transfer efficiency of energy to the majority carrier. The A coefficient represents the transfer of energy to the minority carrier.

5.3 Experimental setup

5.3.1 Steady-state photocapacitance measurements

Fig. 5-3 shows the setup diagram for the steady-state photocapacitance measurements. The measurements were performed with a supercontinuum laser (SC450, Fianium Ltd.) as the excitation source, using a monochromator-based setup (MS 2004i, SOLAR TII, Ltd), the total power output of the laser source is about 4 W. The intensity of the light source (at 0.8 eV, 800 μW) was calibrated by a photodiode (PM100D, THORLABS, Inc.). Higher order wavelengths were filtered by a long pass filter (OD>5, FELH0800, THORLABS, Inc.). The spot size of the light beam is about 0.785 mm^2, and the photon flux reaching the surface of the samples was controlled in the order of 10^{15} photons/(cm^2·s) by using combinations of neutral filters. The light intensity of this order is low enough so that the magnitude of the change in photocapacitance is only a function of photon energies [5-15]. The samples for photocapacitance measurements were small circles with diameter of 1 mm and cell structures, which were patterned by photolithography process. The sample temperature was maintained at 60 K to minimize thermal emission from deep defects. Prior to the measurements, the samples were allowed to relax under dark conditions at room temperature for a sufficiently long time. The capacitance measurements were made at zero bias. The "turn-on" and "turn-off" of the illumination on the cell were controlled by an electronic shutter. The time-dependent capacitance signal was measured with a Boonton 72B capacitance meter operating at 1 MHz, and the steady-state photocapacitance transients (stable capacitance under illumination) were recorded.

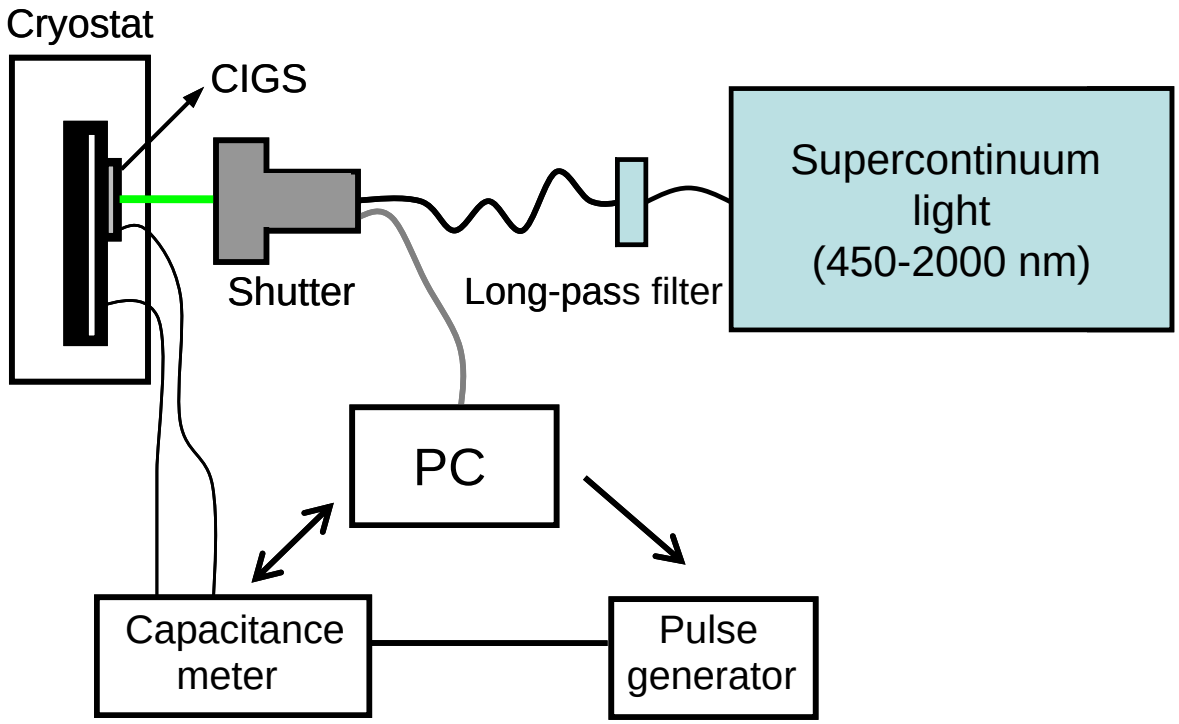

Fig. 5-3. Schematic diagram of the setup for steady-state photocapacitance measurements

5.3.2 Time-resolved photoluminescence measurements

TRPL measurements were carried out at room temperature with a confocal laser scanning microscope using a 635 nm diode laser (Scientex OPG-3300) for excitation. The laser source was operated in a pulsed mode with a pulse width and repetition rate of 100 ps and 2-5 MHz, respectively. An InGaAs-based photomultiplier tube (Hamamatsu H10330A-75) was used to detect the signals for the wavelength longer than 950 nm and an avalanche photodiode (Becker&Hickl GmbH) was used for the wavelength shorter than 900 nm.

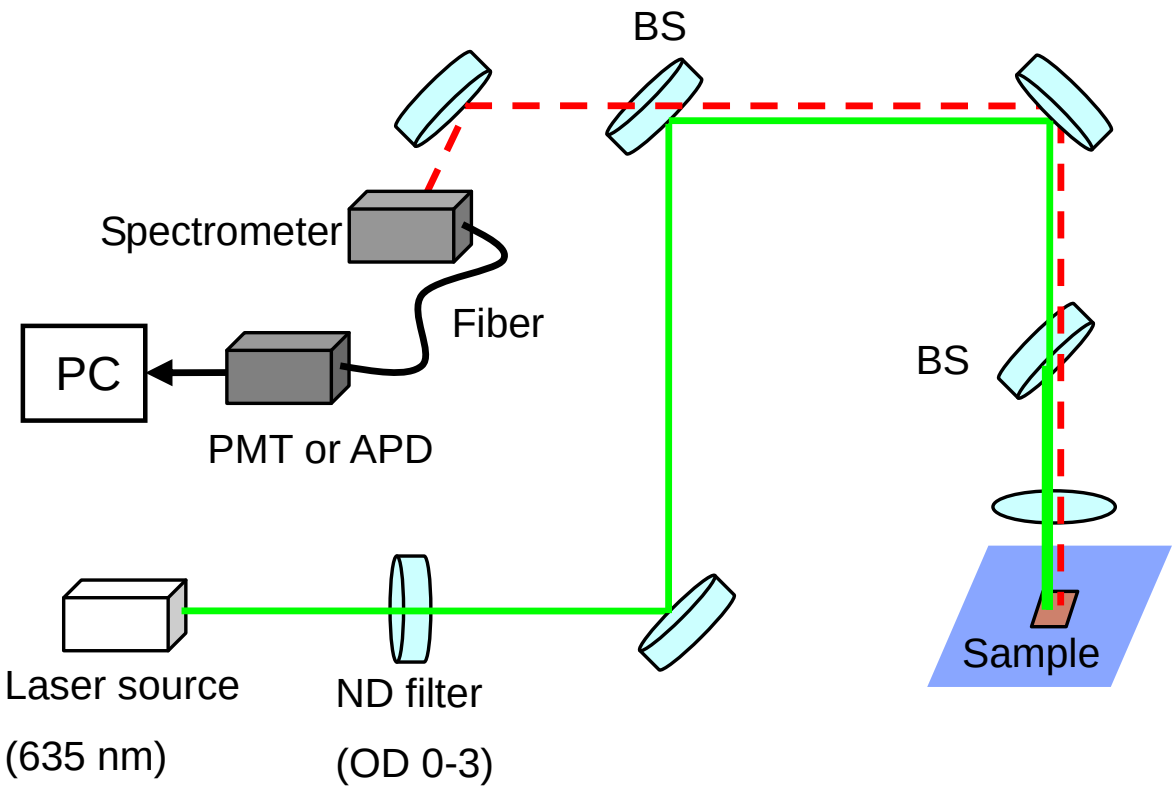

Fig. 5-4 Schematic diagram of the setup for Time-resolved photoluminescence measurements

5.3.3 CIGS solar cells for measurements

The parameters of CIGS thin-film solar cells used for the steady-state photocapacitance measurements are listed in Table 5-1. The Ga content x was controlled to be 0.30-0.80, and the copper content of the CIGS films was roughly fixed at approximately Cu/(In+Ga) = 0.9. The detailed deposition conditions for the CIGS films were described previously in Chapter 1. The TRPL measurements were made using CdS-covered CIGS specimens with different Ga content, which were prepared by chemical bath deposition (CBD), to exclude the reduction in lifetime caused by air oxidation, [5-16], the corresponding solar cells' parameters are shown in Table 5-1.

Table 5-1. CIGS device parameters used in this study, measured under AM1.5 illumination at 25°C.

Ga/(Ga+In) (x)	J_{sc} (mA/cm^2)	V_{oc} (V)	FF	Efficiency (%)
0.30	29.74	0.687	0.78	15.89
0.40	27.88	0.730	0.77	15.67
0.52	26.48	0.700	0.73	13.57
0.62	24.39	0.718	0.72	12.67
0.76	22.35	0.738	0.71	11.15
0.80	20.30	0.731	0.68	10.14

5.4 Results and discussion

Fig. 5-4(a) shows the photo-capacitance transients for CIGS with different Ga content measured at 60 K. The light was irradiated to the sample for about 30 minutes so as to reach the steady state. The increase of capacitance by photo-irradiation indicates a dominant contribution of hole emission ($\sigma_p^o >> \sigma_n^o$). Assuming an initial condition that the defect level is empty (since before the measurements, the samples were relaxed for long enough time, the assumption is reasonable), the concentration of the deep-level defect could be estimated. Fig. 5-4(b) shows the fitting results with Eq. (5-5) for the CIGS sample with Ga content of 0.40.

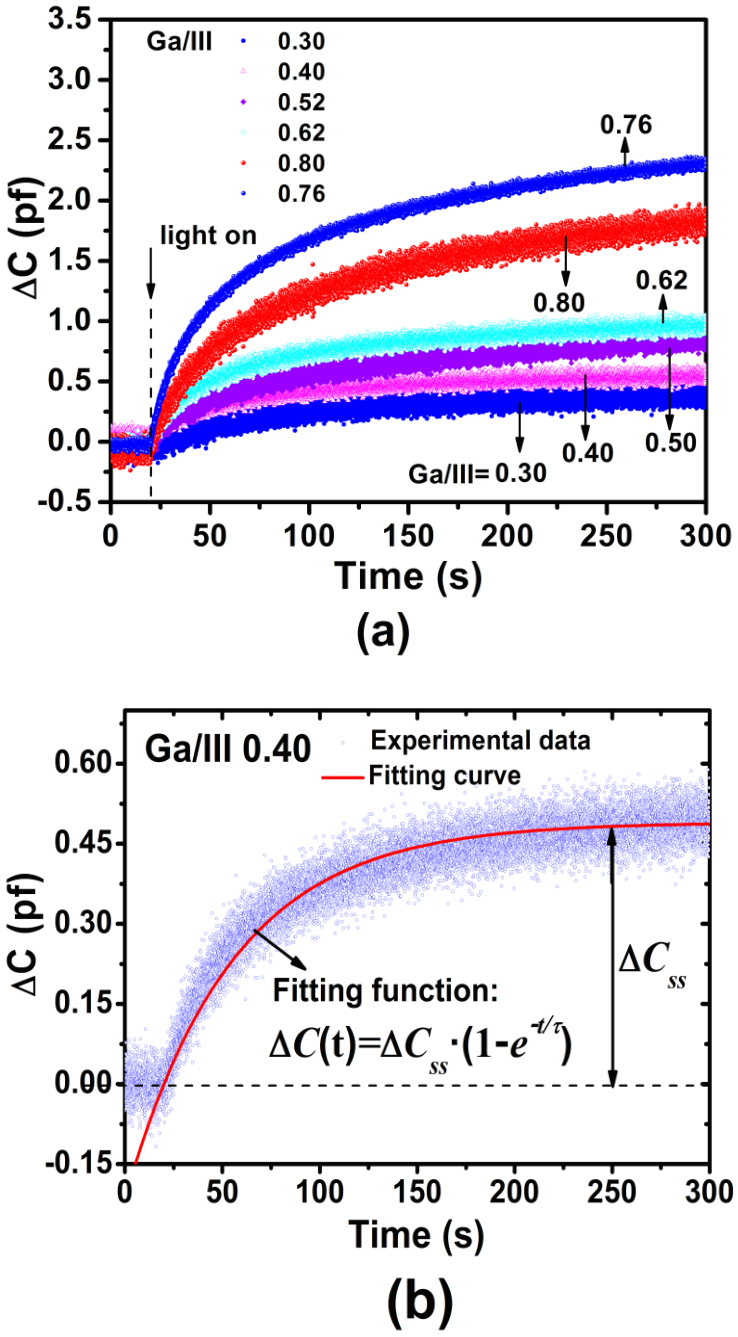

Fig. 1. (a) Photocapacitance transients for CIGS with various Ga content measured at 60 K. (b) Fitting results with Eq. (5-5) for the CIGS sample with Ga content of 0.40.

Fig. 5-5 shows the results of defect concentration and photo-ionization cross section of CIGS with various Ga content. The defect concentration was estimated to be in the order of 10^{-13}-10^{-14} cm^{-3} and increased with Ga content, this result is in accordance with our previous work where the defect concentration was found to increase with Ga content by using the transient photo-capacitance method as shown in Chapter 3. The photo-ionization cross section of the hole was estimated to be in the order of 10^{-17}-10^{-16} cm^2 and shows also increasing tendency with Ga content.

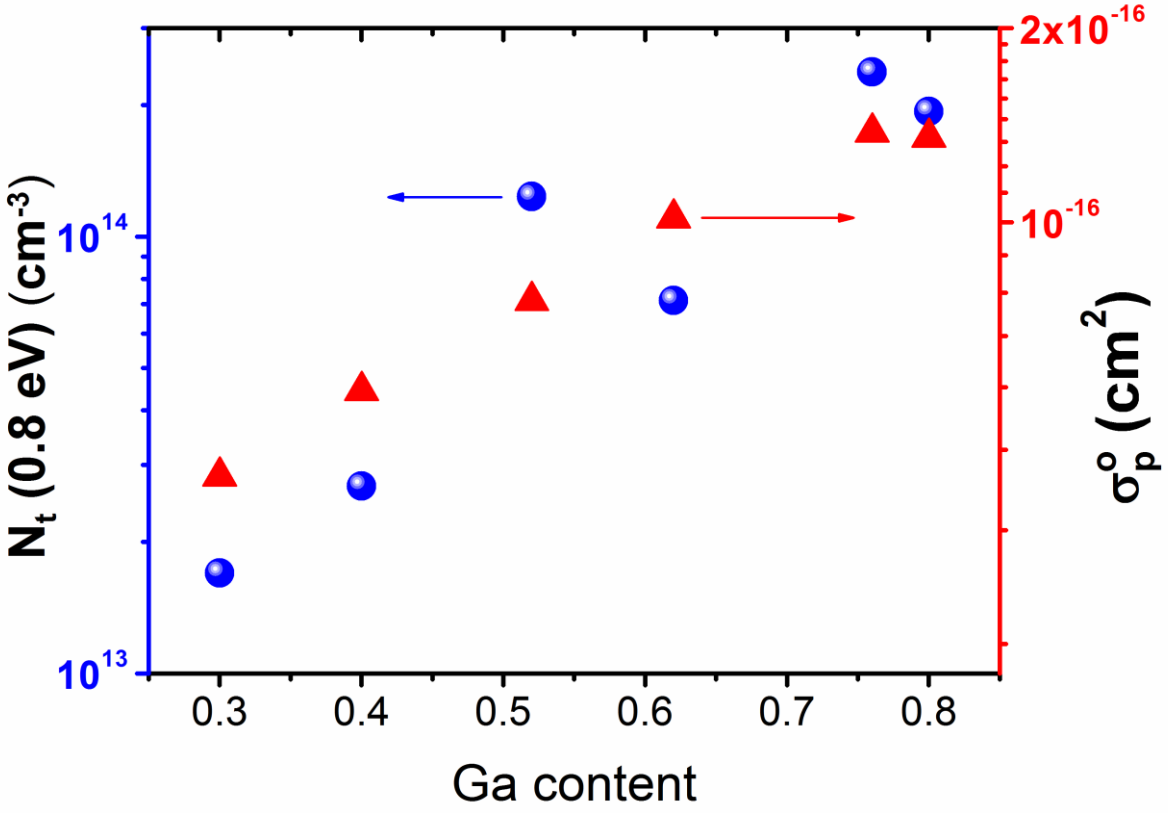

Fig. 5-5. Concentration and photo-ionization cross section (σ_p^o) of the deep-level defect

Fig. 5-6 shows the photoluminescence (PL) spectra of CIGS films with Ga content varied from 0.30 to 0.80. The red vertical line indicates the band gap energy estimated from the relationship between Ga content and CIGS band gap energy in which the band gap energy increases with the Ga content [5-17]. As the Ga content increases, the difference between the band gap energy and the PL emission peak becomes larger which indicated that for high Ga content CIGS, the radiative recombination was gradually dominated by deeper donor-acceptor (DA) transitions since the shift in the emission peaks toward the higher-energy side with increasing excitation-light power density was confirmed [5-18].

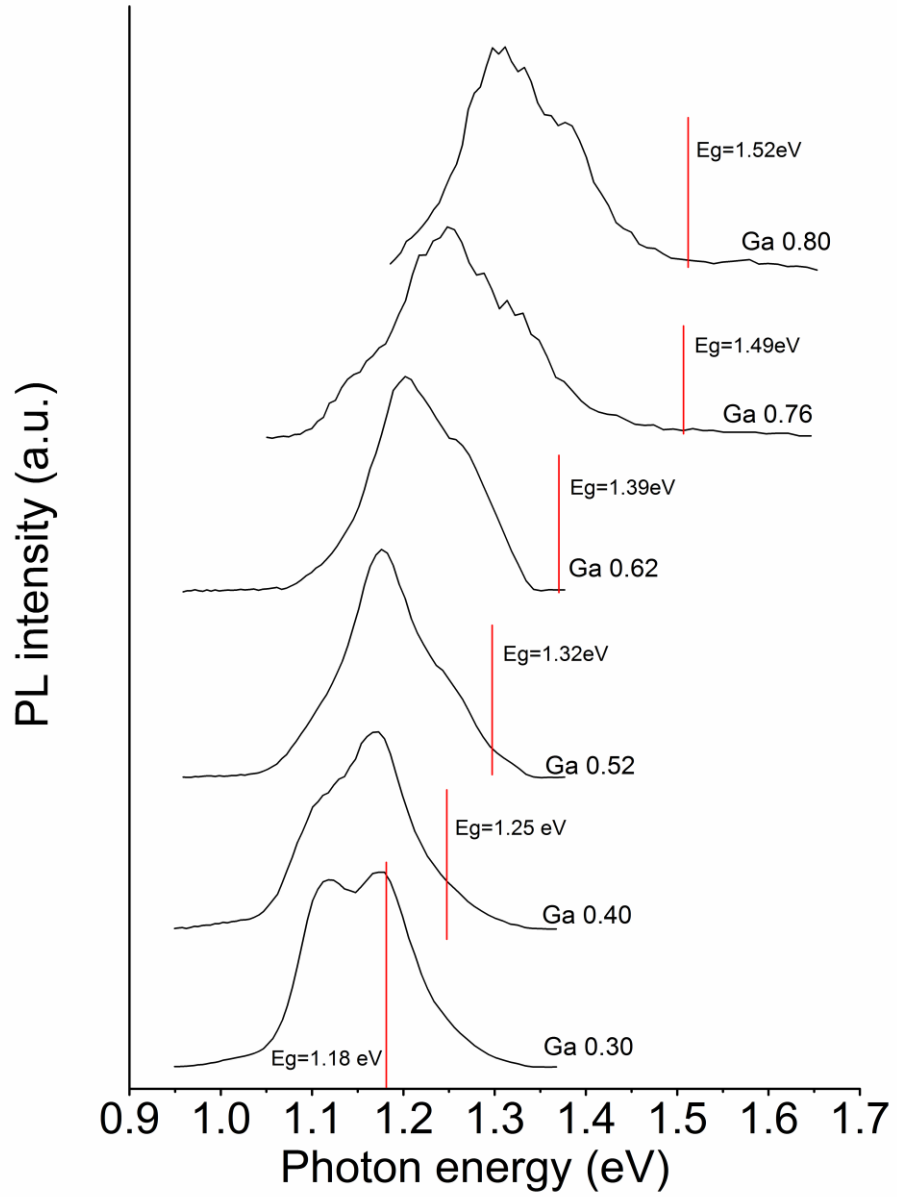

Fig. 5-6. PL spectra of CIGS films with Ga content varied from 0.30 to 0.80.

Fig. 5-7(left part) shows the PL decay curves of CIGS films with Ga content varied from 0.30 to 0.80 measured at room temperature. For each film, the decay curve was measured at the wavelength showing maximum intensity of the PL spectrum. The decay curves were well fitted by bi-exponential formula [5-19], that is,

$$I = I_1 \exp(-t/\tau_1) + I_2 \exp(-t/\tau_2), \tag{5-21}$$

where I is the luminescence intensity at time t, and I_1 and I_2 are coefficients, τ_1 and τ_2 are the fast and slow decay lifetimes, respectively. The minority carrier lifetime was evaluated using the slow emission component (lifetime τ_2) which approximately corresponds to the values observed under low intensity irradiation [5-16]. Fig. 5-7(right part) shows an example of the fitting results with Eq. (5-6) for the CIGS specimens with Ga content of 0.30.

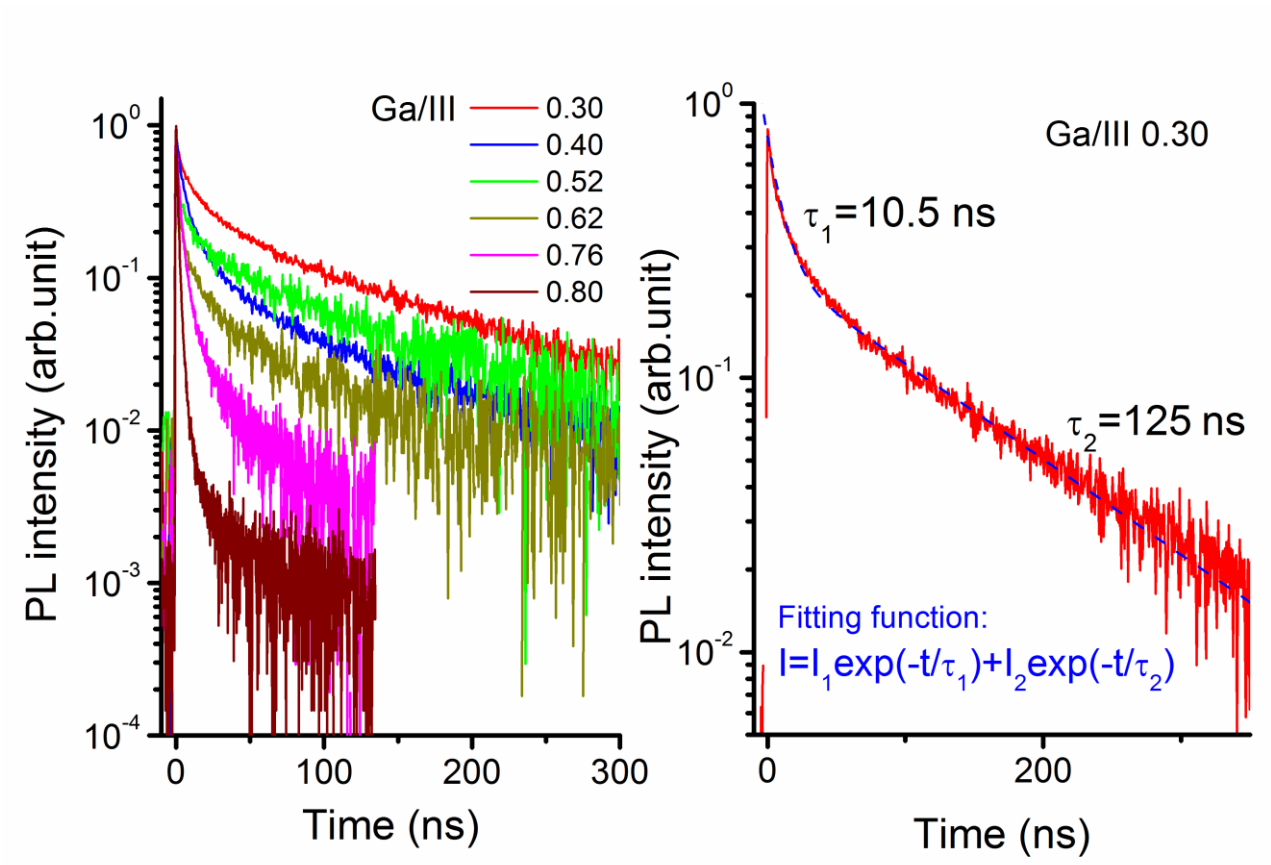

Fig. 5-7. (Left) PL decay curves for CIGS films with Ga content varied from 0.30 to 0.80. (Right) Fitting results with the bi-exponential function for the CIGS sample with Ga content of 0.30.

The minority carrier lifetime of various Ga content was shown in Table 5-1 with the conversion efficiency of corresponding solar cell. It can be obviously seen that the minority carrier lifetime decreases with increasing Ga content and higher conversion efficiency corresponds to longer minority carrier lifetime.

Table 5-1. Minority carrier lifetime of CIGS thin films with various Ga content and efficiency of corresponding solar cell devices

Ga/III (x)	0.30	0.40	0.52	0.62	0.76	0.80
Efficiency (%)	15.89	15.67	13.57	12.67	11.15	10.14
Lifetime (ns)	125	110	95	58	25	14

Generally, the PL decay includes radiative decay which is caused by interband recombination and nonradiative decay caused through deep level defects, (Auger recombination would also influence the decay lifetime, however, this process was usually negligible at low carrier doping condition and in relatively wide gap material as in our case). Simplifying the nonradiative recombination can be considered as Shockley-Read-Hall (SRH) recombination, the measured PL decay lifetime is then given by [5-20],

$$\frac{1}{\tau_{TRPL}} = \frac{1}{\tau_{rad}} + \frac{1}{\tau_{SRH}}, \tag{5-22}$$

where τ_{TRPL} is the measured PL decay lifetime, τ_{rad} is the lifetime of radiative recombination under low intensity irradiation or in the low carrier injection regime and is described by Eq. (5-10)

$$\tau_{rad} = \frac{1}{BN_A}, \tag{5-23}$$

where B is the radiative recombination coefficient and N_A is the net majority carrier density. τ_{SRH} is the lifetime of nonradiative recombination via deep defects and in low carrier injection regime can be described by Eq. (5-18)

$$\tau_{SRH} = \frac{1}{N_t \upsilon_{th} \sigma} \tag{5-24}$$

where N_t is the defect density, υ_{th} is the thermal recombination velocity and σ is the capture cross section of the defect.

Taking a radiative recombination coefficient of B=8×10^{-11}~1.6×10^{-10} cm^{-3}s^{-1} [5-21], and the net majority carrier concentration N_A of 10^{15}~10^{16} cm^{-3} which was obtained from the capacitance-voltage (C-V) measurements, the radiative lifetime for CIGS can be evaluated to be longer than 1 μs, which is much longer than the obtained lifetimes as shown in Table 5-1. Thus the minority carrier lifetime was considered to be dominated by non-radiative recombination via deep defects. Although there are several kinds of defects in CIGS working as nonradiative recombination center such as impurity phases (e.g., $Cu_{2-x}Se$ and Cu(In,Ga)3Se5) [5-22, 23], point defects (e.g., vacancies and antisite defects) [5-24, 25], and grain boundaries[5-26, 27, 28], as has been reported previously in chapter 4, we have a clear result that the 0.8

eV defect was proved to act as nonradiative recombination center at room temperature by a two-wavelength excitation photo-capacitance method. Therefore, it may be reasonable to evaluate the electron capture cross section by equation (5-24) using the value of τ_{SRH} from the PL decay time and N_t from the photo-capacitance measurements. The typical value of the capture cross section for 0.8 eV defect is 10^{-14} cm^2 and the result is shown in Table 5-2 and Fig. 5-8 correlated with the conversion efficiency.

Table 5-2. Capture cross section of electron (σ_n) at 0.8 eV defect level and density of 0.8 eV defect dependent on Ga/III ratio

Ga/III (x)	0.30	0.40	0.52	0.62	0.76	0.80
σ_n (10^{-14} cm^2)	4.3	4.9	1.9	2.1	1.6	4.0
N_t(0.8 eV) (10^{14} cm^{-3})	0.17	0.27	1.23	0.71	2.38	1.93

As shown in Fig. 5-8, the defect concentration and lifetime seems to have a correlation with the conversion efficiency but the capture cross section does not have close correlation with the efficiency.

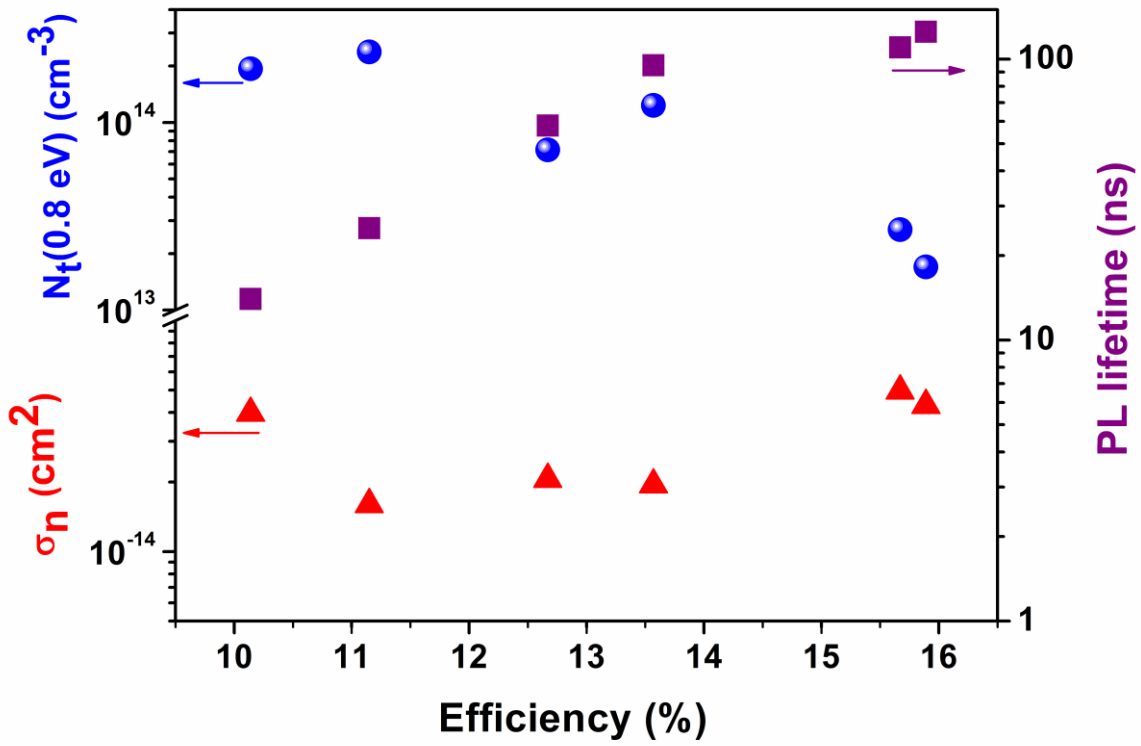

Fig. 5-8. Relationship between the density of 0.8 eV defect (N_t(0.8 eV)), capture cross section of electron (σ_n) at 0.8 eV defect level, PL decay lifetime (minority carrier lifetime) and efficiency of CIGS solar cells.

5.5 Summary

The properties of the deep-level defect located 0.8 eV above the valence band in $Cu(In_{1-x},Ga_x)Se_2$ (CIGS) thin films were investigated using the steady-state photo-capacitance (SSPC) and time-resolved photoluminescence (TRPL) measurements. Quantitative information of this defect was extracted. The defect concentration, photo-ionization cross section and electron capture cross section were evaluated to be in the order of 10^{13}~10^{14} cm^{-3}, 10^{-17}~10^{-16} cm^2, and 10^{-14} cm^2, respectively, in the range of the Ga content x from 0.30 to 0.80. By comparing the obtained values with the device performance, the higher defect concentration seem to be important causes of the degradation of the conversion efficiency of CIGS solar cells with higher Ga content. Therefore, it is necessary to diminish the defect to improve cell efficiency, especially for CIGS samples with high Ga content.

Reference

[5-1] A. Chantre, G. Vincent, D. Bois, Deep-level optical spectroscopy in GaAs, Phys. Rev. B **23** (1981) 5335.

[5-2] C. T. Sah, L. Forbes, L. L. Rosier, and A. F. Tasch, Thermal and optical emission and capture rates and cross sections of electrons and holes at imperfection centers in semiconductors from photo and dark junction current and capacitance experiments, Solid State Electron, **13** (1970) 759.

[5-3] A. Hierro, D. Kwon, S. A. Ringel, S. Rubini, E. Pelucchi and A. Franciosi, Photocapacitance study of bulk deep levels in ZnSe grown by molecular-beam epitaxy, J. Appl. Phys. **87** (2000) 730.

[5-4] P. Blood and J. W. Orton, *The electrical The Electrical Characterization of Semiconductors: Majority Carriers and Electron States*, Academic, San Diego, 1992.

[5-5] R. S. Knox, Theory of Extitons, Solid State Physics (F. Seitz and D. Turnbull, eds.), Supplement 5. Academic Press, New York, 1963.

[5-6] M. A. Green, *Solar Cells: Operating Principles, Technology, and System Applications*. Englewood Cliffs: Prentice-Hall, Inc., 1982

[5-7] S. M. Sze and Kwok K. Ng, *Physics of semiconductor devices*, John Wiley & Sons, Hoboken, 2006.

[5-8] W. Shockley, and W. T. Read, Statistics of the Recombinations of Holes and Electrons, Phys. Rev. **87** (1952) 835.

[5-9] R. N. Hall, Electron-Hole Recombination in Germanium, Phys. Rev. **87** (1952) 387.

[5-10] A. S. Grove, *Physics and Technology of Semiconductor Devices*, John Wiley and Sons, Inc., New York. 1967, p.129.

[5-11] S. M. Sze, *Physics of Semiconductor Devices*, Wiley-lnterscience, New York, 1981.

[5-12] R. K. Ahrenkiel, M. S. Lundstrom, *Minority Carriers In III-V Semiconductors: Physics and Applications*, Academic Press, Inc., San Diego, 1993.

[5-13] P. T. Landsberg, *Recombinarion in Semiconductors*, Cambridge University Press, Cambridge 1991.

[5-14] J. I. Pankove, *Optical Processes in Semiconductors*, Dover Publications, New York, 1971.

[5-15] S. H. Chiao and G. A. Antypas, Photocapacitance effects of deep traps in n‐type InP, J. Appl. Phys. **49** (1978) 466.

[5-16] W. K. Metzger, I. L. Repins, M. Romero, P. Dippo, M. Contreras, R. Noufi and D. Levi, Recombination kinetics and stability in polycrystalline Cu(In,Ga)Se_2 solar cells, Thin Solid Films **517**, 2360 (2009).

[5-17] M. Turcu, I.M. Kotschau and U. Rau, Band alignments in the Cu(In,Ga)(S,Se)2 alloy system determined, Appl. Phys. A **73** (2001) 769-772.

[5-18] S. Siebentritt and U. Rau, *Wide-Gap Chalcopyrites* (Springer Verlag, Berlin Heidelberg, 2006) p. 113-156.

[5-19] T. Sakurai, K. Taguchi, M. M. Islam, S. Ishizuka, A.Yamada, K. Matsubara, S. Niki and K. Akimoto, Time-Resolved Microphotoluminescence Study of Cu(In,Ga)Se_2, Jpn. J. Appl. Phys. **50** (2011) 05FC01.

[5-20] P. Bhattacharya, *Semiconductor Optoelectronic Devices*, Prentice-Hall, Upper Saddle River, New Jersey, 1997, Chaps. 2 and 3.

[5-21] J. H. Werner, J. Mattheis and U. Rau, Efficiency limitations of polycrystalline thin film solar cells: case of Cu(In,Ga)Se_2, Thin Solid Films **480** (2005) 399.

[5-22] V. Izquierdo-Roca, A. Perez-Rodrı´guez, A. Romano-Rodriguez, J. R. Morante, J. Alvarez-Garcia, L. Calvo-Barrio, V. Bermudez, P. P. Grand, O. Ramdani, L. Parissi and O. Kerrec, Raman microprobe characterization of electrodeposited S-rich CuIn(S,Se)$_2$ for photovoltaic applications: Microstructural analysis, J. Appl. Phys. **101** (2007) 103517.

[5-23] M. M. Islam, T. Sakurai, S. Otagiri, S. Ishizuka, A. Yamada, K. Sakurai, K. Matsubara, S. Niki, and K. Akimoto, Determination of Cu(In1−xGax)3Se5 defect phase in MBE grown Cu($In_{1-x}Ga_x$)Se_2 thin film by Rietveld analysis, Sol. Energy Mater. &Sol. Cells **95** (2011) 231.

[5-24] S. Zhang, S.-H. Wei, A. Zunger, and H. Katayama-Yoshida, Defect physics of the CuInSe2 chalcopyrite semiconductor, Phys. Rev. B **57** (1998) 9642.

[5-25] S. Lany and A. Zunger, Light- and bias-induced metastabilities in Cu(In,Ga)Se_2 based solar cells caused by the (V_{Se}-V_{Cu}) vacancy complex, J. Appl. Phys. **100** (2006) 113725.

[5-26] M. Gloeckler, J. R. Sites, and W. K. Metzger, Grain-boundary recombination in Cu(In,Ga)Se_2 solar cells, J. Appl. Phys. **98** (2005) 113704.

[5-27] S. Siebentritt and U. Rau, *Wide-Gap Chalcopyrites*, Springer, Heidelberg, 2006, p. 193.

[5-28] U. Rau, K. Taretto, and S. Siebentritt, Grain boundaries in Cu(In, Ga)(Se, S)$_2$thin-film solar cells, Appl. Phys. A **96** (2009) 221.

Chapter 6 Electronic structure of deep-level defects in CIGS thin films

In this chapter, the electronic structure of the 0.8 eV deep-level defect in CIGS thin films is discussed based on the temperature dependence of transient photocapacitance spectrum and steady-state photocapacitance measurements with excitation with light intensity.

6.1 Temperature dependence of transient photocapacitance spectrum

The details about TPC measurements have been demonstrated in Chapter 3. To understand more about the TPC signal, the temperature dependent photocapacitance experiment was performed [6-1]. Fig. 6-1 shows a typical TPC spectrum for the CIGS thin-film solar cell with Ga/III ratio of 0.70 measured in the temperature range of 60 to 340 K. The intensity of sub-bandgap TPC signal decreased with increasing temperature while significant variation in the inter-band signal was not observed with temperature. The decreasing of TPC intensity with temperature can be attributed to the thermal de-trapping of charges in defect levels with temperature.

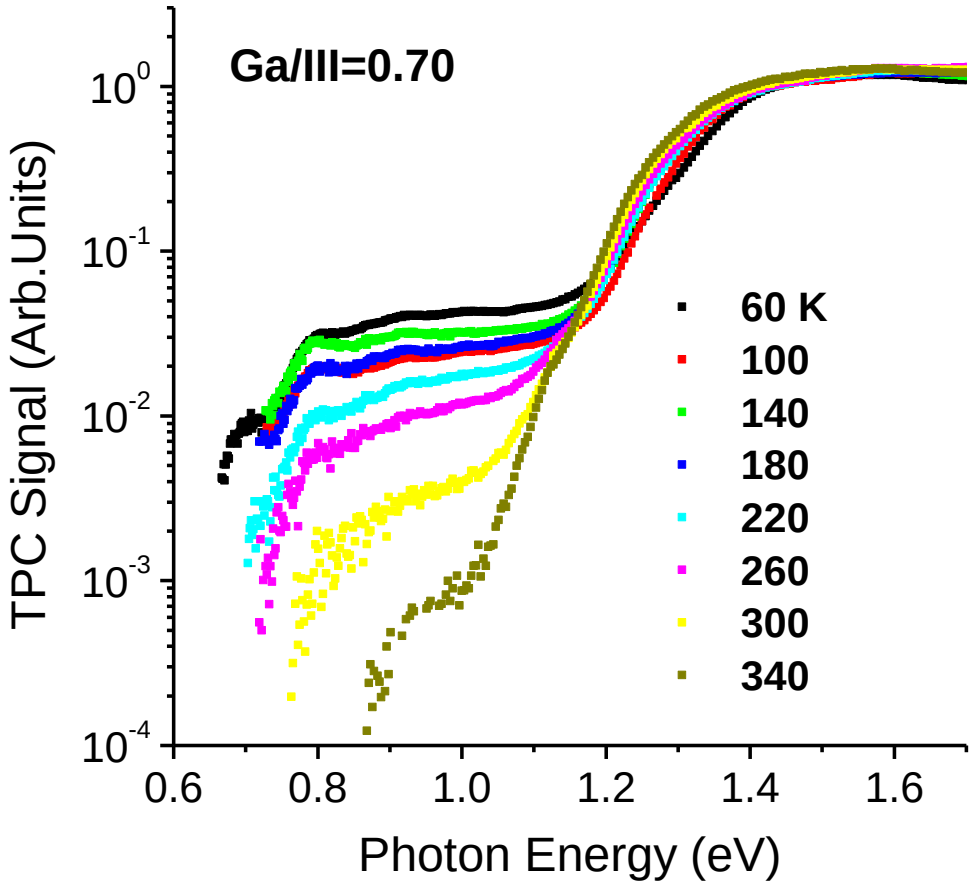

Fig. 6-1. Transient photocapacitance spectrum of CIGS thin-film solar cell with Ga/III ratio of 0.70 measured in the temperature range of 60 to 340 K

Fig. 6-2 shows the relation between the temperature and logarithm of TPC signal measured under monochromatic band gap light irradiation (at 0.8 eV) for CIGS solar cell with Ga/III ratio of 0.70. The variation of the TPC signal *S(T)*, with the temperature *T* was described by the thermal quenching model commonly used for the photoluminescence study [6-2, 3, 4, 5],

$$S(T) = \frac{S(0)}{1 + C\exp(-E_a / kT)} \tag{6-1}$$

where C is a constant and E_a is the activation energy of thermal quenching. The activation energy was obtained as 0.20 eV.

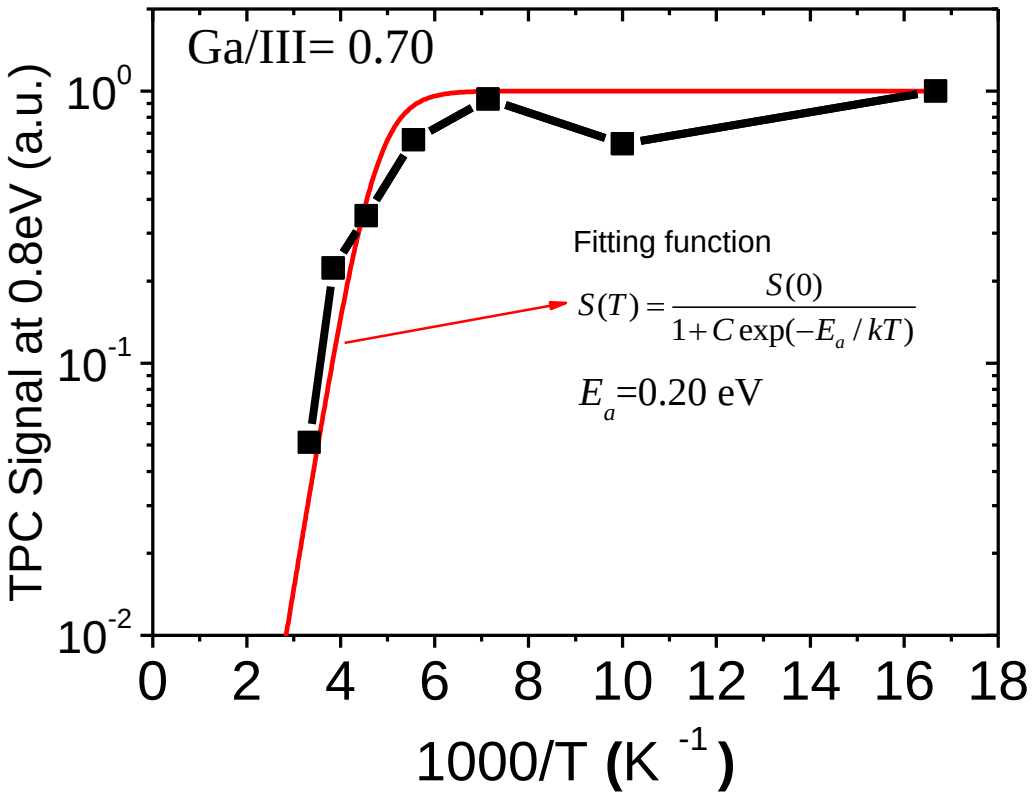

Fig. 6-2. Relation between temperature and TPC signal at photon energy 0.8 eV for CIGS solar cell with Ga/III ratio 0.70

Then, the relation between the temperature and the TPC signal at 0.8 eV photon energy after measuring CIGS solar cells with different Ga/III ratio (x) was shown in Fig. 6-3 [6-1]. Regardless of the Ga concentration, the values of E_a are calculated as 0.2–0.3 eV, as listed in the inset table in Fig. 6-3. These values are relatively small as compared to those expected from a previously reported model; this model is described in the next section.

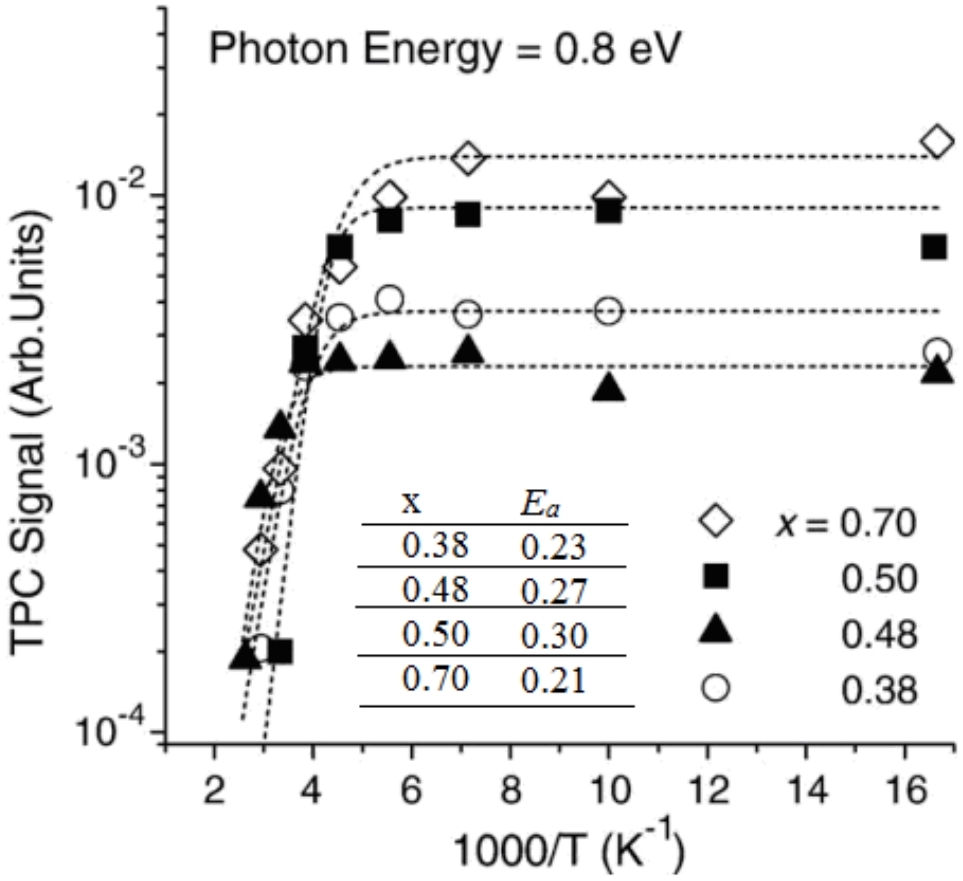

Fig. 6-3. Relation between temperature and logarithm of temperature and TPC signal at photon energy 0.8 eV for CIGS for CIGS solar cells with Ga/III ratio (x) from 0.38 to 0.70. Inset table shows the activation energy of thermal quenching E_a (eV) for each sample.

The mechanism of thermal quenching has been interpreted by using a discrete energy model [6-6]. In this model, the thermal excitation of the electrons trapped in deep defects to the conduction band leads to the quenching of the TPC signal, as shown in Fig. 6-4. By using this model, the thermal quenching activation energy E_a is the difference between the bandgap energy and the optical transition energy E_{opt}, e.g. $E_a=E_g-E_{opt}$. Thus, the activation energies of quenching are expected to be approximately 0.43 and 0.65 eV for the samples with Ga contents of 0.38 (E_g=1.23 eV) and 0.70 (E_g=1.45 eV), respectively. However, these values are considerably larger than those observed in the experiment as Fig. 6-3 shows. Moreover, a clear correlation of the activation energy to the Ga content in CIGS has not been found.

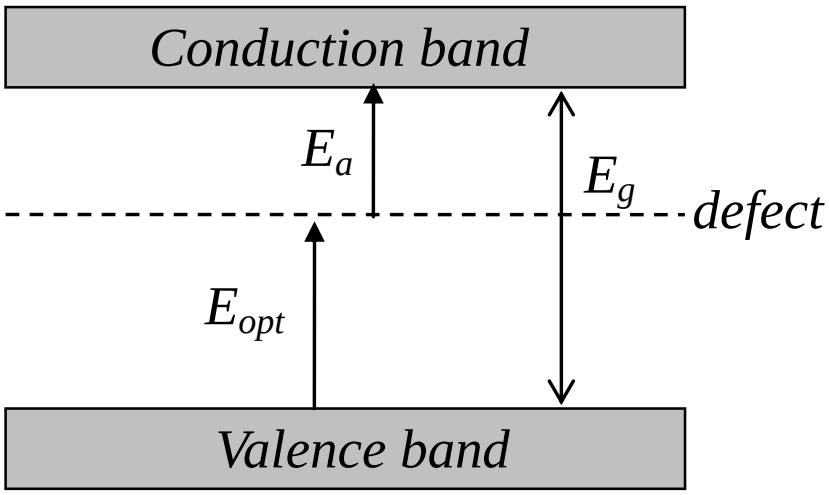

Fig. 6-4 Schematic energy diagrams of photoactive deep defects described by discrete energy model

6.2 Coordinate configuration model

Considering this, a configuration coordinate (CC) model [6-2, 7, 8] is proposed to explain the mechanism of the thermal quenching which is shown schematically in Fig. 6-5. Configuration diagram presents the energy state of an atom as a function of its position, this atom being either an impurity atom or a host lattice atom. At its equilibrium position, the ground state is at minimum potential. In this model, the potential energy curves (E_i) of the ground state (i=0) and excited states (i=1, 2) are represented by the following parabolic equation based on the harmonic motion of atoms,

$$E_i(Q) = E_i(Q_i) + \frac{1}{2}\omega^2(Q - Q_i) \tag{6-2}$$

where Q is the configuration coordinate, Q_i is the equilibrium position of the defect, and ω is the angular frequency. With increasing Ga content in CIGS, the band-gap energy increases; therefore, the excited state E_2 will be increased accordingly as the dot line shows in Fig. 6-5.

In this model, the behavior of the thermal and optical activation energies of the sub-bandgap TPC signal is interpreted by the distortions in the local defect configuration, which is described by the parabolic potential, $E_1(Q)$, with a different equilibrium position, Q_1. Since the optical and thermal activation energies do not depend on the specimen, $E_1(Q)$ can be fixed at almost the same energy regardless of the Ga content.

The optical process and thermal quenching process can be explained as follows. According to the

Frank–Condon principle [6-9, 10], the optical transition of electrons from the valence band to deep defect occurs without a variation in the configuration coordinate, as described by the vertical arrow at Q_0 (from A to B). Then, the charged defects relax their configuration from Q_0 to Q_1 (from B to C) with multi-phonon emissions. We suppose that the photo-active deep defect (E_1) may have a role of the minority carrier trap, of which recombination lifetime is fairly long. At low temperatures, the charged defects retain their configuration at Q_1 (position C) due to lower vibration energy. At high temperatures, atomic vibrations can shift their configuration from Q_1 to Q_1^* (from C to D), and the non-radiative transition occurs from D to A. Such a CC model can explain the variation in the optical and thermal activation energies of defects, as described by E_{opt} and E_a in Fig. 6-5. Since the trapping state is thermally quenched easily at room temperature, the photoactive deep defects may play an important role in the device performance.

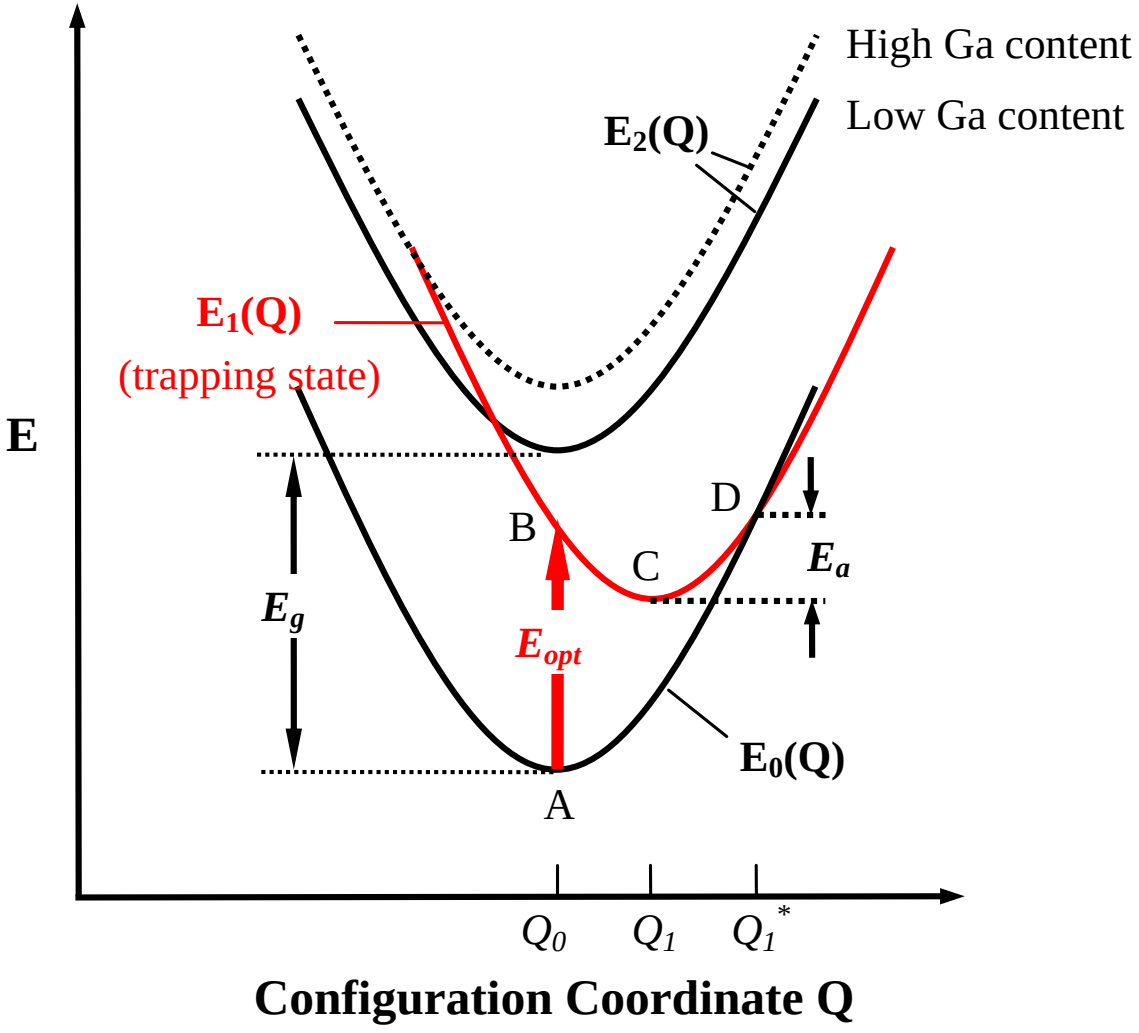

Fig. 6-5. Configuration coordinate model, explaining the optical transition and thermal activation energy observed by TPC signal in our study. A→B: optical transition without changing configuration coordinate; B→C: lattice relaxation with multi-phonon emissions; C→D: atomic vibrations by changing configuration coordinate; D→A: non-radiative transition by shifting configuration coordinate

6.3 Study of metastable state by steady-state photocapacitance

In chapter 5, steady-state photocapacitance with excitation light of low intensity (photon flux about 10^{15} $cm^{-2}s^{-1}$) has been used for investigating the quantitative information of the deep-level defect. In this part, steady-state photocapacitance with excitation light of high intensity (photon flux about 10^{18} $cm^{-2}s^{-1}$) was used for studying the metastable state of the deep-level defect. The other experimental details have been demonstrated in chapter 5.

Fig. 6-6 shows typical photocapacitance transients obtained for CIGS solar cells with varying Ga content under 0.8 eV light illumination at 60 K (for convenience, the term "0.8 eV light" is used in this study to represent the light at wavelength of 1550 nm from the monochromator). For p-type CIGS, the increase in capacitance after the onset of light (indicated by "ON" in Fig. 6-6) indicates a dominant emission of holes from the 0.8 eV level into the valence band. In general, for a single deep level contributing to the photocapacitance transient, the change in capacitance can be written as (Eq. (5-5) in chapter 5)

$$\Delta C(t) = \Delta C_{ss} \cdot (1 - e^{-t/\tau}) \tag{5-5}$$

where ΔC_{ss} is the steady-state photocapacitance, $\tau=1/(e_n^o+e_p^o)$ is the time constant for the transition process, and e_n^o and e_p^o are the optical emission rates of electrons and holes, respectively. Thus, by fitting Eq. (5-5) to the photocapacitance transient, the time constant of the photocapacitance transients could be obtained. It was found that after the 0.8 eV light was shut off (indicated by "OFF" for each sample in Fig. 5-5), the capacitances of all the samples didn't recover to their initial state at t=0. Rather, minutes after the light was turned off, they typically stabilized at much higher levels. For some samples (Ga 0.30 and Ga 0.52 in Fig. 5-5), the capacitance even shows an increase after turning off the light, a possible explanation is that the amount of majorities (holes) flowing out of the depletion region which were induced by the excitation light may contribute to the total free carriers' amount in the neutral region and caused a small shrink of the depletion region which caused the capacitance increase [6-11].

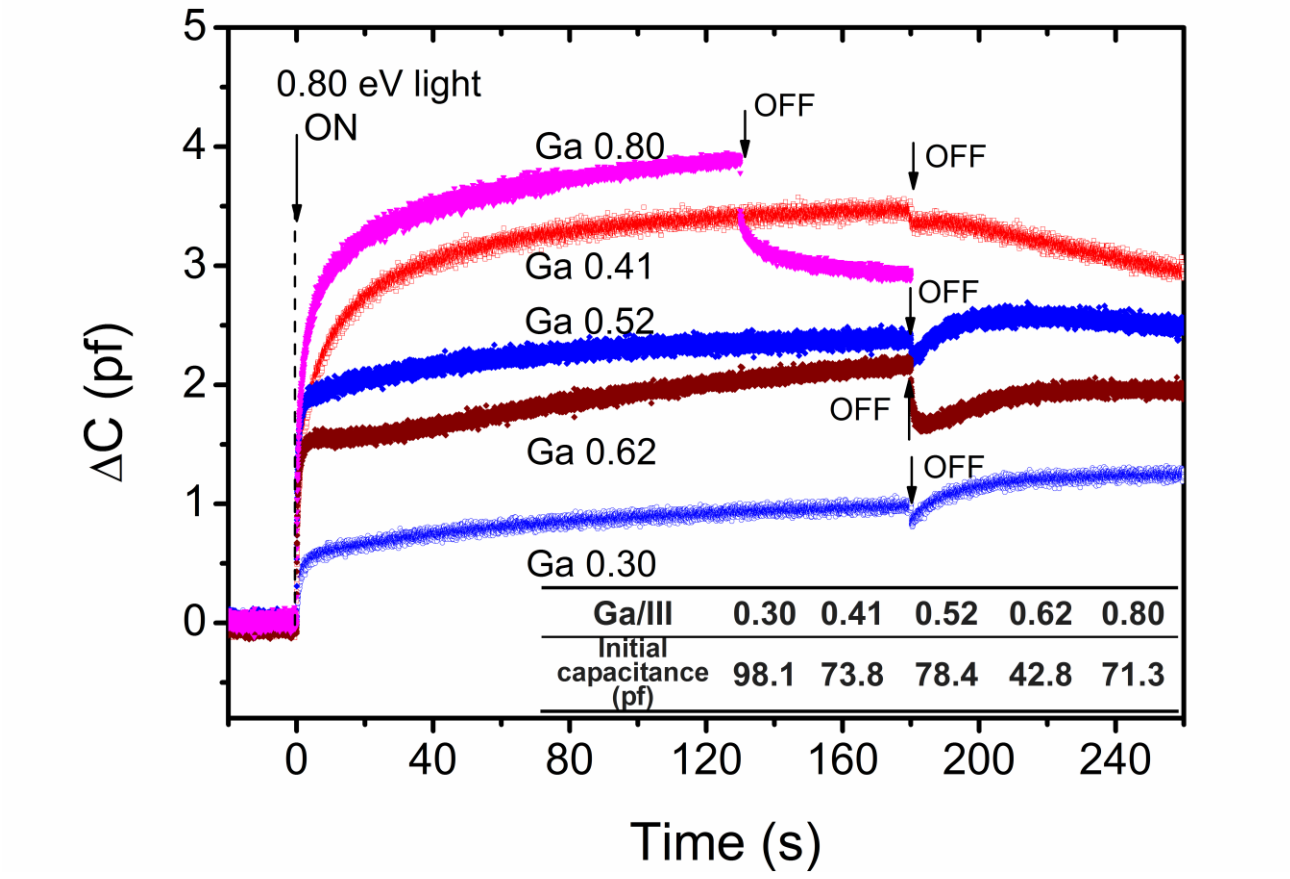

Fig. 6-6. Photocapacitance transients obtained for CIGS films of varying Ga content under illumination by 0.8 eV light at 60 K. The inset table shows the initial capacitance of each sample before illumination at 60 K.

An interesting phenomenon was observed for all samples when illuminated by the 0.8 eV light, namely the evolution of the capacitance into a steady-state photocapacitance versus time curve consisted of two distinct stages: a fast increase (τ_1) and a subsequent slow increase (τ_2), leading up to steady-state photocapacitance. This was verified by the fact that fitting the expression to the photocapacitance transient curve with a single time constant proved unfeasible, but with two time constants, it fit the data very well. Fig. 6-7 shows the typical fitting results for CIGS samples with Ga contents of 0.30, 0.62 and 0.80, for which the fast process was about 1~2 orders of magnitude faster than the slow one. It is noteworthy here that the heating effect of the illumination may contribute to the change of the capacitance, however we have measured the photocapacitance with different light intensity and by decreasing the light intensity to about 1-2 orders, assuming the capacitance change was proportional to the heating effect and the heating effect was proportional to the light intensity, the change of the capacitance should also decrease 1-2 orders, however, the photocapacitance change was just a little smaller than that in the high light intensity condition, so we consider the heating effect on the capacitance change negligible.

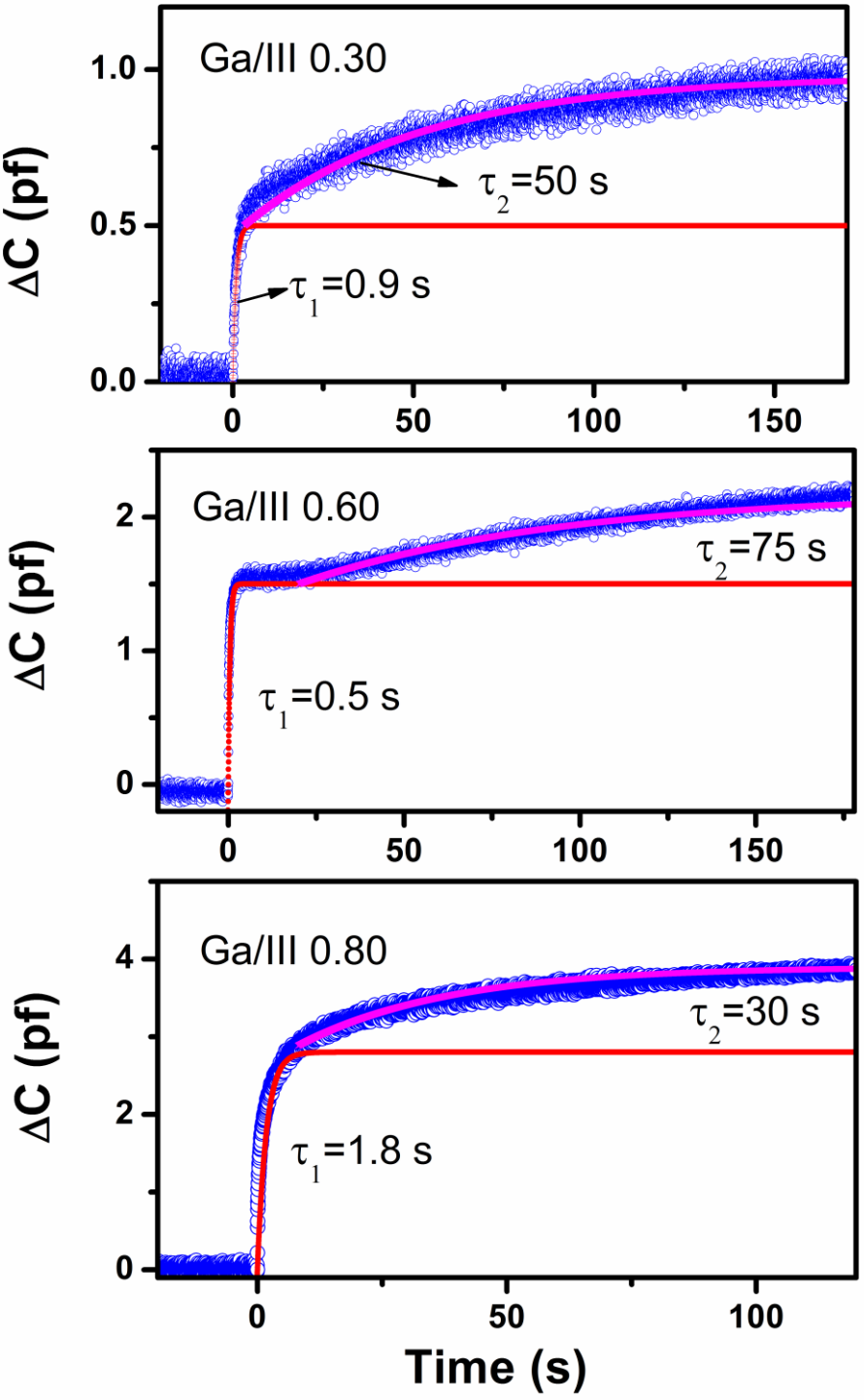

Fig. 6-7. Typical fitting results of photocapacitance transients for CIGS samples with a Ga content of 0.30, 0.62 and 0.80, obtained using Eq. (5-5) with two time constants.

A possible explanation to illustrate the fitting results was employed in this study considering that there are two separate optical transition processes of carriers involving the 0.8 eV deep-level defect. Here, the possibility of two different defect levels causing the two separate processes was excluded since the difference of the time constants (also the photo-ionization cross sections) of the two processes was about 1-2 orders large, and usually this was about the same orders of difference between the deep defect level and band-edges [6-1], and we don't think 0.8 eV light would excite shallow defect levels near the band-edges. Actually, a very similar phenomenon was also observed and is called the photocapacitance quenching effect in the case of the EL2 defect in n-type GaAs, which has been explained by the appearance of a metastable state of EL2 with a large lattice relaxation [6-12, 13]. Similarly, our experimental observations can possibly be explained by the configuration coordinate diagram model shown in Fig. 6-8. Two states are assumed for the 0.8 eV defect: a stable state, D, and its metastable state, D*. It is also assumed that there is a large lattice relaxation between states D and D*. With 0.8 eV light, photons can induce both VB→D and D→CB transitions (VB: valence band, CB: conduction band). With the optical emission rates of electrons, e_n^o, and holes, e_p^o, for the D state, a dynamic equilibrium would be reached if D* did not exist. The time constant for this part of the curves is $\tau=1/(e_n^o+e_p^o)$. However, at a photon energy of 0.8 eV, where the D→D* transition is also possible, even if the overall rate e_n^* for the transition D→D* is very small, a stable state will be reached after a certain time. Thus, the fast process consists of the transitions between the D state and the two bands, and the time constant is $\tau=1/(e_n^o+e_p^o)$, while the slow process is the transition between the D state and its metastable state D*, and the time constant is $\tau=1/e_n^*$, assuming the optical transition from D* to D is negligible. The directions of all arrows in Fig. 6-8 indicate only the transition direction of electrons, so the emission of holes from the defect e_p^o to the valence band is equivalent to the capture of electrons from the valence band by the defect.

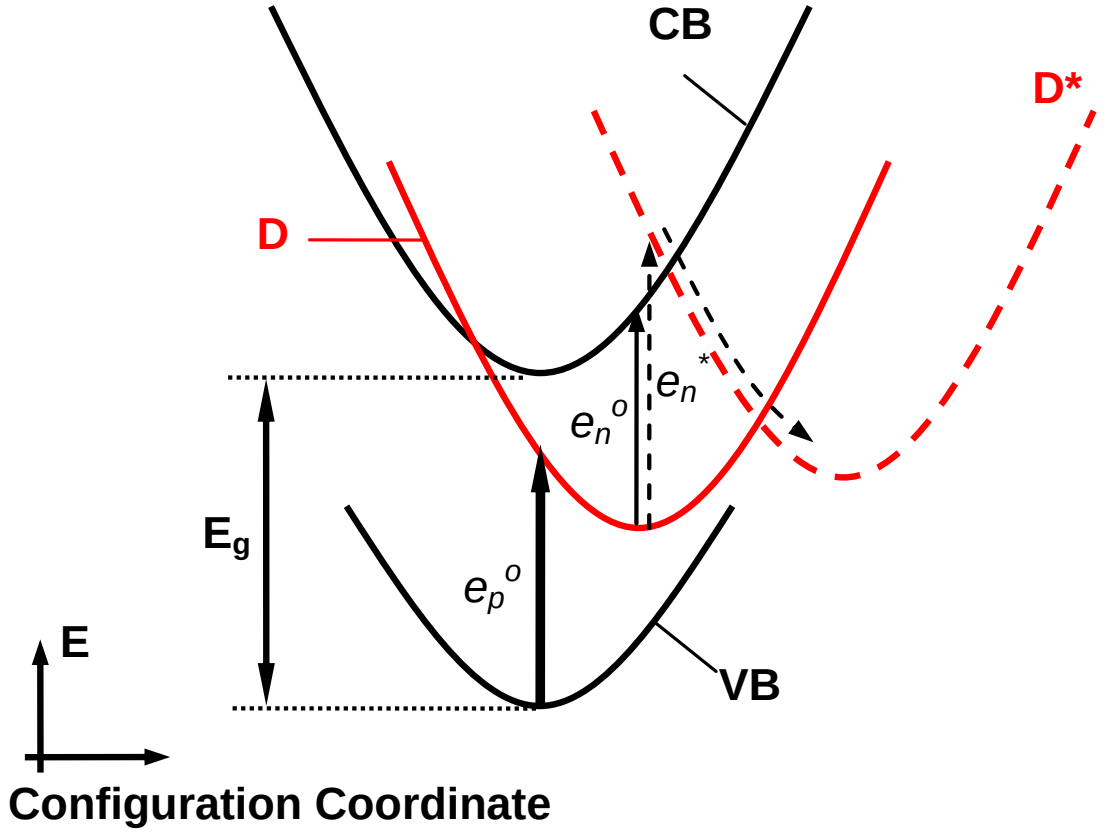

Fig. 6-8. Configuration coordinate diagram for optical transition processes involving deep-level defects

To investigate the optical transitions between the defect state and its metastable state, the photocapacitance transients, which depend on the photon energy striking the CIGS samples of varying Ga content, were also measured as Fig. 6-9 shows. It is worth noting that the measurements of the photon-energy-dependent photocapacitance transients were made after the initial measurements (as Fig. 6-6 shows), that is, at the end of the time in Fig. 6-6, where the capacitance almost reached a steady state after the 0.8 eV light was turned off. The much higher capacitances compared to the initial capacitances ($t<0$ in Fig. 6-6), even after the 0.8 eV light was turned off, indicated that both the stable and metastable states were still at least partly occupied by electrons. It was assumed that before the initial measurement, both the stable and metastable states were almost empty since the samples had been subjected to a long period of relaxation under dark conditions at room temperature in order to release the electrons in the defect level prior to the measurements. Thus, the photocapacitance transients in Figs. 6-6 and 6-9, obtained under the same 0.8 eV light, would be different. In Fig. 6-6, the initial condition was that both the stable and metastable states were empty, while in Fig. 6-9, the initial condition was that both the stable and metastable states were at least partly occupied by electrons. We found that for samples with a Ga content of 0.30, 0.40, and 0.62, there were three stages to the photocapacitance evolution process, *viz*., an initial fast increase, a subsequent slow decrease, and a final slow increase, while the sample having a Ga content of 0.80 exhibited only two increases.

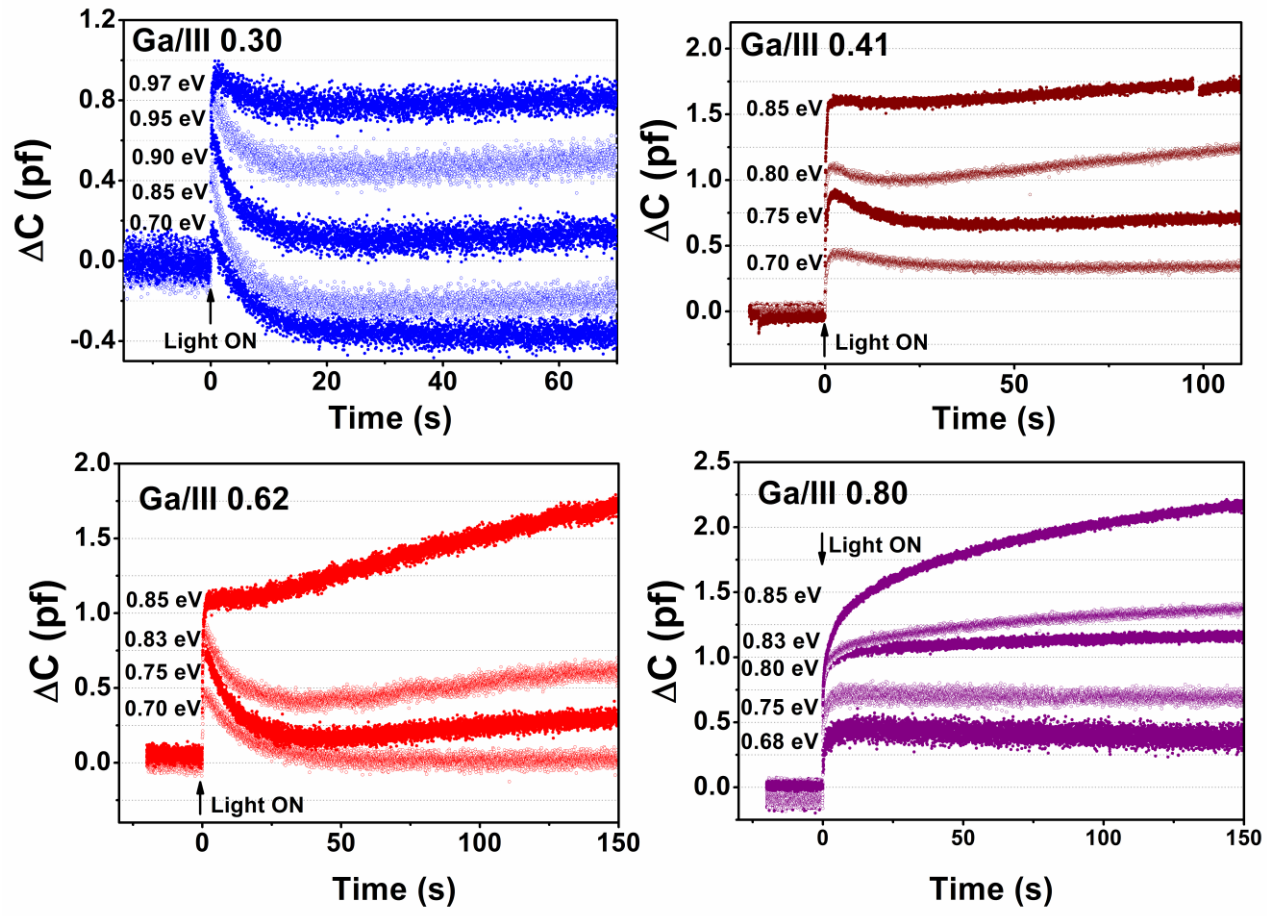

Fig. 6-9. Photon-energy-dependent photocapacitance transients for CIGS samples of various Ga content.

In order to clarify the different transition processes, we selected the capacitance transients of three samples under illumination by 0.8 eV light (see Fig. 6-10(a)). The proposed configuration coordinate model is shown in Fig. 6-10 (b). The two stages of increase are thought to involve the same process, illustrated in Fig. 6-7, which includes a stage of fast increase (defined as the $e_n^o + e_p^o$ process) and a stage of slow increase (defined as the e_n^* process). The new additional phase of decrease, which was not observed in Fig. 6-7, is considered to correspond to the optical emission of electrons (emission rate: e_n^{**}) from the metastable state (D*) to the stable state (D) and then to the conduction band (i.e., D*→D→CB, where the D*→D process was indicated by a blue line in Fig. 6-10(b)), and is defined as the $e_n^{**}+e_n^o$ process. The photocapacitance transients were the results of the total effect of the three processes. In Fig. 6-9, it can be seen that for the CIGS samples of Ga/III 0.30, 0.40 and 0.60, the stage of decrease (the $e_n^{**}+e_n^o$ process) gradually became indistinct as the incident photon energy increased. This could be explained by the lower threshold energy of the slow-decrease phase as compared to the slow-increase phase (the e_n^* process). (The threshold energy of the $e_n^{**}+e_n^o$ process is determined by the higher of the two processes e_n^{**} and e_n^o.) At low photon energies, the $e_n^{**}+e_n^o$ process dominates, while at high photon energies, the e_n^* process dominates. For the CIGS sample of Ga/III 0.80, no slow decrease process was observed at any photon energy. This could be because the optical threshold energy for the transitions from the metastable state to the stable state (D*→D, or e_n^{**} process) was so high that the photon energies used were not enough to excite the transition process. It was found that the optical threshold of the e_n^* process, which could be roughly determined from the energy at which the slow capacitance increase process starts to appear, changed little around 0.80 eV for all samples. (For the Ga 0.30 sample, however, no obvious slow capacitance increase (e_n^* process) was found across the entire range of photon energies examined). This was reasonable since for the same defect, the level of the metastable state was supposed not to change with the band gap energy.

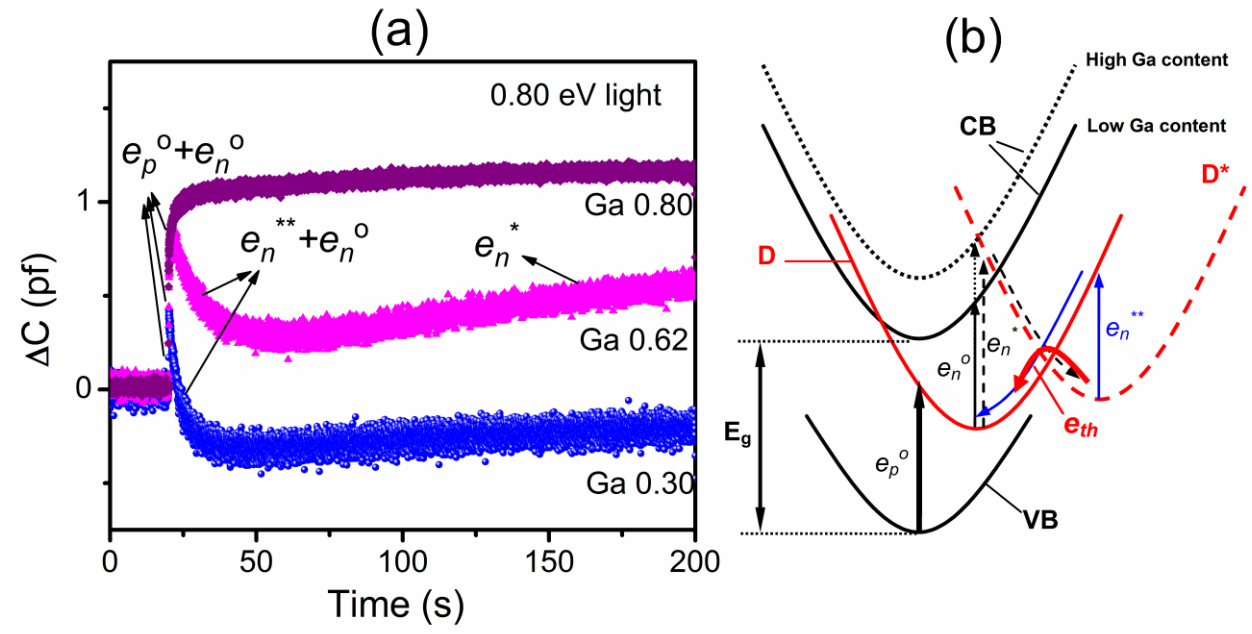

Fig. 6-10. (a) Photocapacitance transients of CIGS samples with a Ga content of 0.30, 0.60 and 0.80 under illumination by 0.8 eV light measured at 60 K; (b) Configuration coordinate model proposed to illustrate the optical transition processes.

It is worth noting that as the temperature increased, the optical transitions associated with the metastable state gradually disappeared. Fig. 6-11 shows the capacitance transients of four samples with different Ga content, measured at a threshold temperature where neither the slow-decrease ($e_n^{**}+e_n^{o}$ process) nor the slow-increase process (e_n^{*} process) was observed. In other words, only optical transition processes between the stable state and the two bands ($e_n^{o}+e_p^{o}$ process) could be observed, as shown in Fig. 6-11. This could be explained by the increasingly dominant thermal emission of electrons from the metastable state to the stable state (D*→D at the thermal excitation rate e_{th}, shown in Fig. 6-10(b)) with the rise in temperature, as compared to the optical processes associated with the metastable state.

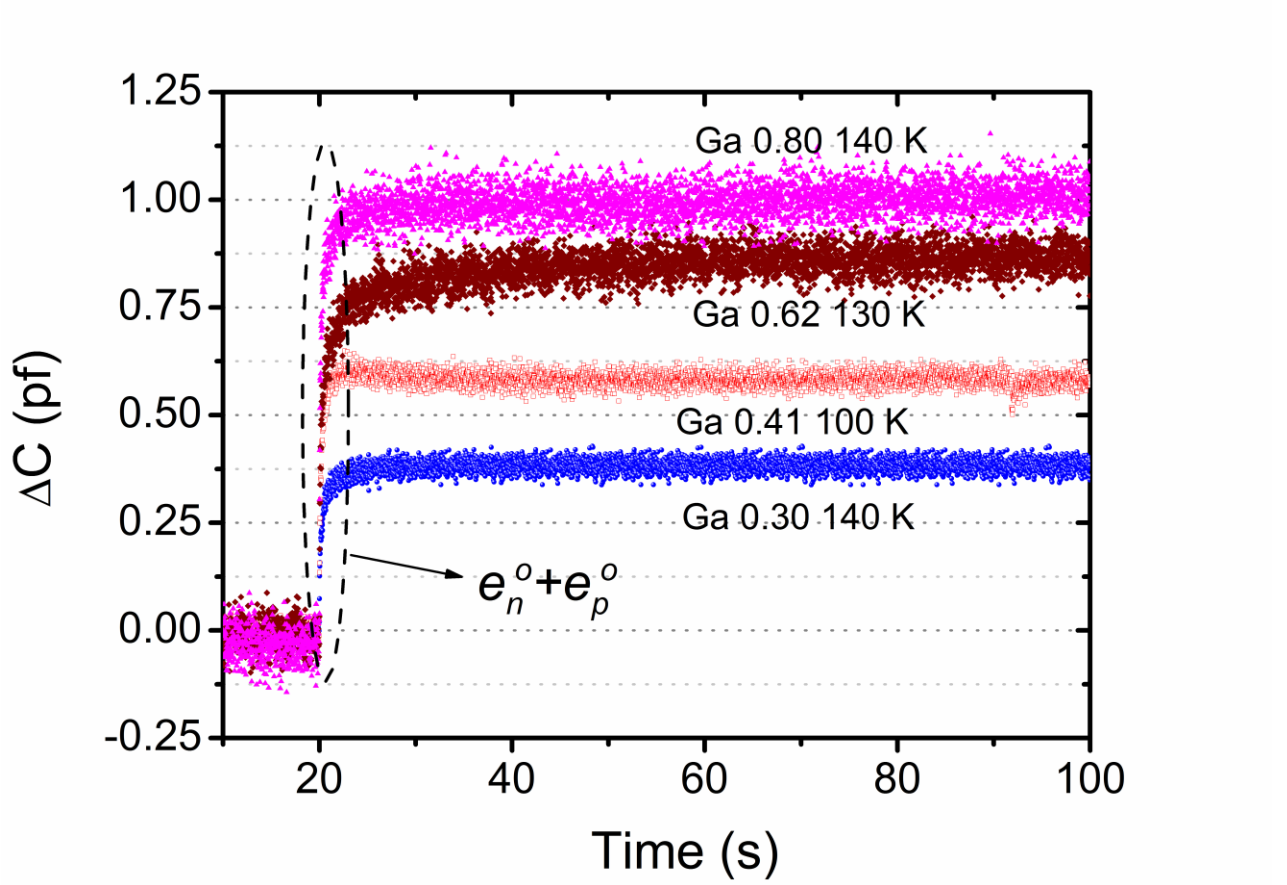

Fig. 6-11. Photocapacitance transients of four samples of varying Ga content, measured at the threshold temperature where neither the slow-decrease ($e_n^{**}+e_n^{o}$ process) nor slow-increase process (e_n^{*} process) was observed.

6.4 Summary

In conclusion, a configuration coordinate model considering distortions in the local defect configuration was proposed to explain the thermal and optical activation processes of the 0.8 eV deep-level defect. Also, the configuration coordinate model was improved to explain a phenomenon involving two states of the 0.8 eV defect, including a stable state, D, and a metastable state, D*, with a large lattice relaxation. The metastable state may provide another recombination path that may influence the performance of solar cells, however, how does it influence the performance needs more investigations.

Reference

[6-1] T. Sakurai, H. Uehigashi, M. M. Islam, T. Miyazaki, S. Ishizuka, K.Sakurai, A. Yamada, K. Matsubara, S. Niki, and K. Akimoto, Temperature dependence of photocapacitance spectrum of CIGS thin-film solar cell, Thin Solid Films **517** (2009) 2403-2406.

[6-2] J. I. Pankove, *Optical Processes in Semiconductors*, Dover, New York, 1971, chapter 7.

[6-3] A. Krtschil, H. Witte, M. Lisker, J. Christen, A. Krost, U. Birkle, S. Einfeldt, D. Hommel, F. Scholz, J. Off, M. Stutzmann, Photoelectric properties of the 0.44 eV deep level-to-band transition in gallium nitride investigated by optical admittance spectroscopy, Appl. Phys. Lett. **77** (2000) 546.

[6-4] S. Siebentritt and U. Rau, *Wide-Gap Chalcopyrites*, Springer Verlag, Berlin Heidelberg, 2006, p.113-156.

[6-5] H. Shibata, Negative thermal quenching curves in photoluminescence of solids, Jpn. J. Appl. Phys. **37** (1997) 550–553.

[6-6] M. Igalson, A. Urbaniak, Defect states in the CIGS solar cells by photocapacitance and deep level optical spectroscopy, Bull. Pol. Acad: Tech. **53** (2005) 157.

[6-7] P. M. Mooney, G. A. Northrop, T. N. Morgan, H. G. Grimmeiss, Evidence for large lattice relaxation at the DX center in Si-doped $Al_xGa_{1-x}As$, Phys. Rev. B **37** (1988) 8298.

[6-8] P. T. Landsberg, *Recombination in Semiconductors*, Cambridge University Press, Cambridge, 1991, chapter 5-6.

[6-9] J. Franck, Elementary processes of photochemical reactions, Transactions of the Faraday Society **21** (1926) 536–542.

[6-10] E. U. Condon, Nuclear motions associated with electron transitions in diatomic molecules, Phys. Rev. **32** (1928) 858–872.

[6-11] S. M. Sze and Kwok K. Ng, *Physics of semiconductor devices* (John Wiley & Sons, Hoboken, 2006) p.80-90.

[6-12] G. Vincent and D. Bois, Solid state Commun., Photocapacitance quenching effect for “oxygen” in

GaAs, **27** (1978) 431-434.

[6-13] G. Vincent, D. Bois and A. Chantre, Photoelectric memory effect in GaAs, J. Appl. Phys. **53** (1982) 3643.

Chapter 7 Possible origins of the deep-level defects in CIGS thin films Chapter

In previous chapters, the properties of the 0.8 eV deep defects have been investigated extensively. Since this defect may play a significant role in influencing the performance of the devices, a removal of the defects in CIGS to enhance the performance of CIGS solar cells is indispensable, thus the knowledge of the origin of this defect is necessary. About the 0.8 eV deep-level defect in CIGS film, models such as the V_{Se}–V_{Cu} divacancy defect model and $(In,Ga)_{Cu}$ antisite defect model were proposed for the possible origins for this defect [7-1], however, no definite conclusions has been made about the ogrins for this defect up to now. In our previous work [7-2], cation type vacancy defects were determined not the origin of deterioration of material properties in wide-gap CIGS by utilizing positron annihilation spectroscopy. Thus, antisite defects and/or anion type vacancy may be responsible for poor device performances in wide gap CIGS. In this chapter, possible candidates for this defect will be discussed.

7.1 $Cu_{2-x}Se$ secondary phase

Seceondary phase such as $Cu_{2-x}Se$ is an important factor that influences the performance of the CIGS solar cells. Usually, after the three-stage process for fabricating the CIGS thin films, KCN solution etching process is needed to remove the $Cu_{2-x}Se$ phase. Fig. 7-1 (a) shows the Raman spectroscopy of CIGS thin films by varying the Ga content from 0 to 1 before KCN etching (w/o KCN) and after KCN etching (KCN). The main peaks around 170-180 cm^{-1} originate from CIGS [7-3], while the peak around 260 cm^{-1} is from $Cu_{2-x}Se$ phase [7-4]. For all Ga content CIGS films, the intensity of $Cu_{2-x}Se$ peak was found decreased, which indicated the remove of the $Cu_{2-x}Se$ on the surface. For low Ga content CIGS films ($Ga<0.40$), it was found that no $Cu_{2-x}Se$ peak was observable at all, which means all the $Cu_{2-x}Se$ phase exists on the surface for these films, however, for high Ga content CIGS films ($Ga\geq0.40$), $Cu_{2-x}Se$ peak is still observable which indicates that the large amount of $Cu_{2-x}Se$ phase still exist in the sub-surface or even deeper regions for these films. In order to clearly see the effect of KCN etching for CIGS films with various Ga content, the Raman spectroscopy of CIGS thin films with various Ga content after surface KCN etching (KCN) is shown in Fig. 7-1 (b).

The effect of removing $Cu_{2-x}Se$ phase on the performance of CIGS solar cells is shown in Fig. 7-2. It can be seen that the efficiency generally increased after KCN etching of $Cu_{2-x}Se$ phase on the surface of CIGS films, and the effect becomes more and more obvious as Ga content increases. Thus, by removing the $Cu_{2-x}Se$ phase is a very effective way to enhance the performance of CIGS solar cells especially for high Ga content CIGS. But for high Ga content ($Ga\geq0.40$) CIGS, the problem is that although after KCN etching, $Cu_{2-x}Se$ phase still exist, so other method should be figured out to remove the residual $Cu_{2-x}Se$ phase which exist in the sub-surface or even deeper regions for these films, this may further enhance the performance of these cells. Here, we'll discuss the dependent of the residual $Cu_{2-x}Se$ phase on Ga content.

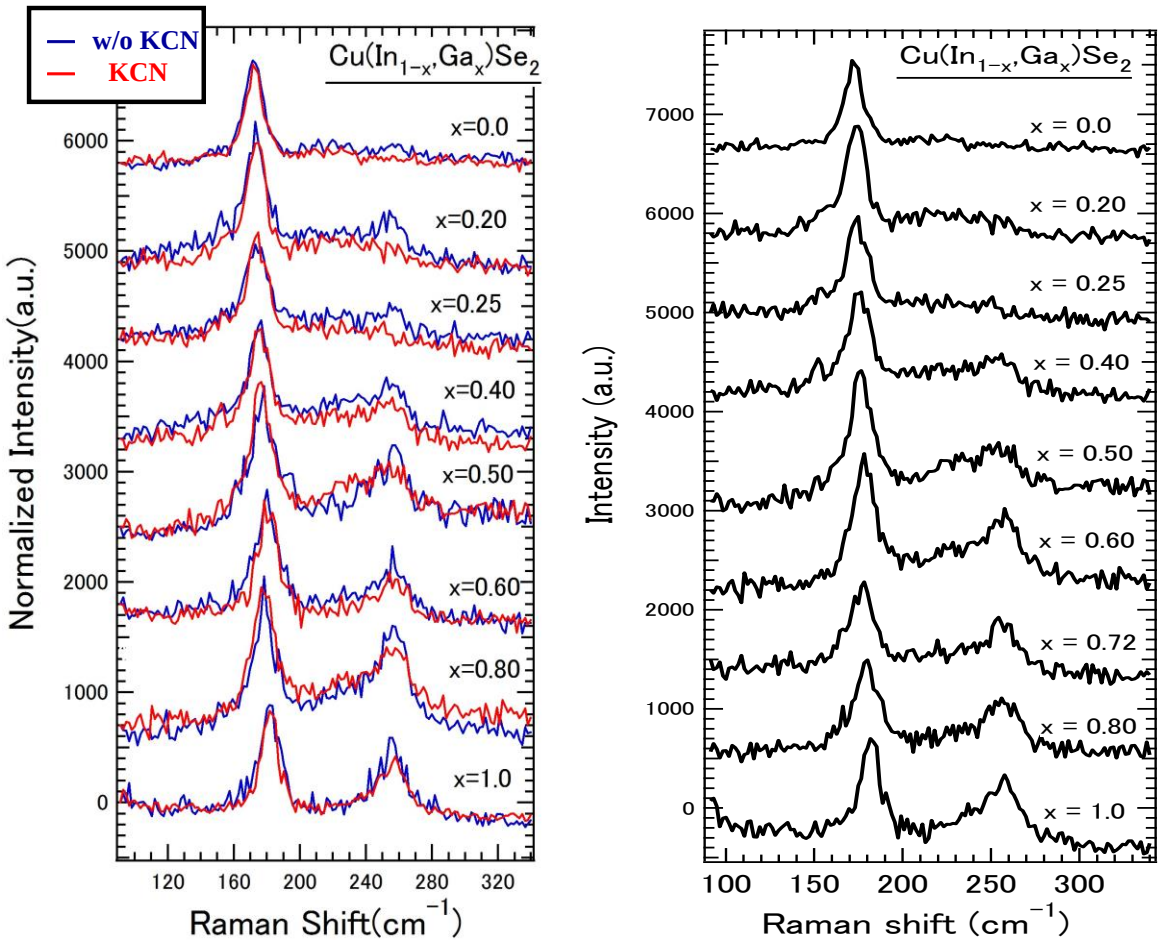

(a) (b)

Fig. 7-1. (a) Raman spectroscopy of CIGS thin films by varying the Ga content before KCN etching (w/o KCN) and after KCN etching (KCN). 170-180 cm^{-1} peaks originate from CIGS [7-3], while the peak around 260 cm^{-1} is from $Cu_{2-x}Se$ phase [7-4]. (b) Raman spectroscopy CIGS thin films after KCN etching (KCN). [7-5]

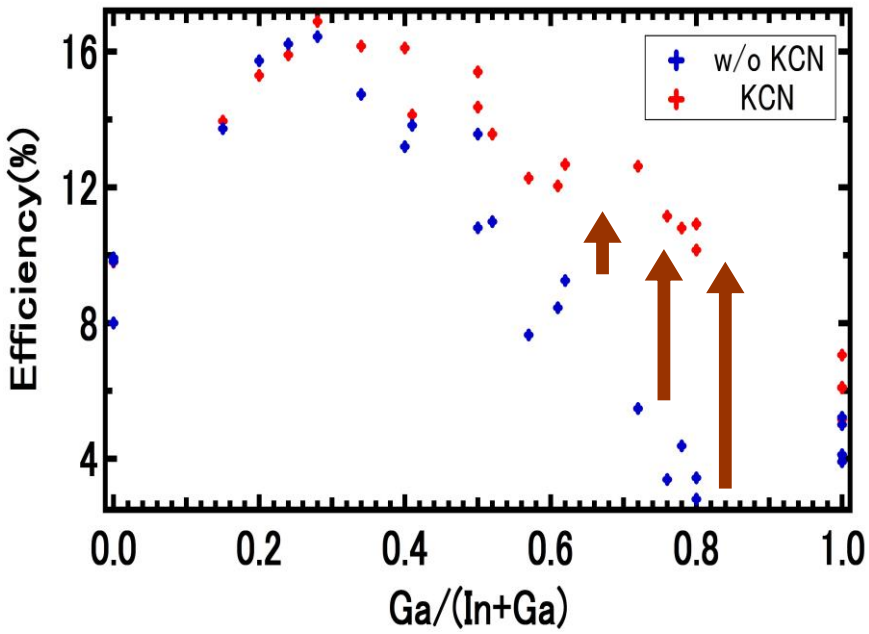

Fig. 7-2. The efficiency of CIGS solar cells with various Ga content before KCN etching (w/o KCN) and after KCN etching (KCN) [7-5].

Fig. 7-3 shows the Raman spectra of the typical three samples with Ga content of 0.30, 0.60 and 0.80. The spectra are convolved to four peaks by using Lorentz fitting (see sample Ga/III 0.80). As mentioned previously, the main peak around 170-180 cm^{-1} and the two peaks between 200 and 240 cm^{-1} originate from CIGS [7-3], while the peak around 260 cm^{-1} is from $Cu_{2-x}Se$ phase [7-4]. Then, the relative intensity of each peak could be obtained by comparing the area of each peak. Then the relative intensity of $Cu_{2-x}Se$ peak to the CIGS main peak dependent on Ga content are extracted as shown in the bottom right figure in Fig. 7-3. It was found that the intensity of $Cu_{2-x}Se$ peak increased with Ga content. Since the ef ficiency of the corresponding CIGS solar cells decreased with Ga content, the increased amount of residual $Cu_{2-x}Se$ phase was supposed to be correlated with the efficiency.

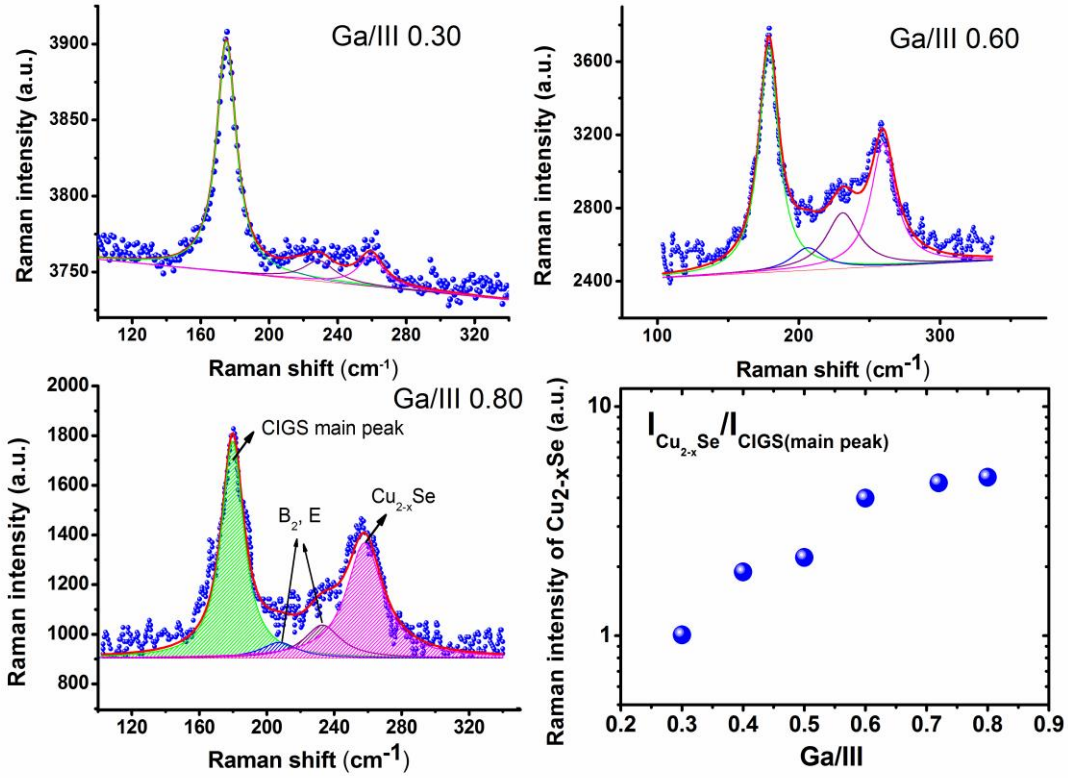

Fig. 7-3. Intensity of the secondary phase $Cu_{2-x}Se$ versus Ga/III ratio. Fitting results of the Raman signals were shown for Ga/III ratio of 0.30, 0.60 and 0.80.

As we have shown in our previous part, the increase of the concentration of the 0.8 eV defect versus the Ga content was considered also to be correlated with the cell efficiency as it acts as a recombination center. Then, to compare the two effects, the $Cu_{2-x}Se$ intensity versus Ga/III ratio from Raman measurement and the 0.8 eV defect density versus Ga/III ratio from TPC and SSPC measurements were normalized and compared in Fig. 7-4, a similar tendency with the Ga content could be seen, this may indicate the 0.8 eV defect is related with the $Cu_{2-x}Se$ secondary phase.

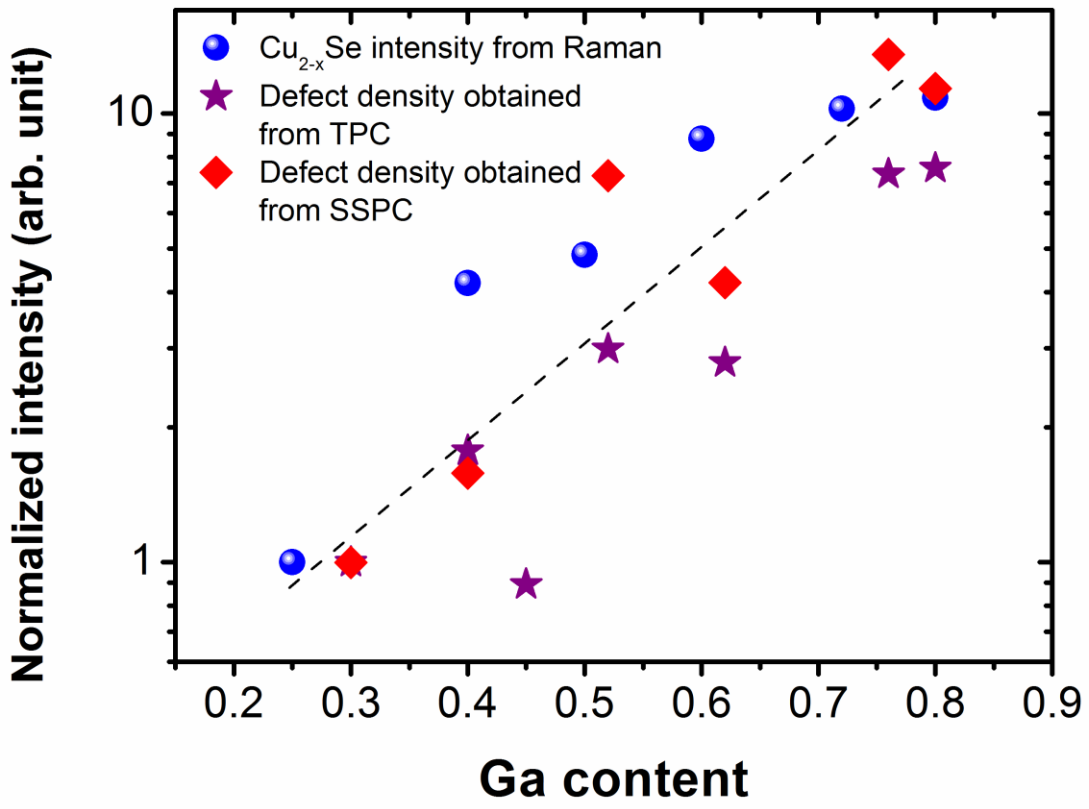

Fig.7-4. Comparison the $Cu_{2-x}Se$ intensity versus Ga/III ratio from Raman measurement and the 0.8 eV deep defect density versus Ga/III ratio from TPC and SSPC measurements.

7.2 Point defect model

Considering the 0.8 eV defect may originate from point defect but still relate with the $Cu_{2-x}Se$ phase, one possible candidate is Cu_{III} (III: In or Ga) antisite defect. Fig. 7-5 shows the crystal structure of chalcopyrite CIGS and the model for illustrating the effect of Cu_{III} antisite point defect on the formation of Cu-Se radicals and finally possibly forming $Cu_{2-x}Se$ secondary phase. Fig. 7-6 shows crystal structure of fluorite Cu_2Se, the Cu-Se bonding structure is very similar to structure of the Cu-Se radicals [7-6]. This indicates that the $Cu_{2-x}Se$ phase may originate from the aggregation of the Cu-Se radicals which are related with Cu_{III} antisite point defect.

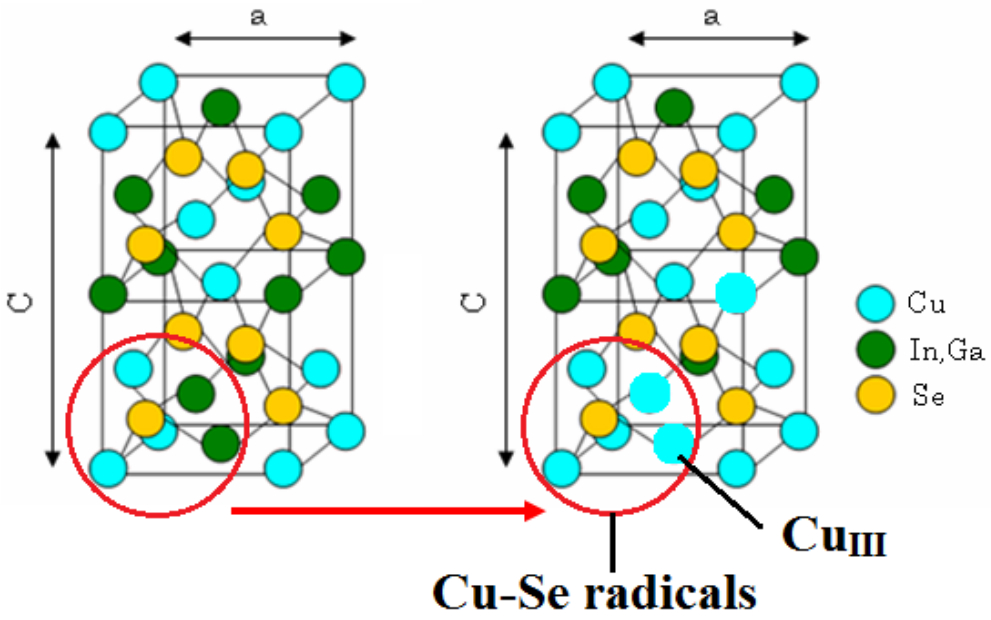

Fig. 7-5. The model for illustrating the effect of Cu_{III} antisite point defect on the formation of Cu-Se radicals and finally possibly forming $Cu_{2-x}Se$ secondary phase.

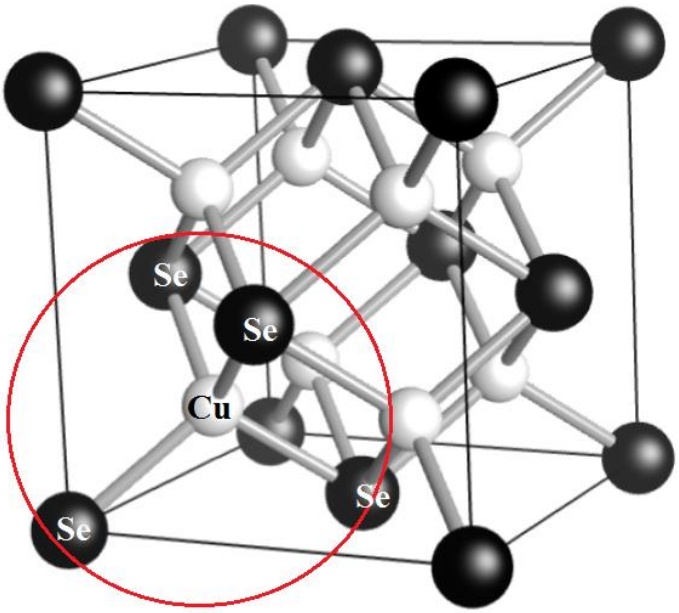

Fig. 7-6. The crystal structure of fluorite Cu_2Se, where Cu atoms are depicted by small (white) spheres and Se atoms by large (black) spheres. The Cu–Se bonds are shown in gray [7-6].

7.3 Conclusion

The formation of $Cu_{2-x}Se$ secondary phase in CIGS films seem to be related to the origin for the 0.8 eV defect and possible point defect such as Cu_{III} was proposed to illustrate as one candidate of the origin. However, the present study is still preliminary, more investigations are needed to determine the definite origin of this defect.

Reference

[7-1] S. Siebentritt, M. Igalson, C. Persson, and S. Lany, Prog. Photovoltaics **18** (2010) 390.

[7-2] M. M. Islam, *Growth and Defect Characterization of Cu($In_{1-x}Ga_x$)Se_2 Thin Film and Fabrication of Solar Cell*, PhD thesis, University of Tsukuba, 2010.

[7-3] C. Rincon, F. J. Ramirez, J. Appl. Phys. **72** (1992) 4321.

[7-4] T. Hsieh et al, Solid-State Electronics, **56** (2011) 175.

[7-5] Y. Takahashi, Formation of secondary phase in CIGS thin-film solar cells, Master thesis, University of Tsukuba, 2013.

[7-6] M. Rasander, L. Bergqvist, and A. Delin, Density functional theory study of the electronic structure of fluorite Cu2Se, J. Phys.: Condens. Matter **25** (2013) 125503.

Chapter 8 Conclusions

This work focused on the study of deep-level defects which located near the midgap energy level of the bandgap in Cu(In, Ga)Se_2 thin film solar cells since these defects may act as active recombination centers to limit the cell efficiency.

Transient photocapacitance (TPC) spectroscopy was used to qualitatively characterize the properties of deep-level defects. With this method, a defect level at 0.8 eV above the valence band maximum (VBM) was observed almost unchanged with Ga/(Ga+In) or Ga/III ratio. Then, a relatively quantitative comparison of deep defect densities based on the results of TPC showed that the defect density seems to increase with increasing Ga/III ratio.

Two-wavelength excitation photocapacitance spectroscopy was utilized to investigate the role of the 0.8 eV deep-level defect, that is, whether or not the defect level acts as a recombination center. With this method, the 0.8 eV defect was found to act as a trap center at low temperature (140 K) but act as a recombination center at at room temperature.

Steady-state photocapacitance (SSPC) method with low intensity excitation light was employed to quantitatively investigate the properties of the 0.8 eV deep-level defect. The defect concentration in the order of 10^{13}-10^{14} cm^{-3} and the photoionization cross section in the order of 10^{-17}-10^{-16} cm^2 were obtained and both the defect concentration and the cross section were found to increase with Ga content (x) in the range of 0.30-0.80.

Steady-state photocapacitance (SSPC) measurements with high intensity excitation light were performed in order to investigate the optical transition properties and structure of the 0.8 eV deep-level defect. Upon the results, a configuration coordinate model was proposed for the 0.8 eV defect assuming two states: a stable state D and its metastable state D* with a large lattice relaxation. The metastable state was found to disappear at high temperature (>140 K) due to the low thermal activation energy.

Time-resolved photoluminescence (TRPL) was used to investigate the effect of the deep-level defects on the devices. According to the results, deep-level defects other than shallow-level defects were supposed to act as the main recombination centers to cause the short minority carrier lifetime in Cu(In, Ga)Se_2 thin films. By comparing the results of TRPL and photocapacitance (including TPC and SSPC), it was deduced that the 0.80 eV deep-level defect may act as a significant recombination center that decreases the minority carrier lifetime in CIGS thin films when Ga content increases.

Possible origins of the 0.8 eV defect were considered to be related with $Cu_{2-x}Se$ while comparing the respective quantity relationship with Ga/III ratio.

Since the 0.80 eV deep-level defect is one of the causes for the degradation of CIGS cell efficiency with high Ga content, it is necessary to decrease the density of defects to improve cell efficiency, especially for CIGS samples with high Ga content.

Acknowledgements

First of all, I would like to give my deepest appreciation to my best respectful supervisor, Prof. Katsuhiro Akimoto. He is a so brilliant scientist that I have learned so much from him. He is so gentle and patient that every time when I met problems in research or life, he would do his best to help me and give useful advice to me. He always gives me valuable and constructive advices during discussion at any time. He also provides me many good opportunities to participate international conferences to communicate with other researchers. His wisdom and research expertise are invaluable fortune in my life.

I would like also to thank Associate Prof. Takeaki Sakurai, he gave me a lot of useful advices and help on my research experiments.

And I would like to thank the members from Akimoto Lab. who gave me help for the experiments, thanks for Natsuka san and Hagiya san for providing CIGS samples to support my experiments. Also, I would like to thank all the members in our lab, they accompany me to have a happy life in a harmonious Lab. This is meaningful treasure for me and it will be a good memory in my life. I also thank all of my good friends with whom I have a happy life in Japan.

Also I would like to thank to Prof. Dejun Han from Beijing Normal University who is my supervisor in my Master period, he gave me a lot of help when I applied the doctoral program in Japan. I also appreciate the Japanese government MEXT for providing scholarships to support my study in Japan.

Finally, I would like to thank all my family members especially my grandmother, my parents and my sister. Their love and support enable me to arrive where I am today.

Publication lists

1. **Xiaobo Hu,** Amit Gupta, Takeaki Sakurai, Akimasa Yamada, Shogo Ishizuka, Shigeru Niki, and Katsuhiro Akimoto. Investigation of deep-level defects in Cu(In,Ga)Se_2 thin films by two-wavelength excitation photo-capacitance spectroscopy. Applied Physics Letters **103**, 163905 (2013).
2. **Xiaobo Hu,** Takeaki Sakurai, Akimasa Yamada, Shogo Ishizuka, Shigeru Niki, and Katsuhiro Akimoto, Investigation of the relative density of deep defects in Cu(In,Ga)Se_2 thin films dependent on Ga content by transient photocapacitance method. Japanese Journal of Applied Physics **53**,068008 (2014).
3. **Xiaobo Hu,** Takeaki Sakurai, Akimasa Yamada, Shogo Ishizuka, Shigeru Niki, and Katsuhiro Akimoto, Investigation of deep-level defects in Cu(In,Ga)Se_2 thin films by a steady-state photocapacitance method. Journal of Applied Physics **116**, 163703 (2014).
4. **Xiaobo Hu,** Takeaki Sakurai, Akimasa Yamada, Shogo Ishizuka, Shigeru Niki, and Katsuhiro Akimoto, Investigation of the Properties of Deep-level Defect in Cu(In,Ga)Se_2 Thin Films by Steady-State Photo-Capacitance and Time-Resolved Photoluminescence Methods. Japanese Journal of Applied Physics, **54**, 04DR02 (2014).

Conference contributions

1. **Xiaobo Hu,** Takeaki Sakurai, Akimasa Yamada, Shogo Ishizuka, Shigeru Niki, and Katsuhiro Akimoto. Characterization of deep defects in Cu(In,Ga)Se_2 by transient photo-capacitance method. The 74th Autumn Meeting of Japan Society of Applied Physics, 2013, 18p-P12-8, September 18, 2013, Kyotanabe Campus, Doshisha University, Kyotanabe City, Kyoto, Japan.
2. **Xiaobo Hu,** Amit Gupta, Takeaki Sakurai, Akimasa Yamada, Shogo Ishizuka, Shigeru Niki, and Katsuhiro Akimoto. Investigation of deep-level defects in Cu(In,Ga)Se2 thin films by two-wavelength excitation photo-capacitance spectroscopy. The 2013 Japan Society of Applied Physics and The Materials Research Society Joint Symposia, 2013, 20a-M2-7, September 20, 2013, Kyotanabe Campus, Doshisha University, Kyotanabe City, Kyoto, Japan.
3. **Xiaobo Hu,** Takeaki Sakurai, Akimasa Yamada, Shogo Ishizuka, Shigeru Niki, and Katsuhiro Akimoto. Characterization of deep defects in Cu(In,Ga)Se_2 by transient photo-capacitance method. The 23rd International Photovoltaic Science and Engineering Conference. October 8-November 2, 2013, Taipei International Convention Center, Taipei, Taiwan.
4. **Xiaobo Hu,** Takeaki Sakurai, Akimasa Yamada, Shogo Ishizuka, Shigeru Niki, and Katsuhiro Akimoto. Investigation of deep-level defects in Cu(In,Ga)Se2 thin films by single-wavelength and two-wavelength transient photo-capacitance spectroscopy. Grand Renewable Energy 2014 International Conference and Exhibition. July 27-August 1, 2014, Tokyo Big Sight, Tokyo, Japan.
5. **Xiaobo Hu,** Takeaki Sakurai, Akimasa Yamada, Shogo Ishizuka, Shigeru Niki, and Katsuhiro Akimoto. Properties of depp-level defects in Cu(In,Ga)Se_2 thin films. 2014 International conference on solid state devices and materials, No.G-6-2. September 8-11, 2014, Tsukuba International Congress Center, Tsukuba, Japan.
6. **Xiaobo Hu,** Takeaki Sakurai, Akimasa Yamada, Shogo Ishizuka, Shigeru Niki, and Katsuhiro Akimoto. Properties of depp-level defects in Cu(In,Ga)Se_2 thin films investigated by Steady state photocapacitance method. 2014 WEPEC-6, 3TuPo.5.6, 2014, Kyoto International Conference Center, Kyoto, Japan.